BRNO UNIVERSITY OF TECHNOLOGY
VYSOKÉ UČENÍ TECHNICKÉ V BRNĚ

FACULTY OF MECHANICAL ENGINEERING
FAKULTA STROJNÍHO INŽENÝRSTVÍ

INSTITUTE OF PHYSICAL ENGINEERING
ÚSTAV FYZIKÁLNÍHO INŽENÝRSTVÍ

BEHAVIOUR OF OBJECTS IN STRUCTURED LIGHT FIELDS AND LOW PRESSURES

CHOVÁNÍ OBJEKTŮ VE STRUKTUROVANÝCH SVĚTELNÝCH POLÍCH A NÍZKÝCH TLACÍCH

DOCTORAL THESIS
DIZERTAČNÍ PRÁCE

AUTHOR
AUTOR PRÁCE

Ing. Jana Flajšmanová

SUPERVISOR
VEDOUCÍ PRÁCE

prof. RNDr. Pavel Zemánek, Ph.D.

BRNO 2020

ABSTRACT

A deeper understanding of behaviour of optically trapped particles reveals underlying physical phenomena arising from the light–matter interaction. We present an explanation of the enhancement of the pulling force acting on optically bound particles in the structured optical field, so–called tractor beam. It is demonstrated that the motion of two optically bound objects in a tractor beam strongly depends on their mutual distance and spatial orientation, which adds an extra flexibility to our ability to control matter with light.

Subsequently, the thesis is focused on the optical levitation of a particle in a vacuum. We propose a novel methodology for a characterization of properties of a weakly nonlinear Duffing oscillator represented by an optically levitated nanoparticle. The method is based on averaging recorded trajectories with defined initial positions in the phase space of nanoparticle position and momentum and provides us with the oscillator parameters directly from the recorded motion. Our innovative approach is compared with the commonly used power–spectral–density fitting, and exploiting numerical simulations, we show its applicability even at lower pressures where the nonlinearity starts to play a significant role.

KEYWORDS

optical trapping, optical tweezers, tractor beam, optical binding, holographic video microscopy, optical levitation, phase portrait, Duffing oscillator, nonlinearity

ABSTRAKT

Studium chování opticky zachycených částic nám umožňuje porozumět základním fyzikálním jevům plynoucím z interakce světla a hmoty. Předkládaná práce podává vysvětlení zesílení tažné síly působící na opticky svázané částice ve strukturovaném světelném poli, tzv. tažném svazku. Ukazujeme, že pohyb dvou opticky svázaných objektů v tažném svazku je silně závislý na jejich vzájemné vzdálenosti a prostorové orientaci, což rozšiřuje možnosti manipulace hmoty pomocí světla.

Následně se práce zaměřuje na levitaci opticky zachycených částic ve vakuu. Představujeme novou metodologii na charakterizaci vlastností slabě nelinearního Duffingova oscilátoru reprezentovaného opticky levitující částicí. Metoda je založena na průměrování trajektorií s určitou počáteční pozicí ve fázovém prostoru sestávajícím z polohy a rychlosti částice a poskytuje informaci o parametrech oscilátoru přímo ze zaznamenaného pohybu. Náš inovativní postup je srovnán s běžně užívanou metodou založenou na analýze spektrální hustoty polohy částice a za využití numerických simulací ukazujeme její použitelnost i v nízkých tlacích, kde nelinearita hraje významnou roli.

KLÍČOVÁ SLOVA

optické chytání, optická pinzeta, tažný svazek, optická vazba, holografická video mikroskopie, optická levitace, fázový portrét, Duffingův oscilátor, nelinearita

FLAJŠMANOVÁ, Jana *Chování objektů ve strukturovaných světelných polích a nízkých tlacích*. Brno: Vysoké učení technické v Brně, Fakulta strojního inženýrství, Ústav fyzikálního inženýrství, 2020. 117 s. Dizertační práce. Vedoucí práce prof. RNDr. Pavel Zemánek, Ph.D.

Prohlášení

Prohlašuji, že jsem dizertační práci vypracovala samostatně pod odborným vedením prof. RNDr. Pavla Zemánka, Ph.D., a že veškeré podklady, ze kterých jsem čerpala, jsou uvedeny v seznamu použité literatury.

Acknowledgements

My sincere gratitude goes to prof. Pavel Zemánek for introducing me to the exciting world of optical micromanipulations and his patient supervision throughout my whole Ph.D. He was always keen to discuss and solve various scientific problems and his endless support and many suggestions were deeply appreciated. I am grateful to him for introducing me to the community of optical micromanipulations at numerous conferences and seminars. I thank Oto Brzobohatý for sharing his experience in experimental procedures and willingness to assist in laboratory issues. I would also like to thank Martin Šiler and Lukáš Chvátal for their extensive support in numerical simulations and data processing and their enthusiasm to explain all the associated issues helpfully. I am grateful to everyone without whom this work would not be possible, especially Petr Jákl, František Hrubý, Radim Filip, Jan Ježek and Jindřich Oulehla. I also thank all the other colleagues for creating a pleasant atmosphere for work and fruitful discussions. My thanks goes to my parents, Lukáš and my closest family for their support and love.

For the financial support I would like to acknowledge Brno Ph.D. talent program financed by city of Brno and South Moravian Region.
The research was supported by projects of CSF (GA14-16195S and 19-17765S), TACR (TE01020233) and its infrastructure by MEYS CR, EC, and CAS (LO1212, CZ.1.05/2.1.00/01.0017, RVO:68081731).

Jana Flajšmanová

CONTENTS

INTRODUCTION

Since the invention of the laser in 1960 [1], there have been developed various research areas where unique properties of laser radiation are exploited. One example of the important laser–based methods is optical trapping that enables to manipulate deterministically with nano- to microscale particles or bioobjects without any physical contact. This technique has become a powerful tool not only in the field of biology for manipulation and characterization of micro–sized objects [2, 3], but the optical trapping is also utilized for single- or multiparticle studies in the field of ultracold atom physics [4], statistical physics [5] or even quantum physics [6].

The aim of the thesis is to investigate the dynamics of optically trapped particles in various structured optical fields and ambient environments where we explore a coupling between the light and mechanical motion of microscopic matter in overdamped and underdamped regimes. The presented work tackles two significant and very actual directions in the vast field of optical manipulation techniques. The first topic deals with the motion of optically bound particle pairs in complex structured light fields, also referred to as the tractor beam. The presented thorough experimental investigation allows us to observe number of intriguing phenomena. Together with the support of numerical simulations, we provide the first intuitive and rigorous description of this yet not fully understood system.

The second system studied in the thesis is a seemingly very fundamental experiment performed on a single optically trapped particle in a vacuum. This setup is often used in optical cooling experiments with an aim to bring a levitated object into its quantum ground state. We show that the theoretical description of the system is often oversimplified, which can lead to an incorrect determination of the crucial system parameters. We present a novel approach exploiting a more accurate approximation of the problem and we provide both the experimental investigation and the numerical simulations showing the applicability and limitations of the novel and commonly used methods.

The thesis is organized as follows. After the introduction to the basics of optical trapping of nano- and microobjects in Chapter 1, Chapter 2 deals with the overdamped system in the complex optical field created by a retro–reflection of a single Gaussian beam [7]. Such a configuration, called tractor beam, exhibits the counter–intuitive optical delivery of illuminated objects. The tractor beam can exert a pulling force that drags particles against the total wave vector of the incident field even if the light intensity profile along the beam propagation is uniform.

The particle motion in the tractor beam is usually driven by the particle scattering. If most incident photons are scattered more in the forward direction, the change

in the photon momenta leads to the object motion against the overall photon flow. It has recently been experimentally observed that the pulling force can be significantly enhanced if a nonspherical scatterer, e.g. a linear chain of particles, is optically transported [7]. Here we focus on the motion of two optically bound particles in the tractor beam. Due to the inter–particle scattering, the originally uniform electric field is modulated, which strongly influences the particle pair dynamics.

Chapter 2 based on the published results [8] is introduced by principles of the tractor beam and optical binding followed by the detailed description of the experimental setup together with the holographic video microscopy [9, 10]. This technique enables the precise 3D tracking of few particles trapped in the tractor beam by the post–processing of hologram records and the behaviour of particle pairs in the tractor beam can be studied. The experimental work is then presented and compared with theoretical predictions based on the multi–particle Mie theory [11]. The achieved results demonstrate a strong dependence of the optical force acting on the optically bound particle pair on its internal conformation and orientation in the tractor beam. We show that even the direction of the optical force can be varied simply by the pair arrangement and the force magnitude can be enhanced by an order comparing to a single particle placed in the tractor beam.

The second part of the presented work is devoted to single–particle dynamics in the underdamped regime. Recently, there has been a renewed interest in the dynamics of a single particle optically trapped in a single focused laser beam. However, in contrast to previous efforts, the stress has been put more on a weakly damped particle levitated in vacuum [12–16]. These activities have been motivated by the possibility of entering the quantum regime [17], which is not easily accessible because the clamping to the environment usually deteriorates the quantum properties of a system [12].

In Chapter 3 based on the results presented in [18] we focus on investigating the dynamics exhibited by particles optically levitated in vacuum. A nanoparticle in an optical trap acts as a nanomechanical oscillator with broadly tunable parameters. Such an oscillator can be utilized for measurements of very weak forces [19–22] or as an instrument for testing nanothermodynamic phenomena in the underdamped regime [23, 24] and studying quantum properties of microscopic objects [25, 26]. To exploit a levitated oscillator, a precise characterization of its parameters is highly desirable. A harmonic oscillator is usually assumed for the system characterization [12, 14, 27, 28] but it is not always applicable, especially at lower ambient pressures and higher energy states of a levitated particle. Therefore, we have developed a new methodology for characterizing the properties of a weakly nonlinear oscillator.

Chapter 3 begins with a description of our experimental setup used for an optical levitation of a nanoparticle, followed by a brief overview of applications of such

experimental systems. We introduce a theoretical description of a particle motion in a harmonic approximation as well as a nonlinear approximation based on an oscillator of a Duffing type. Then our novel methodology for a characterization of a nonlinear oscillator is proposed and described in detail. The method is based on averaging of recorded trajectories of a particle starting with the defined initial position and momentum. The obtained oscillator parameters are compared with the commonly used method based on the power–spectral–density evaluation [12, 27], and the validity of the innovative method is supported by numerical simulations. We show that the applicability of our technique is even in experiments performed at lower pressures, where the nonlinearity of the system starts to play an important role. The whole thesis is closed with concluding remarks pointing out the major results of the presented work.

I was involved mainly in the presented experimental part of the work, including designing and aligning of the described experimental setups, sample preparation, and performing all the presented experiments. The acquired data were processed mainly by other members of the group. I was closely involved in the following discussions on the obtained results. The detailed overview of my work is summarized at the end of the thesis on page 117.

1 PRINCIPLES OF OPTICAL TRAPPING

Light carries linear and angular momentum and thus can exert a force on objects by momentum exchange between light and matter. The invention of laser in 1960 by Theodore Maiman [1] introduced a breakthrough and a decade later Arthur Ashkin, awarded the Nobel Prize in Physics in 2018, demonstrated effects of the radiation pressure caused by a focused beam acting on latex microspheres freely suspended in water [29, 30]. He showed that two basic light forces, scattering force and gradient force, can accelerate, decelerate and stably trap microparticles. In 1986, Ashkin et al. reported the first experimental observation of the optical trapping of an object in three dimensions by a tightly focused beam, now referred to as optical tweezers [31]. Since then, it has been shown that the optical tweezers can trap and move objects ranging in size from tens of nanometres to tens of micrometres and this tool have found applications in various areas, for example biology [2], spectroscopy [3], nanotechnology [32] and material science [33].

For a facilitation of the theoretical description of the optical tweezers, there exist two limiting cases. One is for a spherical particle that is much larger than the trapping wavelength, called ray optics approximation [34]. If a radius of a sphere is much smaller than the wavelength of light, the theoretical description can utilize the dipole description, called Rayleigh approximation [35, 36]. For intermediate–scale particles or nonspherical particles, a more complex description of the optical forces has to be applied, typically the Lorenz–Mie scattering theory [37–39]. In the following, all three regimes are introduced and briefly described.

1.1 Ray optics

If a particle size is much larger comparing to the illumination wavelength, the ray optics approximation for the description of optical forces can be utilized [34]. A light beam is decomposed into a set of rays travelling in straight lines in a medium with a homogeneous refractive index. A change in their direction can be achieved only by the reflection or refraction at an interface of two media with different refractive indices. For the expression of optical forces, the ray–optics approximation employs tools for geometrical optics, namely Snell's law and Fresnel coefficients. The optical force acting upon an illuminated object then arises from the momentum exchange between light and matter when the ray is deviated.

An elementary explanation of the optical forces acting upon an object by means of the beam refraction is illustrated in Fig. 1.1. For clarity, only two representative trajectories of the incident photons N_1 and N_2 of a focused laser beam are shown. Due to the refraction, their direction and in consequence their momentum is changed

after the transmission through the object $\Delta\mathbf{p}_j = \mathbf{p}_{\mathrm{f}1} - \mathbf{p}_{\mathrm{i}1}$, where $j = 1, 2$. It defines the magnitude and the direction of the force acting on photons $\mathbf{F}_{\mathrm{phot}}$. Since the total momentum is conserved in the system, the difference between the initial and the final momentum of photons is transferred to the particle according to Newton's third law and the force exerted on the illuminated object by photons is then $\mathbf{F}_{\mathrm{obj}} = -\mathbf{F}_{\mathrm{phot}}$.

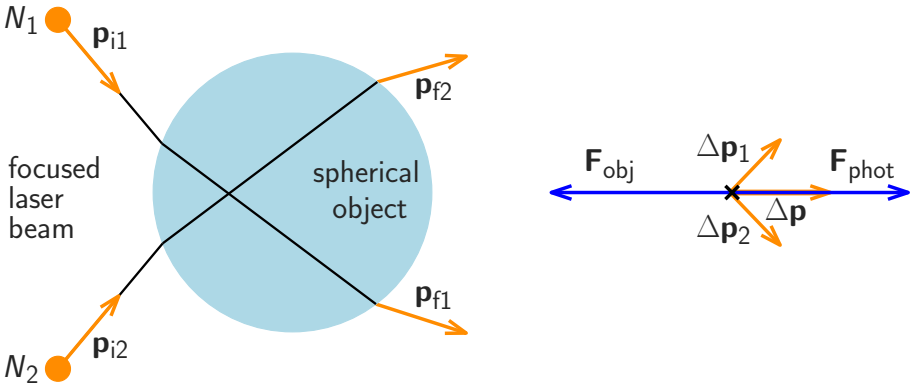

Fig. 1.1: Scheme of the origin of the optical force $\mathbf{F}_{\mathrm{obj}}$ acting on an object illuminated by a focused laser beam. For clarity, only two representative trajectories of the incident photons N_1 and N_2 are shown. A total momentum change of the incident photons $\Delta\mathbf{p} = \sum_j \left(\mathbf{p}_{\mathrm{f}j} - \mathbf{p}_{\mathrm{i}j}\right)$, where j is the photon number, defines the force acting on photons $\mathbf{F}_{\mathrm{phot}}$. Employing Newton's third law, the force exerted on the particle is then $\mathbf{F}_{\mathrm{obj}} = -\mathbf{F}_{\mathrm{phot}}$. The illustrated trajectories represents a case of a particle with a refractive index higher than that of the surrounding medium.

Even if this explanation of the optical forces acting on an illuminated object is a good illustrative approximation, it has some limitations in its utilization. The ray optics approximation can be used only for the spherical objects much larger than the illumination wavelength and moreover, it ignores the information about a phase of electromagnetic waves and all related interference effects. Another approximation utilized for the description of optical forces is for another limiting case, if a particle size is much smaller comparing to the wavelength. This approach is introduced in the following Section.

1.2 Rayleigh approximation

If a size of an illuminated object is much smaller than the wavelength of the incident radiation, the theoretical description can utilize the dipole approximation [35, 36]. In this so–called Rayleigh regime, a particle at position $\mathbf{r}$ and time t is approximated by an induced dipole immersed in an electric field $\mathbf{E}_{\mathrm{in}}(\mathbf{r}, t) = \mathbf{E}_{\mathrm{in}}(\mathbf{r})e^{-\mathrm{i}\omega t}$ with angular frequency ω. In the approximation, the electric field is considered homogeneous in the

whole particle volume and the induced dipole in the particle volume is proportional to the incident field $\mathbf{E}_{\mathrm{in}}$

$$\mathbf{p} = \alpha \mathbf{E}_{\mathrm{in}}. \tag{1.1}$$

The complex effective polarizability α can be approximated as [35, 40]

$$\alpha = \alpha_{\mathrm{CM}} \left(1 - \mathrm{i} \frac{k_{\mathrm{m}}^3 \alpha_{\mathrm{CM}}}{6\pi\varepsilon_{\mathrm{m}}} \right)^{-1}, \tag{1.2}$$

where $k_{\mathrm{m}} = 2\pi n_{\mathrm{m}}/\lambda_0$ is the light wavenumber in the dielectric, non–magnetic, non–absorbing medium surrounding the particle, λ_0 is the vacuum wavelength used for the optical trapping, n_{m} is the refractive index of the surrounding medium and ε_{m} is the dielectric permittivity of the medium. The coefficient α_{CM} is the static polarizability given by the Clausius–Mossotti relation

$$\alpha_{\mathrm{CM}} = 3V\varepsilon_{\mathrm{m}} \frac{\varepsilon_{\mathrm{p}} - \varepsilon_{\mathrm{m}}}{\varepsilon_{\mathrm{p}} + 2\varepsilon_{\mathrm{m}}}, \tag{1.3}$$

where V is the particle volume and ε_{p} the dielectric permittivity of the particle.

The total optical force $\langle \mathbf{F}_{\mathrm{DA}} \rangle$, averaged over the period of the electromagnetic field, acting on an induced dipole can be derived from the equations of motion using Maxwell's equations and we can arrive into the following expression [35]

$$\langle \mathbf{F}_{\mathrm{DA}} \rangle = \frac{1}{4} \Re \{\alpha\} \nabla |\mathbf{E}_{\mathrm{in}}(\mathbf{r})|^2 + \frac{n_{\mathrm{m}} \sigma_{\mathrm{ext,d}}}{c} \langle \mathbf{S}_{\mathrm{in}} \rangle - \frac{1}{2} c n_{\mathrm{m}} \sigma_{\mathrm{ext,p}} \nabla \times \langle \mathbf{s}_{\mathrm{in}} \rangle. \tag{1.4}$$

We introduced the time–averaged Poynting vector of the incoming field

$$\langle \mathbf{S}_{\mathrm{in}} \rangle = \frac{1}{2} \Re \{\mathbf{E}_{\mathrm{in}} \times \mathbf{H}_{\mathrm{in}}^*\}, \tag{1.5}$$

where $\mathbf{H}_{\mathrm{in}}$ is the incoming magnetic field, * indicates the complex conjugate and $\Re(f)$ and $\Im(f)$ denote the real and imaginary part of f, respectively. The time–averaged spin angular momentum density is denoted

$$\langle \mathbf{s}_{\mathrm{in}} \rangle = \mathrm{i} \frac{\varepsilon_{\mathrm{m}}}{2\omega} \mathbf{E}_{\mathrm{in}} \times \mathbf{E}_{\mathrm{in}}^* \tag{1.6}$$

and for the definition of the optical force we also used the extinction cross–section

$$\sigma_{\mathrm{ext,p}} = \frac{k_{\mathrm{m}}}{\varepsilon_{\mathrm{m}}} \Im \{\alpha\} \tag{1.7}$$

and the speed of light in vacuum c.

The optical force given by Eq. 1.4 can be separated into three terms: gradient, scattering and spin–curl force, respectively. The first term, called gradient force, can be rewritten into the form

$$\mathbf{F}_{\mathrm{DA,grad}} = \frac{1}{2} \frac{n_{\mathrm{m}}}{c\varepsilon_{\mathrm{m}}} \Re \{\alpha\} \nabla I_{\mathrm{in}}(\mathbf{r}), \tag{1.8}$$

where we introduced the intensity of the incoming electric field

$$I_{\mathrm{in}}(\mathbf{r}) = \frac{1}{2} n_{\mathrm{m}} c |\mathbf{E}_{\mathrm{in}}(\mathbf{r})|^2. \tag{1.9}$$

The direction of the conservative gradient force is given by the ratio between the refractive index of the object and that of the surrounding medium. Dielectric particles with a positive real part of the polarizability, i.e. the refractive index of the particle is higher than the refractive index of the surrounding medium, are attracted towards the highest intensity region of the optical field. On the other hand, particles with a negative real part of the polarizability are repelled from the area with a high intensity.

The second term in Eq. 1.4 states for the non–conservative scattering force. Due to extinction processes, i.e. scattering and absorption, the momentum of the incident light is transferred to the particle and the particle is pushed in the direction of the Poynting vector $\mathbf{S}_{\mathrm{in}}$. In order to optically trap a particle, the scattering force has to be counterbalanced by the gradient force. Since the gradient force is proportional to the field intensity gradient, the laser beams are usually focused by lenses with high numerical apertures to create the gradient force strong enough to trap stably an illuminated object.

The third term in the Eq. 1.4 represents a spin–curl force. The force is caused by the polarisation gradient in the incoming electromagnetic field and is non–conservative, too. The spin–curl force can be increased for example by means of cylindrical vector beams [41, 42], but usually the force is zero or very weak comparing to the gradient and scattering forces and, therefore, it does not play a major role in optical manipulation.

Two fundamental optical forces, gradient and scattering, acting upon a nanoparticle illuminated by a focused Gaussian laser beam are illustrated in Fig. 1.2. Due to the induced electric dipole in the object, the gradient force pointing to the area of a high intensity attracts the nanoparticle to the beam focus. The momentum change of photons incident on the nanoparticle gives rise to the scattering force, pushing the nanoparticle in the beam propagation direction. The illustrated total force is the sum of the presented gradient and scattering forces. The equilibrium position of the stably trapped nanoparticle is determined by the zero total force and is located slightly behind the focus.

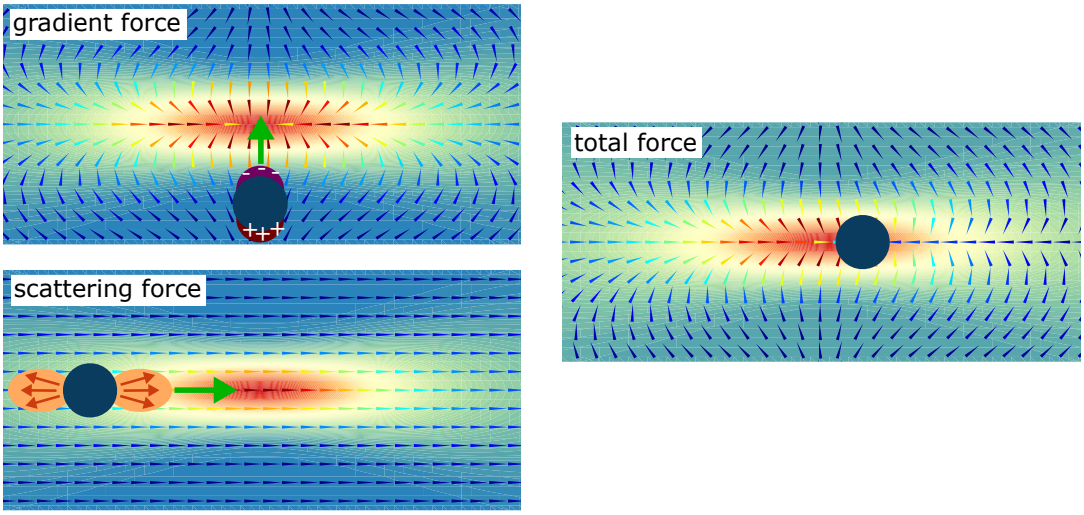

Fig. 1.2: Elementary explanation of the optical forces acting upon a nanoparticle illuminated by a focused Gaussian laser beam incident from the left. The gradient force points towards the high–intensity region (red). The scattering force pushes the particle by means of the photon momentum change. The total force is the sum of the gradient and scattering forces. The illustrated forces represents a case of a nanoparticle with a refractive index higher than that of the surrounding medium. Adapted from [43].

1.3 Lorenz–Mie theory

For nonspherical particles or intermediate–scale particles, the expression of the optical forces is more complex and this traditional identification of gradient, scattering and spin–curl forces is not so straightforward. As the size of the particle increases, the field retardation is no more negligible. The particle is not polarized homogeneously by the incident electromagnetic wave and thus the dipole approximation cannot be applied. For the description of the optical forces acting on a sphere in the intermediate regime, the Lorenz–Mie scattering theory [37–39] has to be utilized.

In this theory, the incident waves are decomposed into the spherical harmonic waves and the description of the mechanical interaction of light with matter is performed through the Maxwell stress tensor [44]. The whole theory is derived from the vectorial Helmholtz equation in the spherical coordinates, which is transferred into the scalar wave equation. The solution of the scalar Helmholtz equation can be expressed by the primary vectorial spherical harmonic functions. The final solution has the form of infinite series consisting of the spherical Bessel functions. A complete derivation of the Mie theory can be found for example in [45, p. 83].

2 OPTICAL BINDING IN TRACTOR BEAM

While a particle is illuminated by a laser beam, its motion is mainly driven by the photon flow due to the radiation pressure and the illuminated object is pushed by the scattering force along the beam propagation. In order to pull a particle against a direction of a wave vector **k** of an incident field, one has to usually employ the gradient forces. This phenomenon is also utilized for 3D optical trapping by a single optical tweezers (described in the previous Chapter) where a particle can be pulled by a strongly focused beam towards the center of the optical trap over the distance of several micrometers.

Recently, an increasing attention has been devoted to mastering a new technique that would enable to pull particles against the beam propagation over a long distance even if the beam has a uniform intensity profile along its propagation direction [46]. There have been developed several theoretical and experimental studies how to generate such an optical instrument with a long–range pulling force, called tractor beam. For example Jun Chen et al. proposed the use of a Bessel beam, where the optical pulling force acting on a dielectric particle in the Mie regime arose from the interference–enhanced forward scattering of multipoles excited by the incident beam [47]. A group of Helmut Ritsch theoretically proposed a pulling force generated via a multimode fibre by the injection of higher order modes [48]. Our group also proposed and experimentally verified a design of a tractor beam that is based simply on two interfering Gaussian beams [7, 49]. For creating a tractor beam, one can also take an advantage of gain media [50] or suitably designed chiral materials [51]. A lot of other approaches how to generate a tractor beam have been recently published [46, 52–59].

Generally, a behaviour of a single isolated particle optically trapped in a tractor beam is examined while more illuminated particles at once are often omitted for a complexity of the problem. But if we placed more objects in an optical field, usually various attractive phenomena, caused by the light–mediated interaction between illuminated particles, can be observed. The initial predictions of this effect, called optical binding, was proposed by Thirunamachandran [60] and followed by the pioneering experiments performed by Burns in 1989 [61, 62]. When two or more particles were present in an optical field, their motion became coupled due to their mutual optical interaction. Even an optical binding force was assumed to be weak compared to the optical gradient and scattering forces [62, 63], later it was shown that this long–range interaction can lead to ultrastable, rigid configurations of multiple micro- or nanoparticles free in solution, creating a flexible optical matter. Particles can be self–arranged for example into one dimensional chains in counter–propagating beams, standing waves or evanescent fields [64–69]. This one–dimensional soft matter

system might create a colloidal waveguide whose transmission spectrum can be tuned by adjusting the properties of the trapping beams [70, 71]. In the geometry of counter–propagating beams, even two– and three–dimensional optically bound structures can be generated and dynamically controlled [72]. In addition to the self–arrangements, optically bound spheroidal particles can exhibit phase locking behaviour through angular optical binding in beams with a certain helicity [73, 74].

The optical binding of microparticles was observed even in a tractor beam [7]. It was shown that this effect is responsible for significant changes in the total optical force acting on illuminated particles. For example, a chain of optically bound microparticles can be pulled by the tractor beam even if a single particle in the same tractor beam is pushed along the beam propagation direction. For now the sufficient explanation of this behaviour was missing and the experiments on the optically bound matter were focused only on two dimensional systems because of the tracking of particle positions from video images. In this Chapter we will focus on a fundamental explanation of the optical binding of microparticles in the tractor beam and its influence on the enhancement of the pulling force acting on the optically bound structure in three–dimensional space. At first, the principle of the tractor beam and optical–binding process is explained followed by the design of the experimental setup and the description of data processing. In Section 2.6 we compare our experimental observations of two optically bound microspheres in the tractor beam with the theoretical description demonstrating that the particle motion strongly depends on their mutual distance and spatial orientation.

This Chapter is based on our published results [8]. Experimental measurements together with the video data preprocessing were performed by the author of this thesis. Holographic video microscopy processing and theoretical analysis were done by Mgr. Lukáš Chvátal, Ph.D.

2.1 Principle of tractor beam

The working principle of the mentioned techniques for a tractor–beam formation is based on the asymmetric scattering pattern. An object is illuminated by a laser beam with a uniform intensity profile along the beam propagation direction and the gradient force is usually used only to trap the particle in a transversal plane. The pulling force attracting the particle towards the light source has the origin in the non–conservative force caused by the scattering the light off the particle. This fundamental principle of the tractor beam is schematically explained in Fig. 2.1. If the majority of photons hitting the particle are elastically scattered more in the forward direction, the horizontal component of the photon momentum increases

upon the scattering. Since the sum of the forces acting upon the scattered photons $\mathbf{F}_{\text{phot}}$ must be in the forward direction, from Newton's third law about the action and reaction the total optical force acting on an object $\mathbf{F}_{\text{obj}}$ points in the opposite direction, against the direction of the wave vector of the incident field

$$\mathbf{F}_{\text{obj}} = -\mathbf{F}_{\text{phot}} = -\sum_j \frac{\Delta \mathbf{p}_j}{\Delta t}, \tag{2.1}$$

where $\Delta \mathbf{p}_j$ is the momentum change for the j–th photon in the time interval Δt.

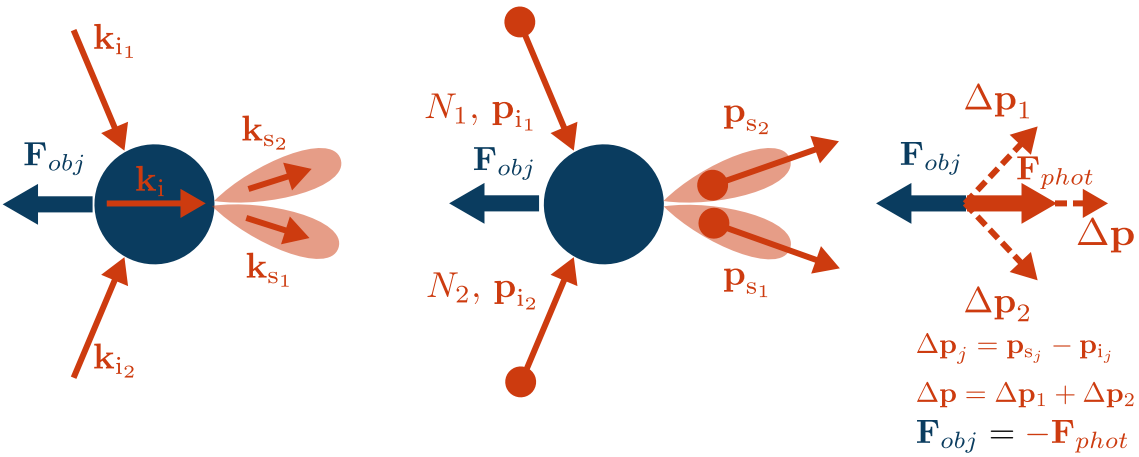

Fig. 2.1: An elementary explanation of the origin of optical pulling force $\mathbf{F}_{\text{obj}}$. For clarity, only two representative trajectories of the corresponding incident and scattered photons N_1, N_2 are shown, characterized by wave vectors $\mathbf{k}_{\text{i}1}$, $\mathbf{k}_{\text{i}2}$ and $\mathbf{k}_{\text{s}1}$, $\mathbf{k}_{\text{s}2}$, and by linear momenta $\mathbf{p}_{\text{i}1}$, $\mathbf{p}_{\text{i}2}$ and $\mathbf{p}_{\text{s}1}$, $\mathbf{p}_{\text{s}2}$, respectively. A total momentum change $\Delta\mathbf{p} = \sum_j \left(\mathbf{p}_{\text{s}j} - \mathbf{p}_{\text{i}j}\right)$, where $j = 1, 2$, defines the magnitude and the direction of the force acting on photons $\mathbf{F}_{\text{phot}}$. According to Newton's third law, the force exerted on the particle by scattered photons is $\mathbf{F}_{\text{obj}} = -\mathbf{F}_{\text{phot}}$. In this geometry, the horizontal component of the total force $\mathbf{F}_{\text{obj}}$ is oriented against the direction of the horizontal component of the incident wave vector $\mathbf{k}_{\text{i}}$. Taken from [43].

From the theoretical point of view, the expression of the optical force acting on an illuminated particle has to include in addition to the contribution of the electric dipole induced by the external optical field also the contribution of the induced magnetic dipole. Their interference creates an asymmetry between the forward and backward scattering pattern which can give rise to the pulling force effect. The

time–averaged optical force can be expressed as [75–77]

$$\begin{aligned}\langle \mathbf{F} \rangle =& \langle \mathbf{F}_{\mathrm{e}} \rangle + \langle \mathbf{F}_{\mathrm{m}} \rangle + \langle \mathbf{F}_{\mathrm{e-m}} \rangle \qquad (2.2)\\ =& \frac{\varepsilon_0 \varepsilon_{\mathrm{m}}}{2} \Re \left\{ \sum_{i=x,y,z} \alpha_{\mathrm{e}} E_{\mathrm{in},i} \nabla E^*_{\mathrm{in},i} \right\} + \frac{\mu_0}{2} \Re \left\{ \sum_{i=x,y,z} \alpha_{\mathrm{m}} H_{\mathrm{in},i} \nabla H^*_{\mathrm{in},i} \right\} \\ & - \sqrt{\mu_0 \varepsilon_0 \varepsilon_{\mathrm{m}}} \frac{k_{\mathrm{m}}^4}{12\pi} \Re \left\{ \alpha_{\mathrm{e}} \alpha_{\mathrm{m}} \mathbf{E}_{\mathrm{in}} \times \mathbf{H}^*_{\mathrm{in}} \right\}, \qquad (2.3)\end{aligned}$$

where μ_0 is the permeability of the medium. The electric and magnetic polarizabilities α_{e} and α_{m} can be expressed using the Mie scattering coefficients a_1 and b_1 [45, 76, 77]

$$\alpha_{\mathrm{e}} = \mathrm{i} \frac{6\pi a_1}{k_{\mathrm{m}}^3}, \qquad (2.4)$$

$$\alpha_{\mathrm{m}} = \mathrm{i} \frac{6\pi b_1}{k_{\mathrm{m}}^3}, \qquad (2.5)$$

which extends the validity of the Rayleigh approximation beyond its limits.

Time–averaged forces $\langle \mathbf{F}_{\mathrm{e}} \rangle$ and $\langle \mathbf{F}_{\mathrm{m}} \rangle$ come from the induced electric and magnetic dipoles, respectively. For a pure electric or a pure magnetic dipole, the far–field radiation pattern is symmetrically distributed between the forward and backward scattering. On the other hand, the third force $\langle \mathbf{F}_{\mathrm{e-m}} \rangle$ corresponding to the interference of the fields radiated by the electric and magnetic dipoles causes an asymmetry between the forward and backward scattering pattern. This force for a non–magnetic medium can be rewritten as follows [76]

$$\begin{aligned}\langle \mathbf{F}_{\mathrm{e-m}} \rangle =& - \sqrt{\frac{\mu_0}{\varepsilon_0 \varepsilon_{\mathrm{m}}}} \frac{k_{\mathrm{m}}^4}{12\pi} \Re \left\{ \alpha_{\mathrm{e}} \alpha^*_{\mathrm{m}} \right\} \Re \left\{ \mathbf{E}_{\mathrm{in}} \times \mathbf{H}^*_{\mathrm{in}} \right\} \\ & + \frac{\mu_0 k_{\mathrm{m}}^3}{12\pi} \Im \left\{ \alpha_{\mathrm{e}} \alpha^*_{\mathrm{m}} \right\} \left\{ \frac{1}{2} \nabla |\mathbf{E}_{\mathrm{in}}|^2 - \Re \left\{ (\mathbf{E}^*_{\mathrm{in}} \cdot \nabla) \mathbf{E}_{\mathrm{in}} \right\} \right\}. \qquad (2.6)\end{aligned}$$

In case of tractor beams where the field gradients should be negligible, the direction of $\langle \mathbf{F}_{\mathrm{e-m}} \rangle$ depends on the phase of the radiation emitted by the electric and magnetic dipoles [43]. If $\Re \left\{ \alpha_{\mathrm{e}} \alpha^*_{\mathrm{m}} \right\} > 0$, the dipoles radiate in phase and $\langle \mathbf{F}_{\mathrm{e-m}} \rangle$ points in a backward direction and acts against the radiation pressure. If this force overcomes the radiation pressure, a particle is pulled against the beam propagation direction. For the maximal force $\langle \mathbf{F}_{\mathrm{e-m}} \rangle$ pointing in the backward direction, i.e. when the backward scattering is zero, the first Kerker condition $\varepsilon_{\mathrm{p}} = \mu_{\mathrm{p}}$ has to be fulfilled [78], where ε_{p} and μ_{p} is the relative permittivity and permeability of a particle, respectively. On the other hand, the maximal force in the forward direction, i.e. when the backward scattering for a lossless magnetodielectric particle is strongest, is achieved under the second Kerker condition: $\varepsilon_{\mathrm{p}} = -\left(\mu_{\mathrm{p}} - 4\right) / \left(2\mu_{\mathrm{p}} + 1\right)$, when

the electric and magnetic dipoles oscillate out of phase and a particle is thus pushed in the beam propagation direction.

Apart from the tractor beams based on the asymmetric scattering pattern, there have been developed other techniques how to generate the pulling force. For example the long–range pulling force on a particle was achieved by the self–induced backaction–generated gradient force in a periodic photonic structure [79]. Other techniques for a pulling force generation were demonstrated theoretically using a directional excitation of surface plasmon polaritons [80], by an injection of higher order modes into an optical fibre [48] or by creating nanobubbles surrounding a plasmonic nanoparticle [81]. Many other conceptually different tractor beams based on optical–conveyor belts have been developed and theoretically and experimentally investigated [82–84].

2.2 Design of tractor beam

Recently, our group proposed and experimentally demonstrated a design of the tractor beam based simply on two interfering Gaussian beams where the pulling force arises from the asymmetric scattering pattern [7, 49]. The concept of the tractor beam is very similar to the technique theoretically proposed by Jun Chen et al. [47] where the projection of the total photon momentum along the propagation direction of the Bessel beam is small enough to create an attractive optical force that acts against the optical power flow. The principle of our tractor beam is schematically shown in Fig. 2.2. Two identical waves characterized by wave vectors $\mathbf{k}_1$ and $\mathbf{k}_2$ interfere under the large defined angle $2\theta_0$. It creates a standing wave where in the vertical direction an object is trapped in formed interference fringes due to the gradient force. In the horizontal direction, which is the direction of the overall photon momentum characterized by the total wave vector $\mathbf{k} = \mathbf{k}_1 + \mathbf{k}_2$, the particle motion is driven by the non–conservative force $\mathbf{F}_z$.

This force can point along or against the optical power flow in the z axis, depending on several parameters of the incident beams and the trapped object. One of the crucial parameters is a polarization of the tractor beam. The pattern of the optical field scattered by the trapped particle differs for the out–of–plane (s polarization) and in–plane (p polarization) polarized beams, see Fig. 2.2b and Fig. 2.2c, respectively. For some dimensions of optically trapped particles, in the s–polarized tractor beam, the majority of incident photons are scattered off a particle more in the forward direction. Hence the optical force acting on the particle is negative and pulls the particle against the beam propagation in the z axis. On the other hand, the photons in the p–polarized tractor beam are scattered in the backward direction

and consequently, the particle is pushed by the incoming field. Simply by rotating the polarization of the tractor beam it is possible to switch between the pulling and pushing force. Other important parameters that influence the magnitude and the direction of the non–conservative force, are the beam interference angle θ_0 and a particle size. Thus this technique can be utilized for sorting of particles of different sizes that are mixed in a colloidal suspension [7].

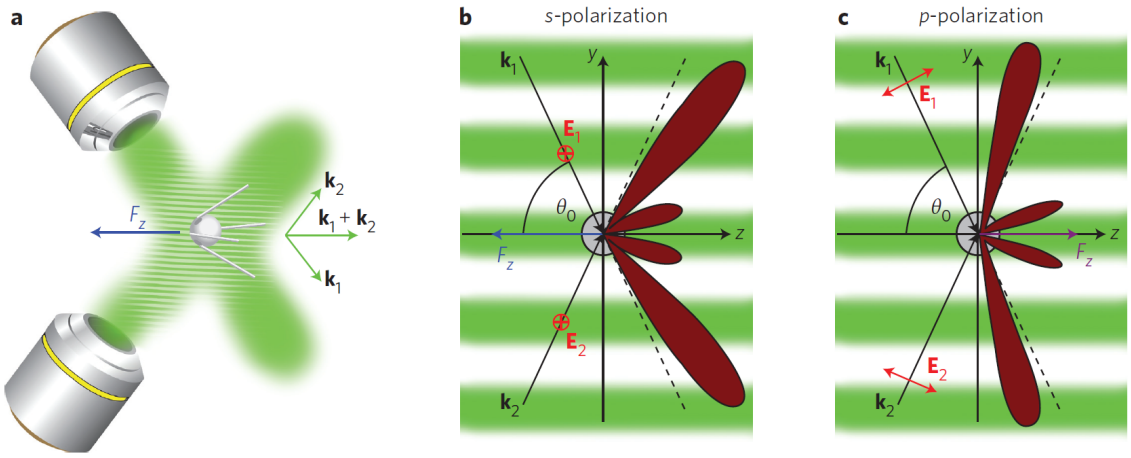

Fig. 2.2: Principle of the tractor beam. (a) Geometry of two beams described by wave vectors $\mathbf{k}_1$ and $\mathbf{k}_2$. (b) and (c) Illustration of the scattering for s– and p–polarized beams, respectively. In case of s–polarized light, the majority of the incoming photons are forward–scattered, causing the optical pulling force $\mathbf{F}_z$ oriented against the direction of the total wave vector $\mathbf{k} = \mathbf{k}_1 + \mathbf{k}_2$. And vice versa, p–polarized beams produce the pushing force. [7]

2.3 Optical binding

A behaviour of a single particle in the described tractor beam has been already comprehensively experimentally and theoretically analyzed [7]. However, it was observed that under certain circumstances the pulling force can appear or be significantly enhanced if a chain of microspheres is formed and optically transported [7]. Such a chain of particles is created through the optical binding caused by the scattering of the incoming light off the illuminated objects. This light–mediated interaction between particles can give rise to a creation of various systems of optically bound matter up to three–dimensional structures [62, 71, 72, 85–87].

Optical forces acting on two optically bound identical nanospheres illuminated by a plane wave can be described analytically. Assuming the Rayleigh regime, the optical interaction between particles is performed through the radiation of induced

dipoles representing the illuminated nanoobjects. The total electric field at position $\mathbf{r}_1$ of dipole 1 is given by a sum of the incident field $\mathbf{E}_{\text{in}}(\mathbf{r}_1)$ and the field emitted by a radiating dipole 2 at position $\mathbf{r}_2$

$$\mathbf{E}(\mathbf{r}_1) = \mathbf{E}_{\text{in}}(\mathbf{r}_1) + \bar{G}(\mathbf{r}_1 - \mathbf{r}_2)\,\alpha_2 \mathbf{E}(\mathbf{r}_2)\,, \tag{2.7}$$

as shown schematically in Fig. 2.3. The same expression applies for the electric field at the position of dipole 2. The total electric field affecting particle 2 is the sum of the incident field and the field radiated by dipole 1

$$\mathbf{E}(\mathbf{r}_2) = \mathbf{E}_{\text{in}}(\mathbf{r}_2) + \bar{G}(\mathbf{r}_2 - \mathbf{r}_1)\,\alpha_1 \mathbf{E}(\mathbf{r}_1)\,. \tag{2.8}$$

$\bar{G}(\mathbf{r}_1 - \mathbf{r}_2)$ is the field propagator between two dipoles in the form [88, 89]

$$\begin{aligned}\bar{G}(\Delta\mathbf{r}) = &\frac{e^{\mathrm{i}k_{\text{m}}\Delta r}}{4\pi\varepsilon_0\varepsilon_{\text{m}}\Delta r^3}\left[\left(-k_{\text{m}}^2\Delta r^2 - 3\mathrm{i}k_{\text{m}}\Delta r + 3\right)\frac{\Delta\mathbf{r}\otimes\Delta\mathbf{r}}{\Delta r^2}\right.\\ &\left. + \left(k_{\text{m}}^2\Delta r^2 + \mathrm{i}k_{\text{m}}\Delta r - 1\right)\bar{I}_3\right],\end{aligned} \tag{2.9}$$

where $\Delta\mathbf{r} = \mathbf{r}_1 - \mathbf{r}_2$, $\otimes$ represents the tensor product of two vectors and $\bar{I}_3$ is the identity matrix. The expression of the field propagator contains three terms with different dependences on the inter–particle separation $\Delta\mathbf{r}$ which divides the problem of the mutual interaction into three distance ranges. The term $(k_{\text{m}}\Delta r)^{-1}$ dominates in the far field, where $\Delta r \gg \lambda$, whereas the term $(k_{\text{m}}\Delta r)^{-3}$ dominates in the near field, where $\Delta r \ll \lambda$. The last term $(k_{\text{m}}\Delta r)^{-2}$ is crucial in the intermediate separation, where $\Delta r \simeq \lambda$.

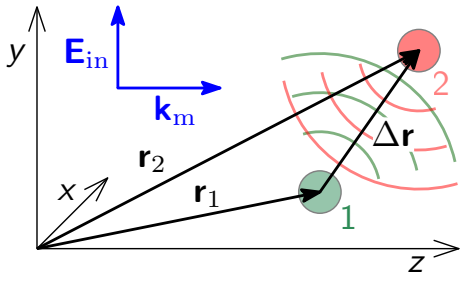

Fig. 2.3: Principle of optical binding of two particles. Particles at positions $\mathbf{r}_1$ and $\mathbf{r}_2$ scatter the incoming light which contributes to the total electric field affecting the second particle.

Solving Eqs. 2.7 and 2.8, one can arrive into an analytical solution for the electric field at the position of dipole 1 while dipole 2 is present, and consequently the expression for the optical force acting on the dipoles can be found, too [88]. In order to show illustratively the behaviour of the optically bound dipoles, we simplify the equations for the optical force and in the following, we focus on two types of the optical binding – lateral and longitudinal, in two separation regions, near field and far field.

2.3.1 Lateral binding

If the particles are optically bound perpendicularly to the propagation of the incident wave, the process of the light–mediated interaction is called lateral binding [61, 63, 90]. In the near field, the two identical dipoles ($\alpha_1 = \alpha_2 = \alpha$) tend to orient along the axis of the beam polarization [88]. Consequently, the induced dipoles have the same orientation, the positive end of dipole 1 is close to the negative end of dipole 2 and hence, they attract each other.

In the far field, the dominant force component is the radial force [88]

$$F_\mathrm{r} = \frac{|\alpha|^2 |E_\mathrm{in}|^2 k_\mathrm{m}^2}{8\pi\varepsilon_0\varepsilon_\mathrm{m}\Delta r^2}\left[k_\mathrm{m}\Delta r\left(\cos^2\varphi - 1\right)\sin\left(k_\mathrm{m}\Delta r\right) + 2\left(2\cos^2\varphi - 1\right)\cos\left(k_\mathrm{m}\Delta r\right)\right], \tag{2.10}$$

where E_in is the amplitude of the incident field and φ is the angle of $\Delta\mathbf{r}$ in the lateral plane with respect to the polarization of the incident beam, see Fig. 2.4a. The most stable lateral configurations are created if the dipoles are aligned perpendicular to the polarization, i.e. $\varphi = \pi/2$. The dipole separation in such configurations is determined predominantly by the first term in Eq. 2.10 due to its $1/\Delta r$ dependence on the inter–particle distance $F_\mathrm{r} \sim -\sin^2\varphi\sin\left(k_\mathrm{m}\Delta r\right)/\Delta r$. Therefore, for the stable configurations applies $\sin\left(k_\mathrm{m}\Delta r\right) = 0$, i.e. $k_\mathrm{m}\Delta r = 2\pi N$, where N denotes a larger natural number. One can clearly see that the stable configurations of the dipoles in the lateral binding differ by the wavelength in the surrounding medium $\Delta r = N\lambda_\mathrm{m}$. If the dipoles are optically bound along the polarization direction ($\varphi = 0$), the binding force follows as $F_\mathrm{r} \sim \cos\left(k_\mathrm{m}\Delta r\right)/\Delta r^2$. The stable configurations differ by λ_m, too, but the binding force is much weaker and decays faster because of the term $1/\Delta r^2$.

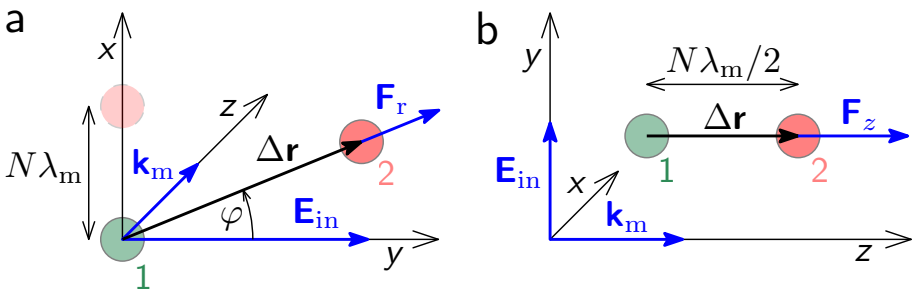

Fig. 2.4: Visualisation of the particle configurations and significant quantities during (a) lateral and (b) longitudinal binding.

2.3.2 Longitudinal binding

The second type of the optical interaction between particles is called longitudinal binding [87, 91]. In such a configuration the illuminated particles are optically bound along the propagation direction of the incident field, see illustration in Fig. 2.4b. In the near field, the interaction between two dipoles in the longitudinal configuration is repulsive [88] and thus this unstable system tends to orient into the lateral arrangement described above.

In the far field, the binding force between two dipoles is described as follows [88]

$$F_z = F_{z,2} - F_{z,1} = -\frac{\Re\{\alpha\}\, k_\mathrm{m}^3 |E_\mathrm{in}|^2}{4\pi\varepsilon_0\varepsilon_\mathrm{m}\Delta r}\left\{\Re\{\alpha\}\sin(2k_\mathrm{m}\Delta r) + \Im\{\alpha\}\left[\cos(2k_\mathrm{m}\Delta r) - 1\right]\right\}. \tag{2.11}$$

The particle separation in the stable configurations is then defined as $2k_\mathrm{m}\Delta r = 2\pi N$, i.e. $\Delta r = N\lambda_\mathrm{m}/2$, which is half the distance comparing to the lateral binding.

2.3.3 Optical binding of microparticles

Increasing a size of optically bound objects, the theoretical description of the mutual optical interaction becomes much more complex. The scattered field of only specifically shaped particles, such as spheres, spheroids and cylinders can be expressed analytically and the light–mediated interaction of these objects is treated using the multi–particle Mie scattering theory [11, 63]. This method also employs a superposition strategy for the description of the external field. Such an electric field external to n spherical objects is then represented by the superposition of the incident field and the field scattered off each sphere

$$\mathbf{E} = \mathbf{E}_\mathrm{in} + \sum_{i=1}^{n} \mathbf{E}_{\mathrm{s},i}, \tag{2.12}$$

where $\mathbf{E}_{\mathrm{s},i}$ is the scattered field of the i-th sphere. The incident and scattered fields are decomposed into the spherical Bessel and Hankel functions and a linear system of equations is solved for the scattering coefficients. Particles of more complex shapes have to be treated numerically, for example using the coupled dipole method [92], finite element method [93] or finite–difference time–domain method [94]. If illuminated objects are much larger than the wavelength of the incoming light, the ray optics approximation can be utilized [95].

Although the binding force acting on microparticles cannot be expressed in a simple form, it has been shown experimentally and numerically that the lateral–binding force acting upon microspheres illuminated by a plane wave oscillates with the laser wavelength as in the case of laterally bound nanoparticles [49]. Due to the radiation

pressure, the longitudinal binding is preferably studied in counter–propagating beams in order to compensate the scattering force [49, 68, 87]. It has been demonstrated that a separation of particles optically bound in counter–propagating beams is strongly dependent on a diameter and angle of trapping beams and a number of trapped particles [49, 68, 71, 72]. Therefore, the configuration of a self–arranged matter can be easily controlled by parameters of the trapping beam. It was observed that the binding force between two microparticles can be enhanced if the optically bound structure is placed close to a reflective surface [49]. Due to the presence of the reflective surface, both the lateral and longitudinal optical binding effects contribute to the particle self–organization.

In the tractor beam where the reflective surface is also present, an enhancement of the pulling force acting on optically bound matter was observed [7]. However, the origin of such behaviour of optically bound particles has not been sufficiently explained yet. Moreover, the system has been investigated only with particles trapped along one interference fringe because of the subsequent tracking of particles in video images. Therefore, in this study we focus on the case of two microspheres optically bound in arbitrary fringes in the tractor beam and provide an intuitive explanation of the optical binding process and the origin of particle motion.

2.4 Experimental setup

In addition to the tractor beam itself, another laser beam is utilized for the holographic video microscopy [9] in order to be able to detect positions of two particles in all three dimensions. An advantage of the holographic imaging for a particle 3D tracking is in a very large depth of focus without any need of mechanical motion of a sample nor an objective lens. These two crucial parts of the experimental setup – tractor beam and holographic video microscopy, are schematically shown in Fig. 2.5 and described in the following sections in more detail.

2.4.1 Tractor beam

Instead of using two independent beams that create the tractor beam as shown in Fig. 2.2, a single Gaussian beam with the incident angle α_0 was back–reflected onto a dielectric mirror placed under an aqueous solution with particles. The back–reflected beam created the standing wave where the particle could be trapped into interference fringes due to the gradient force and along the horizontal z axis the pushing or pulling motion could be observed. The polarization of the beam was rotated utilizing a half–wave plate and the angle of incidence was controlled by a

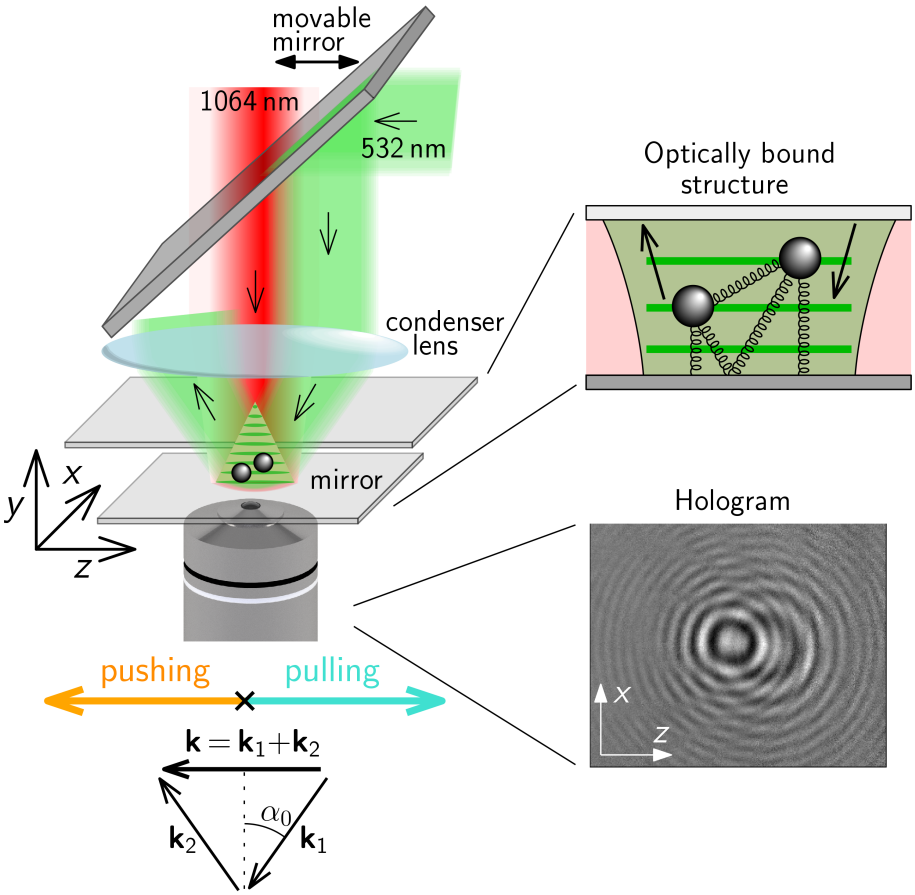

Fig. 2.5: Schematic illustration of the experimental setup. Polystyrene spheres with the radius of $a = 410\,\text{nm}$ are optically bound (illustrated in upper right image where the springs represent optical binding through the scattered light) in the tractor beam (green beam $\lambda_0 = 532\,\text{nm}$, the incident angle α_0) and illuminated by a 1064nm laser (red beam) utilized for holographic video microscopy (hologram shown in lower right image). Adapted from [8, 96].

movable mirror above the condenser lens that focused the incident beam onto a dielectric mirror.

For optical trapping we used a laser source Coherent VERDI V18 with the vacuum wavelength $\lambda_0 = 532\,\text{nm}$ and the incident power $P = 3.5\,\text{W}$ in the sample plane. The angle of incidence in a sample chamber was set to $\alpha_0 = 2.15\,^\circ$ and the narrow Gaussian beam was focused by a condenser lens with a focal length $f' = 150\,\text{mm}$ (Thorlabs AC508-150-A). It created a slightly focused beam with a beam waist radius $w_0 = 35\,\mu\text{m}$. Since the intensity profile along the horizontal plane was not uniform and was formed by the Gaussian beam profile, the motion of a particle in this plane was not driven only by the non–conservative scattering force but also by the gradient force that attracts an object to the beam center, to the area with the highest intensity. Once the particle was stably trapped, it meant that the gradient force and the pushing / pulling force were in equilibrium and the particle distance from the beam center could reveal the magnitude of the pushing / pulling force.

As an examined sample we used a colloidal suspension of polystyrene microspheres with a radius $a = 410\,\text{nm}$ (Duke Scientific Corporation). The original solution was diluted in water in ratio 1:25 000 and placed between two cover glasses that were separated by a 100µm spacer. The bottom cover glass served as a dielectric mirror for the reflection of the tractor beam. Using the electron beam evaporation technique, the bottom cover glass was covered by altering layers with higher and lower indices of refraction (TiO_2 and SiO_2 layers, respectively) in order to increase a reflectivity of the 532nm laser beam as much as possible and to increase the transmission of other wavelengths, especially the wavelength of 1064 nm used for the imaging. Both cover glasses were treated by a 1% solution of sodium dodecyl sulfate in order to prevent the particle sticking to the surfaces. The whole sample was fixed in a motorized 2D stage that could move the sample in the xz plane.

2.4.2 Holographic video microscopy

In this work we focus on two particles optically bound in different interference fringes in the tractor beam. In order to precisely determine three–dimensional positions of optically bound microspheres, we utilized a technique called holographic video microscopy [9, 10]. The holography method provides us with the complex information (3D position, shape, ets.) about the illuminated object written in an image as the name of the technique suggests; the word *holography* comes from the Greek words *holos* (whole) and *graphé* (writing or drawing). In a common arrangement, the laser beam is split into two branches, the object beam and another part as the reference beam. The object beam illuminates an object of interest and the scattered light

off the object interferes with the reference beam which creates an image called hologram. The holographic video microscopy utilizes only a single beam illuminating an object that is small comparing to the beam waist. The laser beam is scattered by a particle and the scattered field interferes with the undiffracted part of the illuminating beam that serves as a reference beam. It creates a resulting interference pattern, the hologram, where the information about the object position, its size, shape and index of refraction is encoded.

In our experimental setup, the optically trapped particles in the tractor beam were illuminated by another weak laser beam with a different wavelength and a wide waist (laser ADLAS GmbH & Co., the vacuum wavelength $\lambda_0 = 1064\,\mathrm{nm}$, the incident power $P = 5\,\mathrm{mW}$ and the beam waist radius $w_0 = 40\,\mu\mathrm{m}$). The irradiance was too weak to exert measurable forces on the illuminated objects, thus the illumination used for imaging had no detectable effect on the particle behaviour. The dielectric mirror placed under the aqueous solution was designed to reflect the wavelength of 532 nm and to transmit the wavelength of 1064 used for the imaging. In order to completely eliminate all the green light from hologram images, the notch filter for the wavelength of 532 nm was placed in the imaging path. The resulting interference pattern created under the illuminated particles was magnified by an objective lens (Olympus UPlanFl 100×, NA 1.5, oil immersion) placed on a 1D translational piezo stage for the objective refocusing and using a tube lens (focal length $f' = 200\,\mathrm{mm}$, Thorlabs AC254-200-C) the hologram image was projected on a CMOS chip (Basler acA640–750um), see Fig. 2.5 lower right image. This system provided an experimentally calibrated magnification of 85.6 nm/px.

2.5 Holographic tracking

Each recorded holographic image contains the information regarding the three–dimensional distribution of matter and its properties. The scattering of particles and its interference with the undiffracted portion of the laser beam can be theoretically described under certain conditions [97]. The basic principle of the holographic video microscopy is illustrated in Fig. 2.6. Assuming the incident illumination as a plane wave, the field propagating against the y axis is expressed as following

$$\mathbf{E}_{\mathrm{in}}\left(\mathbf{R}, y\right) = u_{\mathrm{in}}\left(\mathbf{R}\right) e^{-\mathrm{i}k_{\mathrm{m}}y}\mathbf{n}_{\mathrm{in}}, \tag{2.13}$$

where $u_{\mathrm{in}}\left(\mathbf{R}\right)$ is the transverse amplitude profile of the incident field in the position $\mathbf{R}$ in the xz plane and $\mathbf{n}_{\mathrm{in}}$ is the unit vector of the polarization. The wave scattered by an illuminated object with a complex amplitude $E_{\mathrm{s}}\left(\mathbf{R}, y\right)$ is defined in the following way

$$\mathbf{E}_{\mathrm{s}}\left(\mathbf{R}, y\right) = E_{\mathrm{s}}\left(\mathbf{R}, y\right)\mathbf{n}_{\mathrm{s}}\left(\mathbf{R}, y\right), \tag{2.14}$$

where $\mathbf{n}_\mathrm{s}(\mathbf{R}, y)$ is the polarization of the scattered field. The intensity profile in the focal plane $y = 0$ observed on a camera chip (see hologram in Fig. 2.6) is given by the superposition of the incident and scattered fields [9, 97]

$$I(\mathbf{R}, 0) = |\mathbf{E}_\mathrm{in}(\mathbf{R}, 0) + \mathbf{E}_\mathrm{s}(\mathbf{R}, 0)|^2 \tag{2.15}$$

$$= u_\mathrm{in}^2(\mathbf{R}) + 2\Re\{u_\mathrm{in}(\mathbf{R}) E_\mathrm{s}(\mathbf{R}, 0) \mathbf{n}_\mathrm{in}^* \cdot \mathbf{n}_\mathrm{s}(\mathbf{R}, 0)\} + |E_\mathrm{s}(\mathbf{R}, 0)|^2. \tag{2.16}$$

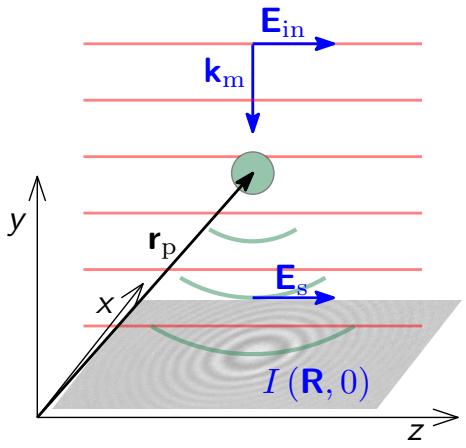

Fig. 2.6: Principle of holographic video microscopy used for 3D tracking of optically trapped particles. The incident field $\mathbf{E}_\mathrm{in}$ (red lines) is scattered by an illuminated particle at position $\mathbf{r}_\mathrm{p}$. The scattered field $\mathbf{E}_\mathrm{s}$ (green curves) interferes with the undiffracted incident light, which creates a hologram with an intensity profile $I(\mathbf{R}, 0)$.

The first term in Eq. 2.16 is the intensity measured when no object is in the field of view. Usually the illumination is not uniform and the hologram image is marred by speckle and fringes caused by reflections, refractions and scattering by surfaces and particles in the beam path, as it can be observed in Fig. 2.7a. These defects in the recorded image can be minimized by normalizing the recorded intensity profile $I(\mathbf{R}, 0)$ with a measured background image $|u_\mathrm{in}(\mathbf{R})|^2$. Since the background speckles in our experimental setup were slowly fluctuating in time, it was impossible to record the background image before or after the experiment with particles. We took an advantage of significantly moving particles across the whole field of view and the background value at each pixel was estimated as the median value of the intensities measured at each pixel [98]. In order to deal with drifts of the background intensity, the entire video was boxed into shorter sequences that were used for the background estimation from the median. An obtained reference image was subtracted from the measured interference pattern, the undistorted image of two particles is shown in Fig. 2.7b. The profile of the normalized hologram is described by the following equation [97]

$$b(\mathbf{R}) \approx 1 + 2\Re\{E_\mathrm{r}(\mathbf{R}, 0)\} + |E_\mathrm{r}(\mathbf{R}, 0)|^2, \tag{2.17}$$

where $E_{\mathrm{r}}(\mathbf{R}, y) = E_{\mathrm{s}}(\mathbf{R}, y) / u_{\mathrm{in}}(\mathbf{R})$ is the reduced scattered field and where we assumed the geometric rotation of the scattered polarization to be small, thus $\mathbf{n}_{\mathrm{in}}^{*} \cdot \mathbf{n}_{\mathrm{s}}(\mathbf{R}, 0) \approx 1$. This assumption is valid when the height of the object above the focal plane is greater than its size.

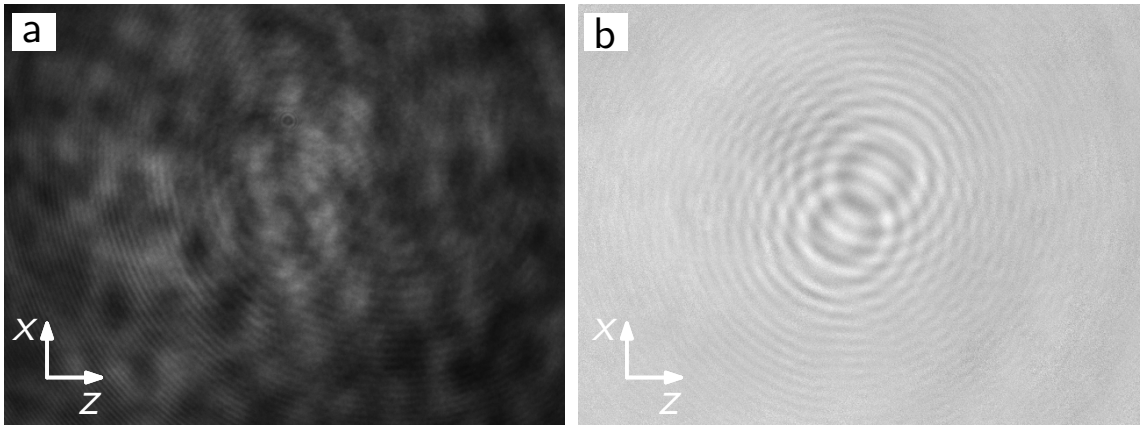

Fig. 2.7: (a) Recorded hologram of two particles with all interference defects. (b) Normalized hologram of two particles with the background subtracted.

Variations of the holographic video microscopy differ principally in how the normalized holographic snapshots are analyzed. There are two main approaches how to extract the information about object positions from the hologram image. A more precise determination of a three–dimensional position of an illuminated particle is performed by fitting the created interference fringes using Lorenz–Mie theory of a particle scattering theory [97, 99]. This method provide us with the additional information about a particle itself, its size, index of refraction and the index of refraction of the surrounding medium. But fitting the holograms of two or more particles is much more complex and therefore, a different procedure for a hologram analysis has been developed. It is possible to reconstruct the scattered field above the focal plane using the Rayleigh–Sommerfeld propagator [9, 10, 97] and the position of scatterers are determined as brightest spots in the volumetric reconstruction of the scattered field. In the following Sections these two methods are briefly described and the basic concept is explained.

2.5.1 Lorenz–Mie theory

Hologram images can be interpreted with Lorenz–Mie theory [97, 99] to obtain exceptionally precise measurements of individual microsphere dimensions and optical properties while simultaneously tracking their three–dimensional motions with a

nanometer–scale spatial resolution. This method works over the entire range of particle sizes and compositions for which Mie scattering theory applies, and requires only a single calibration of the experimental–setup magnification.

The scattered field in the focal plane in the transverse position $\mathbf{R}$ with the particle at position $\mathbf{r}_\mathrm{p}$ from the center of the focal plane can be written as [97]

$$\mathbf{E}_\mathrm{s}\left(\mathbf{R},0\right)=u_\mathrm{in}\left(\mathbf{r}_\mathrm{p}\right)\mathbf{f}_\mathrm{s}\left(k_\mathrm{m}\left(\mathbf{R}-\mathbf{r}_\mathrm{p}\right)\right), \tag{2.18}$$

where $\mathbf{f}_\mathrm{s}$ is the normalized scattering function. $\mathbf{f}_\mathrm{s}\left(k_\mathrm{m}\mathbf{R}\right)$ is described by Lorenz–Mie theory as an expansion in the vector spherical harmonics depending on size, shape and orientation of the illuminated object and a ratio of the object and its environment refractive indices. The normalized image is related to the calculated scattering pattern $\mathbf{f}_\mathrm{s}\left(k_\mathrm{m}\mathbf{R}\right)$ in the focal plane $y=0$ as follows [97, 99]

$$b\left(\mathbf{R}\right)=1+2\Re\left\{\mathbf{f}_\mathrm{s}\left(k_\mathrm{m}\left(\mathbf{R}-\mathbf{r}_\mathrm{p}\right)\right)\cdot\mathbf{n}_\mathrm{in}\right\}+\left|\mathbf{f}_\mathrm{s}\left(k_\mathrm{m}\left(\mathbf{R}-\mathbf{r}_\mathrm{p}\right)\right)\right|^2. \tag{2.19}$$

Knowing an analytic form for $\mathbf{f}_\mathrm{s}\left(k_\mathrm{m}\mathbf{R}\right)$, an experimentally recorded normalized hologram may be fit to Eq. 2.19 and all desired parameters of the object and its surrounding can be determined. However, the nonlinear least–square fits are computationally demanding and all evaluated parameters are not always desirable. Therefore, in order to determine only the 3D positions of illuminated object, Rayleigh–Sommerfeld back–propagation method can be generally utilized.

2.5.2 Rayleigh–Sommerfeld back–propagation method

Rayleigh–Sommerfeld back–propagation method [9, 10, 97] uses a hologram image to reconstruct the 3D optical scattered field that created the hologram. An advantage of such a reconstruction is in its exploitation for any hologram without knowledge of the scattering object shape, size or composition. It is also much less computationally expensive than Lorenz–Mie fits.

Since the field scattered by a particle spreads during its propagation, its amplitude should be substantially smaller than the illumination amplitude at the focal plane. Therefore, the second term in Eq. 2.17 dominates the third and the equation can be reduces to [9, 97]

$$b\left(\mathbf{R}\right)-1\approx 2\Re\left\{E_\mathrm{r}\left(\mathbf{R},0\right)\right\}. \tag{2.20}$$

Then the scattered field at height y above the focal plane could be characterized, if the complex scattered field at the focal plane was fully specified. The reconstructed scattered field would be calculated as the convolution [9, 10, 97]

$$E_\mathrm{s}\left(\mathbf{R},y\right)=E_\mathrm{s}\left(\mathbf{R},0\right)*h_y\left(\mathbf{R}\right), \tag{2.21}$$

where $h_y(\mathbf{R})$ is the Rayleigh–Sommerfeld propagator describing the field propagation along the optical axis [10]

$$h_y(\mathbf{r}) = -\frac{1}{2\pi}\frac{\partial}{\partial y}\frac{e^{\mathrm{i}k_\mathrm{m}r}}{r} \tag{2.22}$$

with $r^2 = R^2 + y^2$. Since only the intensity profile of the reduced scattered field at the focal plane is known, the field reconstruction has to be performed using the Fourier diffraction theory.

The Fourier transform of $b(\mathbf{R}) - 1$ is [9, 97]

$$B(\mathbf{q}) \approx U_\mathrm{r}(\mathbf{q}, 0) + U_\mathrm{r}^*(\mathbf{q}, 0), \tag{2.23}$$

where

$$U_\mathrm{r}(\mathbf{q}, y) = \int_{-\infty}^{\infty} E_\mathrm{r}(\mathbf{R}, y)\, e^{-\mathrm{i}\mathbf{q}\cdot\mathbf{R}}\mathrm{d}^2R \tag{2.24}$$

is the Fourier transform of $E_\mathrm{r}(\mathbf{R}, y)$. Using the Fourier convolution theorem, we arrive at the equation [9, 97]

$$B(\mathbf{q})\, H(\mathbf{q}, y) = U_\mathrm{r}(\mathbf{q}, y) + U_\mathrm{r}^*(\mathbf{q}, -y), \tag{2.25}$$

where

$$H(\mathbf{q}, y) = e^{-\mathrm{i}y\left(k_\mathrm{m}^2 - q^2\right)^{\frac{1}{2}}}. \tag{2.26}$$

The first term in Eq. 2.25 is the reconstructed field scattered by a particle while the second term is caused by a mirror image of a scatterer around the focal plane, which can highly disturb the examined scattered intensity profile. The effect of this artefact on the total reconstructed scattered field can be reduced by defocusing from a scatterer. This precaution is also required for our other assumptions that a polarization rotation is small and the scattered field is significantly less intense than the illumination field. Assuming a uniform illumination of a scatterer, the reconstructed scattered field is given by the following expression [9, 97]

$$E_\mathrm{s}(\mathbf{R}, y) \approx \frac{e^{\mathrm{i}k_\mathrm{m}y}}{4\pi^2}\int_{-\infty}^{\infty} B(\mathbf{q})\, H(\mathbf{q}, y)\, e^{\mathrm{i}\mathbf{q}\cdot\mathbf{R}}\mathrm{d}^2q. \tag{2.27}$$

The particle positions are then found as centres of the brightest spots in the reconstructed scattered intensity $I_\mathrm{s}(\mathbf{R}, y) \propto |E_\mathrm{s}(\mathbf{R}, y)|^2$.

Objects with dimensions smaller than the laser wavelength can be tracked in a 3D space with a high resolution using Rayleigh–Sommerfeld back–propagation method, even if the shape and composition of objects are unknown, while Lorenz–Mie fitting requires a specific model of the scattering function for all scatterers. On the other hand, the back–propagation method is not reliable for 3D tracking of objects

placed in polydisperse and heterogeneous medium. Another advantage of Lorenz–Mie tracking is in providing us with more information about a scatterer and more precise estimations of 3D positions. However, Lorenz–Mie fitting is computationally very demanding. For our purpose, the fitting to holograms created by two particles is even much more complex and therefore, we have chosen the Rayleigh–Sommerfeld back–propagation method for the tracking analysis.

Considering the uniform illumination and using the Fourier convolution theorem followed by the deconvolution [9], we reconstructed the 3D scattered field above the objective focal plane. In the reconstructed field maps, the particle positions were found as the brightest spots. The typical normalized hologram of two optically bound spheres is shown in Fig. 2.8a and its reconstructed scattered fields for different planes are shown in Figs. 2.8b–d, where the particle positions are indicated with the red cross marks.

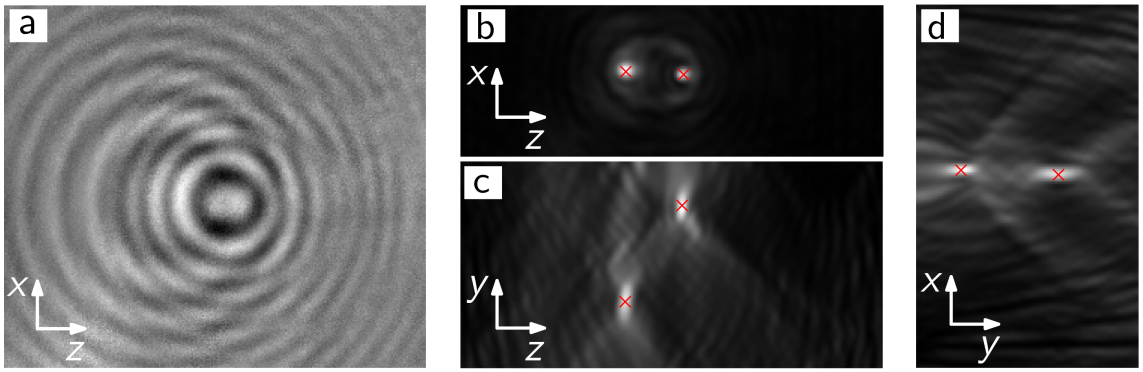

Fig. 2.8: (a) Normalized hologram of two particles with the background subtracted. Summed projection of reconstructed scattered intensities in (b) the zx plane, (c) zy plane and (d) yx plane. Red cross marks indicate positions of illuminated particles. [96]

2.6 Results

In this Section, the main experimental results supported by a theoretical study are presented. At first, a proof of principle of the tractor beam is shown. Then the optically bound particles moving in the tractor beam are studied, far from and close to the dielectric mirror placed under the colloidal solution.

2.6.1 A single particle in tractor beam

At first, we verified whether the tractor–beam setup described in Section 2.4 is working properly. A sample with polystyrene spheres of a radius $a = 410\,\mathrm{nm}$ was

examined. Particles of this dimension in the tractor beam with a wavelength in a water medium $\lambda_m = 400\,\text{nm}$ are highly responsive to the polarization of the laser beam. In the s–polarized tractor beam (out–of–plane polarization) a particle is pulled against the total wave vector $\mathbf{k}$ by the scattering force while the pushing of particles occurs for the p–polarized tractor beam (in–plane polarization), see the schematics of both processes in Fig. 2.9a. Since the beam intensity along the pushing / pulling direction has the Gaussian profile formed by the two interfering Gaussian beams, the gradient force plays a significant role, too. An illuminated particle can achieve a stable position where these two forces, gradient and scattering, are in equilibrium and thus an object does not escape the examined region close to the tractor–beam center.

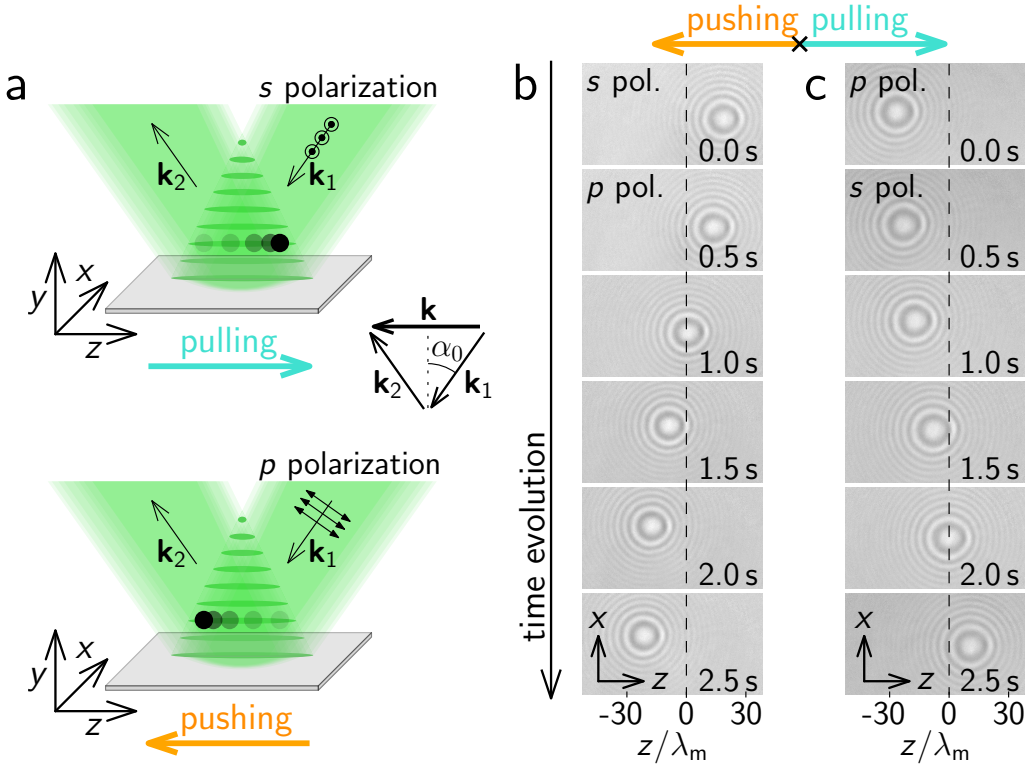

Fig. 2.9: (a) Schematic of pulling and pushing of a particle in the s– and p–polarized tractor beam marked with dots and arrows, respectively. A total wave vector $\mathbf{k}$ is composed by the incident and the reflected beams characterized by wave vectors $\mathbf{k}_1$ and $\mathbf{k}_2$, respectively. (b) and (c) Sequence of hologram images of a single polystyrene sphere of a radius $a = 410\,\text{nm}$. Dashed line marks the beam center at $z = 0$ and $\lambda_m = 400\,\text{nm}$ is the tractor beam wavelength in water. (b) s–polarized beam was switched to p–polarized beam and the pushing of a particle was observed. (c) p polarization was flipped to the s polarization and a particle was pulled against the total $\mathbf{k}$ vector.

A single particle was trapped in the s–polarized tractor beam, see hologram in the upper image in Fig. 2.9b. We could observe pulling of the trapped particle against the total $\mathbf{k}$ vector which was revealed by a particle stable position on the right side from the tractor beam center marked with the dashed line. Then the polarization of the tractor beam was flipped to the p polarization resulting in the pushing motion of the particle, as shown in the image sequence in Fig. 2.9b. This process is reversible and the experimental system works vice versa, too. If the polarization of the tractor beam was flipped from the p– to s–polarized light, the opposite direction of the particle motion could be observed, see the image sequence in Fig. 2.9c. A frame rate of the recorded video was set to 100 frames/s and an exposure time to 60 µs. This time was sufficiently short to minimize blurring caused by the particle moving with a speed of tens of µm/s. All following experimental results were performed with the same set of experimental parameters as described above unless otherwise defined.

By the presented fundamental experiment we proved the working principle of the tractor–beam setup for a single isolated particle. In this case, 3D mapping of the particle position by processing the acquired hologram images was not necessary. The 3D tracking of the particle motion is utilized in the following Sections, where we study a motion of a pair of optically bound particles. We show that a completely different behaviour can appear even if the experimental parameters remain the same as in the experiment with a single particle.

2.6.2 Particle pair optically bound far from a mirror

It has been already observed that, when more particles close to each other are illuminated in the tractor beam, they can behave in a different way comparing to a single particle [7]. Brzobohatý at al. [7] experimentally demonstrated that even though the set of experimental parameters in the tractor–beam setup remained unchanged, after particle assembling the pulling force was significantly enhanced comparing to a single particle. The pulling force acting on a structure of optically bound particles was observed even for the p–polarized beam while a single particle was simply pushed under these conditions. Here the particle assembling is studied in more detail and an explanation of a various behaviour of an optically bound structure is presented and supported by a theoretical analysis.

The observed self–arrangement of particles is caused by the light–mediated interaction between the illuminated particles. Particle 1 optically trapped in the tractor beam scatters the incident field that interferes with the tractor–beam field. It creates lobes with higher optical intensities, as illustrated in Fig. 2.10a, where the interference fringes caused by the tractor–beam standing wave are omitted for clarity. In fact, the scattering diagram of a microparticle is more complex, the scattering lobes

are illustrated just for an intuitive explanation. Due to the gradient force, particle 2 is attracted to the center of the scattering lobe of particle 1 (green lobes). The magnified region around particle 2 placed in the scattering lobe of particle 1 together with the intensity and the gradient–force profile is depicted in Fig. 2.11. In the same time, particle 2 scatters the incident field, too, which modifies the tractor–beam field and creates new areas (marked with red lobes in Fig. 2.10a) where particle 1 is optically trapped by the gradient force. The described mechanism causes the mutual optical binding of illuminated particles that can create a very stable structure with a specific internal configuration. Even in the optical field modified by the particle scattering, the tractor–beam field is still significant and particles are preferably trapped in the y axis in the tractor–beam interference fringes. If two particles are placed close to the dielectric mirror which is used for the tractor–beam reflection, the scattered field is reflected, too, and the profile of the optical field is modified, see Fig. 2.10b. This problem is described in Section 2.6.3 in more detail.

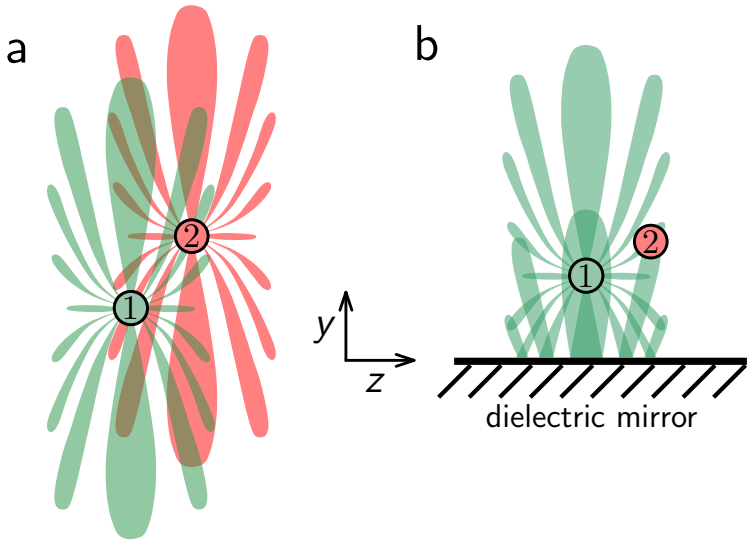

Fig. 2.10: Schematic configuration of a pair of optically bound particles and illustration of the higher intensity lobes created by the interference of the tractor beam and the field scattered by the illuminated particles. Horizontal interference fringes caused by the tractor–beam standing wave were omitted. (a) Particle pair far from a dielectric mirror. (b) Particle pair close to a dielectric mirror, where the scattered field is reflected. For clarity, only the scattering lobes of particle 1 are illustrated.

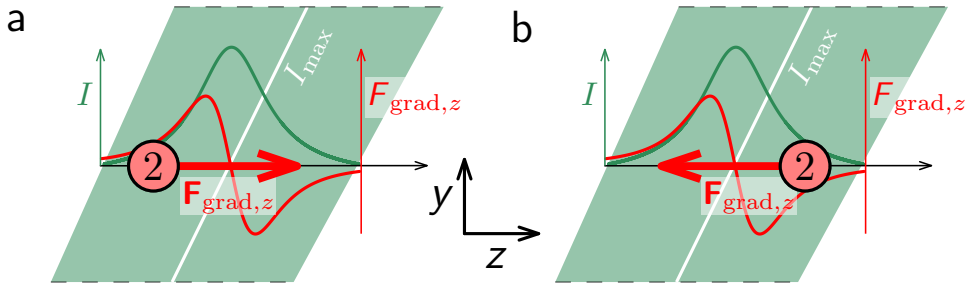

Fig. 2.11: The zoomed area of Fig. 2.10a around particle 2 optically bound in the scattered field of particle 1 (green area). Green curves represent intensity profile along the z axis of the total field originating from the tractor–beam field and the scattered field off particle 1. The red curves represent the magnitude of the corresponding gradient force $\mathbf{F}_{\mathrm{grad},z}$ that attracts particle 2 to the intensity maxima (white lines). Depending on the side where the particle is stably bound, the particle is moving (a) against or (b) along the total $\mathbf{k}$ vector of the tractor beam.

Experimental observations

In the following experimental procedures, the polarization was set to the out–of–plane polarization. Under these conditions, a single particle is pulled by the tractor beam, as we verified above. Now we focus on an optically bound pair of spheres optically trapped far from a dielectric mirror (about 50 μm), where the scattered field reflected onto a dielectric mirror is very weak to influence a particle motion. The typical behaviour of two optically bound spheres far from the dielectric mirror is shown in the hologram sequence in Fig. 2.12a. Surprisingly, even if the beam parameters remained unchanged during the whole experiment, the particle pair was pushed and subsequently pulled by the laser beam. From the recorded video, any significant change in the system could not be observed. Therefore we processed all the hologram video frames in order to determine precisely the particle positions during their motion using the Rayleigh–Sommerfeld back–propagation method.

The motion in the x direction was negligible thus we focused on the behaviour in the y and z axes. Calculated trajectories of both particles presented in the hologram sequence in Fig. 2.12a are plotted in Fig. 2.12b, see red and green curves. The regions of the observed pulling and pushing motion of the optically bound particle pair are indicated by the turquoise and orange background, respectively. The significant motion in the z axis, which is the axis of the pulling and pushing direction, was clearly visible and we could identify the position changes even from the video frames in Fig. 2.12a. But the holographic microscopy revealed remarkable changes during the investigated process also in the y axis. During the pushing motion (indicated by orange region between red cross marks i–ii in Fig. 2.12b) the particles were closer to

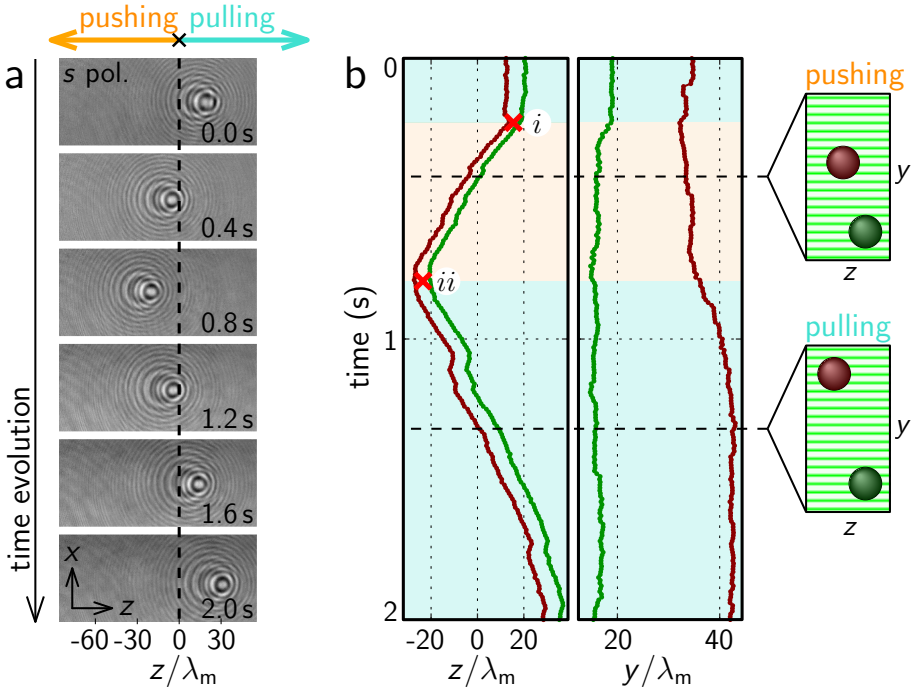

Fig. 2.12: (a) Typical sequence of hologram images with the subtracted background of two optically bound particles. Dashed line marks the beam center at $z = 0$ and $\lambda_m = 400\,\text{nm}$ is the tractor–beam wavelength in water. (b) Time dependence of positions of two optically bound particles in the z and y axes shown in (a). The y distance is calculated relatively to the focal plane. The orange and turquoise background corresponds to the pushing and pulling motion, respectively. The right images illustrate the internal configurations of the particle pair in two different regimes during the pushing and pulling. Red crosses highlight the positions where the motion direction was changed and interconnect experimental data with numerical calculations shown in Fig. 2.15a. Adapted from [8].

each other in the y axis comparing to the particle configuration during the pulling motion. The relative internal conformations of optically bound pairs in the tractor beam during the pushing and pulling motion are schematically illustrated in the upper and lower right images in Fig. 2.12b, respectively. This exemplary measurement demonstrated that the direction of the particle pair motion is strongly dependent on the internal configuration of the optically bound structure but it did not reveal the origin of changes in the motion direction. For the principle interpretation we had to utilize the theoretical analysis of the scattered field and optical forces acting on optically bound particles.

Numerical calculations of optical fields and forces

In our numerical model, the tractor beam was described by two interfering ideal plane waves. This description is valid close to the Gaussian beam axis where the particles were moving. The refractive index of a polystyrene sphere with a 820nm diameter was $n_{\mathrm{p}} = 1.59$ and the refractive index of the surrounding aqueous medium was $n_{\mathrm{m}} = 1.33$. The optical forces acting on individual spheres were calculated via the Maxwell stress tensor integrals [44] employing multipolar expansion of fields provided by the multi–particle Mie theory [11].

The field scattering problem was solved in a self–consistent way, i.e. enough reflections of the scattered field was taken into account in order to achieve a numerical convergence. If the separation between illuminated particles was greater than several wavelengths, the multiply scattered field off particles was very weak and its contribution to the total optical force was negligible. The optical force acting on optically bound particle 2 was predominantly determined by the tractor–beam field and the field scattered off particle 1 only once.

Calculated optical field modified by particle 1 scattering the incident field is illustrated in Fig. 2.13, where particle 1 is placed at the coordinate origin. The calculated optical intensity is shown in a logarithmic scale and averaged in the y axis over one–fringe length to remove the interference–fringe pattern. In order to show that the stable positions of optically bound particles are mainly determined by the center of scattering lobes, we calculated the extremes of the scattered field interfering with the incident tractor–beam field in the following way.

In our case, the tractor beam is described by two interfering plane waves characterized by wave vectors $\mathbf{k}_1$ and $\mathbf{k}_2$

$$\mathbf{k}_1 = [0, -k_{\mathrm{m}} \cos\alpha_0, -k_{\mathrm{m}} \sin\alpha_0] = [0, -k_y, -k_z]\,, \tag{2.28}$$

$$\mathbf{k}_2 = [0, k_{\mathrm{m}} \cos\alpha_0, -k_{\mathrm{m}} \sin\alpha_0] \quad = [0, k_y, -k_z]\,. \tag{2.29}$$

Then the tractor–beam electric field for the s–polarized beam is described as follows

$$\begin{aligned} E_{\mathrm{in},x} &= E_{\mathrm{in}} \exp\left[\mathrm{i}\left(-k_y y - k_z z\right)\right] + E_{\mathrm{in}} \exp\left[\mathrm{i}\left(k_y y - k_z z\right)\right] \\ &= 2E_{\mathrm{in}} \cos\left(k_y y\right) \exp\left(-\mathrm{i} k_z z\right). \end{aligned} \tag{2.30}$$

Few wavelengths from the particle, its scattered field can be represented by a propagating spherical wave

$$E_{\mathrm{s},x} = E_{\mathrm{in}} \frac{F_{\mathrm{s}}\left(\theta\right)}{k_{\mathrm{m}} R} \exp\left[\mathrm{i}\left(k_{\mathrm{m}} R + \phi_{\mathrm{s}}\left(\theta\right)\right)\right], \tag{2.31}$$

where F_{s} and ϕ_{s} are real functions characterizing the scattering of the s–polarized incident field $E_{\mathrm{in},x}$ in a direction $\theta = \arctan\left(z/y\right)$ and R is a radial distance from a scattering particle in the yz plane. The total electric field intensity is then

$$\begin{aligned} &|E|^2 = |E_{\mathrm{in},x} + E_{\mathrm{s},x}|^2 \\ &= 4|E_{\mathrm{in}}|^2 \cos^2\left(k_y y\right) + 4|E_{\mathrm{in}}|^2 \cos\left(k_y y\right) \cos\left[k_z z + k_{\mathrm{m}} R + \phi\left(\theta\right)\right] \frac{F_{\mathrm{s}}\left(\theta\right)}{k_{\mathrm{m}} R} + |E_{\mathrm{in}}|^2 \left(\frac{F_{\mathrm{s}}\left(\theta\right)}{k_{\mathrm{m}} R}\right)^2 \\ &\approx 4|E_{\mathrm{in}}|^2 \cos\left(k_y y\right) \left[\cos\left(k_y y\right) + \cos\left[k_{\mathrm{m}} R + \phi_{\mathrm{s}}\left(\theta\right) + k_z z\right] \frac{F_{\mathrm{s}}\left(\theta\right)}{k_{\mathrm{m}} R}\right]. \end{aligned} \tag{2.32}$$

The particle position is set to the maximum of the interference fringe along the y axis assuming

$$k_y y = \pi n, \tag{2.33}$$

where n is an integer. The scattering function $F_{\mathrm{s}}\left(\theta\right)$ is positive and varies slower with the position than the cosine terms. Then the condition for the constructive (destructive) interference of the tractor–beam and scattered fields yields

$$k_{\mathrm{m}} R + \phi_{\mathrm{s}}\left(\theta\right) + k_z z = \pi m, \tag{2.34}$$

where m is an integer with even (odd) values, respectively. Combining Eqs. 2.33 and 2.34, we arrive at the solution for the z coordinate

$$z = \frac{\left(\phi_{\mathrm{s}}\left(\theta\right) - \pi m\right) \sin\alpha_0 \pm \sqrt{\left(\phi_{\mathrm{s}}\left(\theta\right) - \pi m\right)^2 - \pi^2 n^2}}{k_{\mathrm{m}} \cos^2\alpha_0}. \tag{2.35}$$

For the p–polarized tractor beam, the derivation is analogical. Assuming a small value of α_0, we can arrive at the same condition as in case of the s polarization. Comparing to the exactly calculated optical intensity revealed that the value $\phi_{\mathrm{s}}\left(\theta\right) = \pi/2$ gives a very good coincidence. The curves defined by Eq. 2.35 are plotted in Fig. 2.13 denoting maxima (white curve) and minima (black curve) of the scattering lobes.

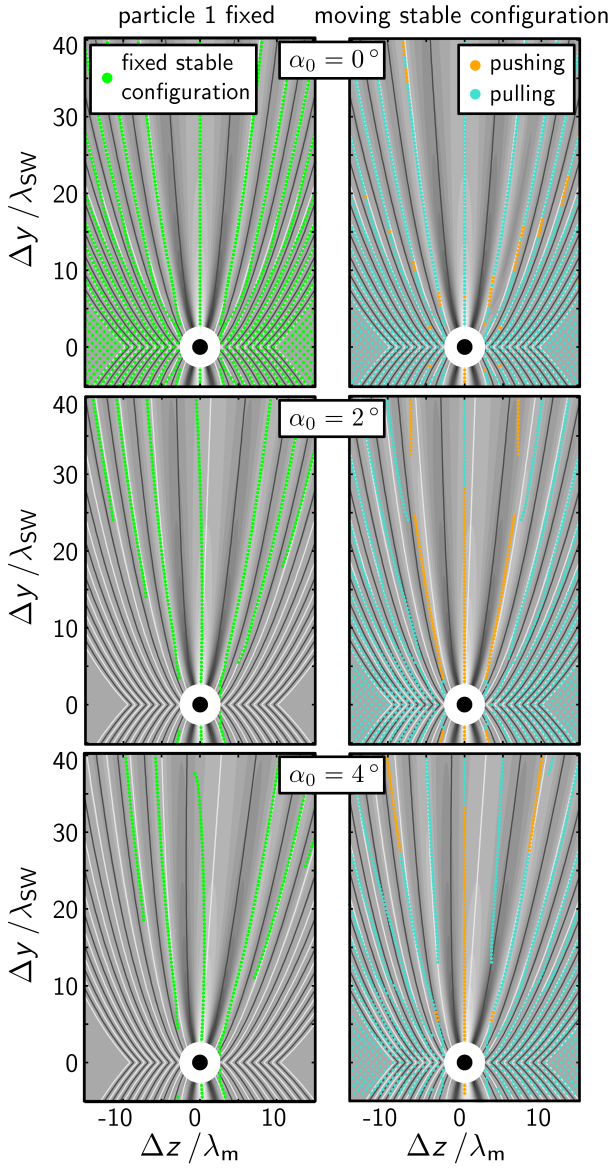

Fig. 2.13: Stable configurations of optically bound particle pairs in the s-polarized tractor beam for different incident angles α_0 for fixed particle 1 (left column) and moving stable configurations (right column). Particle 1 is marked with a black dot placed at the coordinate origin. Green dots denote stable positions of particle 2 while particle 1 is fixed. For the moving stable configurations, the positions of particle 2 are marked with orange and turquoise dots revealing the direction of motion, pushing and pulling, respectively. The y axis is normalized to the length of two interference fringes $\lambda_{SW} = \lambda_m / \cos\alpha_0$. The backgrounds show the optical intensity consisting of the tractor–beam field and the field scattered off particle 1 in a logarithmic scale, where the interference fringes caused by the tractor beam itself were artificially removed. White and black curves illustrate maxima and minima of scattering lobes given by Eq. 2.35, respectively. The white annulus around particle 1 indicates the range, where the particles are too close to each other to plot the data properly. Adapted from [8].

At first we calculated stable positions of particle 2 while particle 1 was held fixed in an interference fringe. Optically bound particle 2 remained tightly bound to the centres of interference fringes, except for very closest configurations, where the near fields shifted the centres by a little fraction of the wavelength in y. The stable configurations of optically bound particle pairs, i.e. where $\mathbf{F}_{2,z} = 0$, are shown in Fig. 2.13 in the left column for different incident angles α_0. Particle 1 is marked with a large black dot placed at the coordinate origin and all possible positions of particle 2 in the static equilibrium are represented by green dots in a relative distance to particle 1. It was found out that particle 2 is highly effected by the optical field scattered off particle 1 and is optically bound preferentially very close to maxima of the scattering lobes marked with almost overlapping white curves. Since the counter–propagating beams are tilted by an angle α_0, the binding process of two particles cannot be simply divided into the lateral or longitudinal binding. However, one can observe that in the horizontal direction ($y = 0$) the particles are separated about $\Delta r = N\lambda_\mathrm{m}$ as it was theoretically predicted for the lateral binding in Section 2.3. In the vertical plane, the particle separation is predominantly determined by the interference fringes which leads to the inter–particle distance about $\Delta r = N\lambda_\mathrm{m}/2$ in the y direction.

Since particle 1 was not fixed in the experiment, the stable configurations of an optically bound pair could be achieved if the inter–particle distance did not change during their motion. As the system of particles in aqueous medium is over–damped, the optical forces acting on particles of the same size has to meet the requirement $\mathbf{F}_{1,z} = \mathbf{F}_{2,z}$. The condition for the static equilibrium, when the optical forces acting on both particles are zero, are fulfilled only for counter–propagating plane waves with incident angle $\alpha_0 = 0$, i.e. $k_z = 0$. The stable configurations for the zero incident angle are shown in Fig. 2.13 in the upper right image. However, any nonzero incident angle breaks the mirror symmetry in the xy plane and stable configurations with constant inter–particle distances are the pairs of particles moving with the same velocity given by the optical forces acting on both particles. The stable moving configurations are plotted in Fig. 2.13 in the right column. There are much more stable configurations of moving particle pairs comparing to the case of the fixed particle 1. Particle 2 is optically bound again close to maxima of the scattering lobes but some cases deviate more from the white curves. The colour of dots reveals a direction of motion of a particle pair. Particle pairs in most configurations are pulled by the tractor beam, as a single isolated particle in the s–polarized tractor beam, but we can find ranges of inter–particle distances where the particle pair is pushed.

Principle of the motion direction

An intuitive explanation of the optical binding process and direction of the particle pair motion can be based on the description of the electric field of the tractor beam modified by the present particles. Particle 1 scatters the incoming field that interferes with the tractor beam. It creates high intensity lobes where particle 2 is attracted to due to the gradient force, as we demonstrated in our calculations presented in Fig. 2.13 and schematically showed in Fig. 2.11. Since the field creating the tractor beam is asymmetric due to the nonzero incident angle α_0, the particle cannot reach the intensity maxima of the lobes and stays aside, see Figs. 2.11 and 2.14. The optical gradient force acting on particle 2 causes its motion, which effects the stable positions of particle 1 attracted by the scattering lobe of particle 2. Thus the particles are mutually propelled by the gradient force toward the center of the scattering lobe running ahead. Depending on the side where the particles are stably bound, the whole structure is moving against or along the total $\mathbf{k}$ vector, demonstrating pulling and pushing motion, respectively, see Figs. 2.14a and 2.14b. In the vertical direction, particles are attracted to the interference fringes created by the tractor beam itself but the optical barrier can be overcome by the Brownian motion, as we observed in the experiment shown in Fig. 2.12b in the y axis.

The total optical force acting on particle 2 in the z axis can be decomposed into two components $\mathbf{F}_{2,z} = \mathbf{F}_{\mathrm{isol2},z} + \mathbf{F}_{\mathrm{int2},z}$, where $\mathbf{F}_{\mathrm{isol2},z}$ represents the force acting on an isolated particle 2 in the tractor beam (unfilled arrows in Fig. 2.14c) and $\mathbf{F}_{\mathrm{int2},z}$ is the interaction force arising from the presence of particle 1 (filled arrows in Fig. 2.14c). Since we consider the homogeneous incident beam and two identical particles, for the stable moving configuration has to apply $\mathbf{F}_{\mathrm{isol1},z} = \mathbf{F}_{\mathrm{isol2},z}$ and therefore $\mathbf{F}_{\mathrm{int1},z} = \mathbf{F}_{\mathrm{int2},z}$.

In the s–polarized tractor beam with the incident angle $\alpha_0 = 2.15\,^\circ$, a single 820nm polystyrene particle is pulled and $\mathbf{F}_{\mathrm{isol2},z}$ points against the total wave vector in the z axis. But the direction of particle pair motion and their velocities strongly depend on the interaction force $\mathbf{F}_{\mathrm{int2},z}$ that can be up to several times stronger than $\mathbf{F}_{\mathrm{isol2},z}$, see Fig. 2.14c. In the first scattering lobe, particle 2 is optically bound always on the right side of the center of the scattering lobe, see blue dots in Fig. 2.14c. Therefore the interaction force $\mathbf{F}_{\mathrm{int2},z}$ directing to the lobe maximal intensity, pushes the particle along the total $\mathbf{k}$ vector, which is opposite to the direction of the force acting on the isolated particle $\mathbf{F}_{\mathrm{isol2},z}$. The interaction force predominates over the isolated–particle force for short inter–particle distances and the optically bound pair is pushed in the tractor beam. Since the magnitude of the interaction force is getting weaker with the inter–particle distance, the total force switches between pushing and pulling when the inter–particle distance increases, see Fig. 2.15.

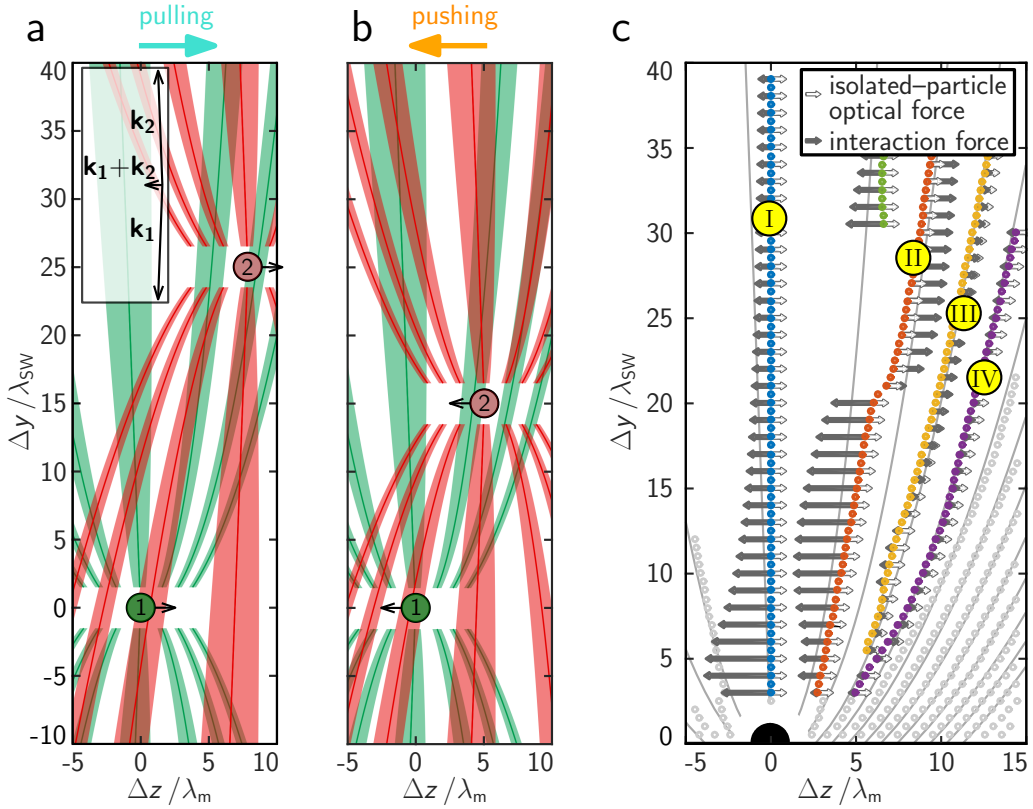

Fig. 2.14: (a) and (b) Schematic illustration of optically bound particles in scattering lobes revealing the direction of their motion (see black arrow marks) depending on the side where they are bound with respect to the intensity lobe maxima. Maxima of the scattering lobes are highlighted by lines with corresponding colours. (c) The forces acting on stably bound particles in the z axis. The total force acting on a particle can be decomposed into the force acting on an isolated particle in the tractor beam $\mathbf{F}_{\mathrm{isol2},z}$ (unfilled arrows) and the interaction force caused by the scattering off another particle $\mathbf{F}_{\mathrm{int2},z}$ (filled arrows), i.e. $\mathbf{F}_{2,z} = \mathbf{F}_{\mathrm{isol2},z} + \mathbf{F}_{\mathrm{int2},z}$. The scattering–lobe maxima are indicated by grey lines. Possible stable positions of an optically bound particle 2 are marked with dots. The colour of dots and Roman numerals connect the corresponding scattering lobes with the velocity calculations in Fig. 2.16. The calculations were performed for the s–polarized tractor beam with the incident angle $\alpha_0 = 2.15\,^\circ$. Adapted from [8].

The most interesting behaviour can be observed in the second and third lobes, marked with red dots in Fig. 2.14c. The stable positions in the certain distance jump from the second lobe to the third one and therefore, the interaction force changes its direction to opposite because the particles are optically bound on the other sides of the intensity lobe maxima (represented by grey lines). Since the interaction force is the leading force in the examined region, the optically bound pair of particles changes its direction of motion from pushing to pulling with the increasing inter–particle distance. In other scattering lobes, the isolated–particle force prevails over the interaction force and all other configurations of particle pairs in the investigated region are pulled by the tractor beam.

Comparison of experimental data and numerical calculations

Since the motion of particles in the tractor beam in an aqueous medium is over–damped, the velocity of a particle pair is proportional to the optical force. The calculated velocities of stably bound particle pairs are shown in Fig. 2.15. Each stable configuration is propelled with a different speed and in a different direction, as lengths and colours of arrowhead marks reveal, respectively. The change in the direction of the particle–pair motion in the first lobe discussed above is clearly visible, as well as the direction reversal when the particle stable position jumps from the second to the third lobe.

We compared the numerical simulations with the experimental results that are represented by the zigzag curve in orange and turquoise colour revealing the pushing and pulling motion, respectively. We found a perfect agreement between the numerical simulations and the experimental measurement shown in Fig. 2.12, see Fig. 2.15a. Particle 2 was preferably optically bound in the calculated stable moving configurations and the direction of the particle–pair motion corresponded to the numerical simulations, too. In the *i*–*ii* region between red cross marks the particle pair was pushed, as the numerical simulations predicted and the change in the motion direction was observed in the area between the second and third lobes, as expected.

More experimental trajectories of optically bound pairs were recorded, a few selected examples are shown in Figs. 2.15b–d. In most cases, particle 2 was predominantly optically bound in higher–order scattering lobes created by particle 1 and the whole particle pair was pulled by the tractor beam. However, we could find more examples, where the inter–particle position jumped from the second to the third lobe and the direction of particle–pair motion changed from pushing to pulling. Even in the higher–order lobe, where the pushing is expected, the particle–pair performance could be experimentally observed in accordance with the numerical predictions, see Fig. 2.15d.

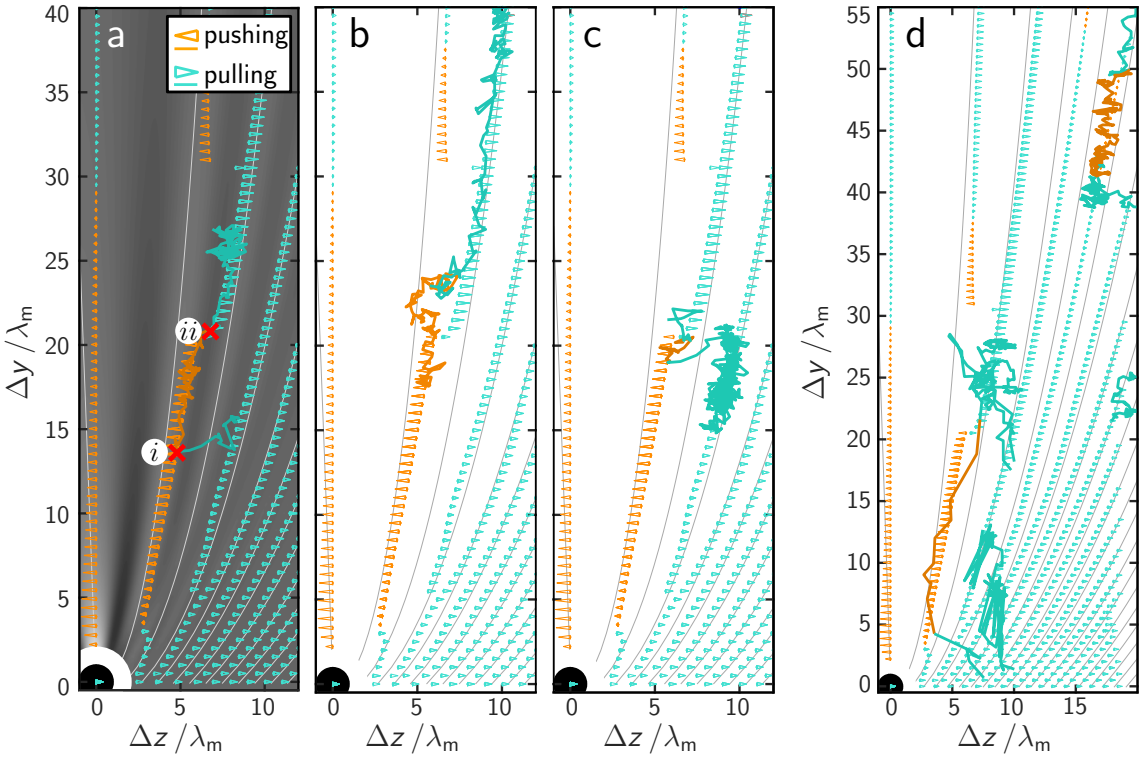

Fig. 2.15: Calculated velocities of optically bound pairs, where the magnitude and the direction of the velocity is encoded in the length (proportional to $\sqrt{v_{\mathrm{pair}}}$) and colour of the arrowhead marks, respectively. Experimental trajectories are marked with the zigzag curve, where the colour indicates the direction of motion. For comparison, the velocity of an isolated particle v_{isol} is shown at the coordinate origin. The scattering lobe maxima are illustrated by grey lines. The experiment and numerical calculations were performed for the s–polarized tractor beam with the incident angle $\alpha_0 = 2.15\,^\circ$. (a) The comparison is performed for the experimental trajectory shown in Fig. 2.12. Red cross marks indicate the i–ii region of the pushing motion. The background is proportional to the optical intensity consisting of the tractor–beam field and the field scattered off particle 1 in a logarithmic scale averaged in y over one fringe length. (b)–(d) Other measured trajectories of particle pairs are compared with the numerical calculations. Adapted from [8].

Velocity of an optically bound pair

The theoretical and experimental comparison of magnitudes and directions of velocities of particle pairs v_{pair} and a single isolated particle v_{isol} is performed in Fig. 2.16. The colours of plotted curves and Roman numerals indicate the corresponding scattering lobe with the calculated stable positions of optically bound particle 2 shown in Fig. 2.14c. The experimental data identified by cross and round marks are influenced by the Gaussian profile of the tractor beam but even so, we can observe a good agreement between the experimental measurements and the theoretical predictions. Comparing to a single isolated particle in the tractor beam, the velocity of an optically bound particle pair can be enhanced up to 4×, both for pushing and pulling motion. The dashed curves indicate calculations including the hydrodynamic interaction between particles [100] but the shift in the velocity is not significant. It reveals that the observed behaviour is mainly of the optical origin.

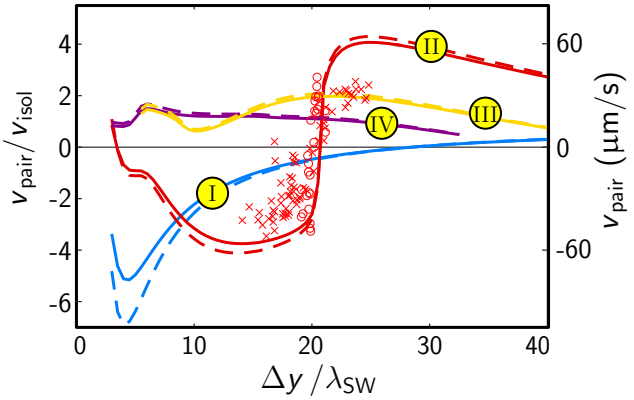

Fig. 2.16: Particle pair velocities v_{pair} compared to the velocity of an isolated particle v_{isol} for the selected configuration groups denoted by the colour and Roman numbers as in Fig. 2.14c. Different marks correspond to different experimental data set with the same experimental conditions. Dashed curves represent calculations including the hydrodynamical interaction between particles. We considered the s–polarized tractor beam with the incident angle $\alpha_0 = 2.15\,^\circ$ and incident power density $1.8\,\mathrm{mW{\cdot}\mu m^{-2}}$. [8]

In order to show the diverse behaviour of the optically bound pairs, we calculated the pair velocities for different incident angles α_0, see Fig. 2.17. The pair velocities of all possible stable configurations in the same investigated region of the inter–particle distances as in Fig. 2.15a are marked by grey segments. For comparison, a velocity of a single isolated particle for corresponding incident angles is pictured, indicated by the yellow curve. For some incident angles of the tractor beam, there exist configurations of the optically bound pair whose velocity enhancement along the z axis

is even by an order higher comparing to a single isolated particle. Although a single particle in the p–polarized tractor beam is pushed, the optically bound structure can be pulled revealing that in case of optically bound structure, its direction of motion is strongly dependent on the internal configuration rather than on the behaviour of a single particle in the same tractor beam.

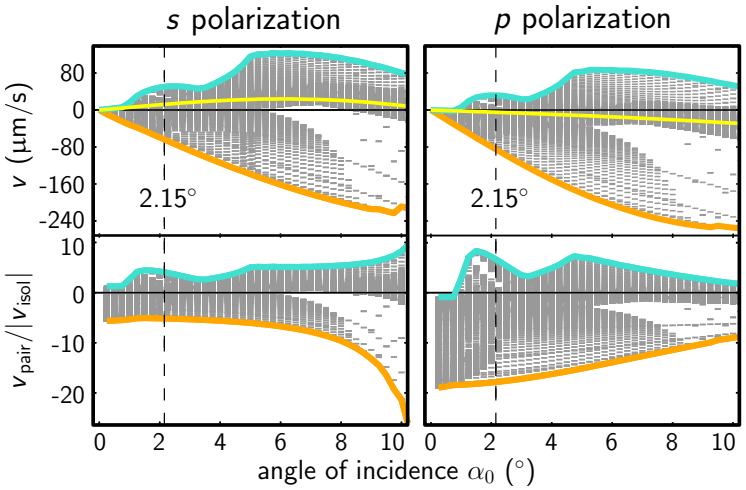

Fig. 2.17: Comparison of calculated velocities of optically bound particle pairs v_{pair} for different incident angles α_0 of the tractor beam and both polarizations. Each grey segment corresponds to one stable configuration of the particle pair in the same region of the inter–particle distances as in Fig. 2.15a. The velocity extremes are highlighted with thick curves in orange and turquoise colours corresponding to pushing and pulling, respectively. The yellow curve represents a velocity of a single particle v_{isol}. We considered the incident power density $1.8\,\mathrm{mW{\cdot}\mu m^{-2}}$. [8]

2.6.3 Particle pair optically bound close to a mirror

If optically bound particles are placed close to the reflective surface, the interaction between them is even more complex. Due to the presence of the mirror, the reflected scattered field of both optically bound spheres plays a significant role, as we illustrated in Fig. 2.10b.

Experimental observations

In our experiments, we could observe optical binding of particles near the reflective surface that was primary used for the creation of the tractor beam. Two different examples of experimental measurements of optically bound pair at a distance from the mirror $y_{\mathrm{M}} \approx 9.6\,\mu\mathrm{m}$ are shown in Fig. 2.18a. In order to simplify the problem,

we focused on the particles optically bound at the same distance from the mirror, i.e. particles were aligned along the z axis while $\Delta y \approx 0$.

A behaviour of the upper pair pictured in Fig. 2.18a is very similar to that of a single isolated particle in the tractor beam. In the s–polarized tractor beam, an optically bound pair was pulled against the total wave vector, while the pushing force occurred in the p–polarized tractor beam. Another pair of optically bound particles with a longer inter–particle distance was pulled by the tractor beam stronger comparing to the aforementioned pair, see the lower image in Fig. 2.18a. A magnitude of the pulling force was revealed by the distance from the beam center at $z = 0$ because the pulling force in the steady–state of the particle pair had to be in balance with the gradient force arising from the Gaussian beam profile of the trapping beam. In the p–polarized tractor beam, the particle pair was pulled, too, but the pulling force was weaker comparing to the s polarization.

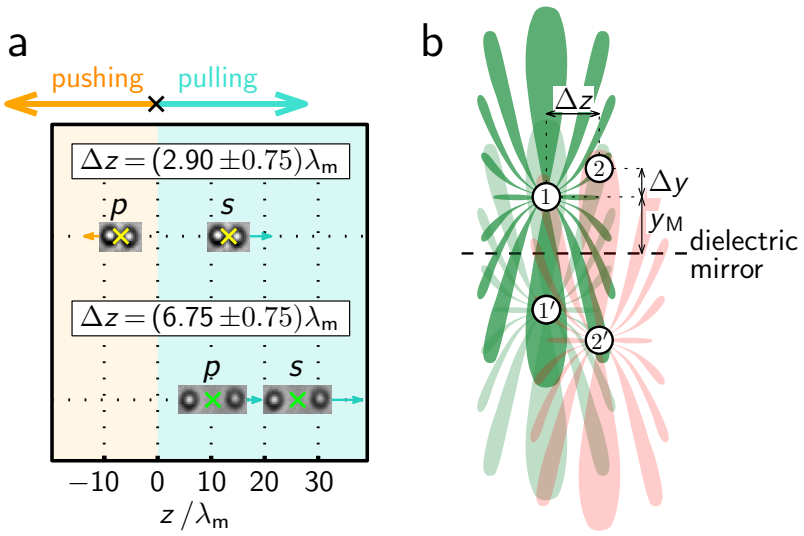

Fig. 2.18: (a) Experimental observations of the optically bound pair in its stable position for the p– and s–polarized tractor beam with the incident angle $\alpha_0 = 2.82\,^\circ$ close to the dielectric mirror ($y_\mathrm{M} \approx 9.6\,\mu\mathrm{m}$) for two different inter–particle distances. [8] (b) Schematic configuration of a pair of optically bound particles close to the dielectric mirror and the illustration of their scattering lobes. In the calculations of the scattered field affecting particle 2, the contribution of the field scattered off particle 1 is enhanced by the fields scattered off the mirror images of particle 1 and particle 2 represented by particle 1' and particle 2' and their scattered fields.

Comparison of experimental data and numerical calculations

In the numerical calculations, the optical field driving the particles is more complex than in case of optically bound objects far from the mirror. Due to the presence of the reflective surface, both the lateral and longitudinal optical binding effects contribute to the particle self–organization. The scattered field off particle 1 affects directly the illuminated particle 2 in the vicinity of the scatterer and simultaneously, the scattered field is reflected onto the reflective surface. Thus the total field affecting particle 2 consists of four contributions: the incident tractor beam, the field scattered off particle 1 and the reflected scattered field of particle 1 and 2. Instead of calculating the reflection of the scattered field at the reflective surface, we considered mirror images in the corresponding distances on the other side of the mirror, see particle 1' and particle 2' and their scattered fields in Fig. 2.18b.

Calculated optical fields with all contributions for different distances from the mirror y_{M} are depicted in Fig. 2.19 together with the maxima of the scattering lobes marked with grey lines. In case of $y_{\mathrm{M}} = \infty$, the reflective surface is missing and the situation is the same as described in the previous Section. Approaching the mirror, a number of stable positions of optically bound particles decreases, but they are still preferably formed near the maxima of the scattering lobes. Examining the calculated velocities of stably formed configurations we can see the problem complexity. For instance approaching the mirror, pair configurations pulled by the p–polarized tractor beam are revealed while in the s–polarized tractor beam both directions of motion exhibit in any distance from the mirror, depending on the internal structure of particles.

Our experimental observations correspond to the numerical calculations in the last row in Fig. 2.19, where yellow and green shaded areas indicate the experimentally measured separations between particles in the z axis. For a shorter distance between particles (yellow area), the pushing motion in the p–polarized tractor beam is distinctive while for the s polarization, the pulling motion occurs only for particles in the same height above the mirror, which confirms the alignment of the investigated particles. For more distant particles (green area), the pulling behaviour for the s polarization is more convincing and the pulling force is stronger, as we observed in the experiment. In the p–polarization alignment, the direction of motion alternates with Δy and the optical forces in both directions are rather weak.

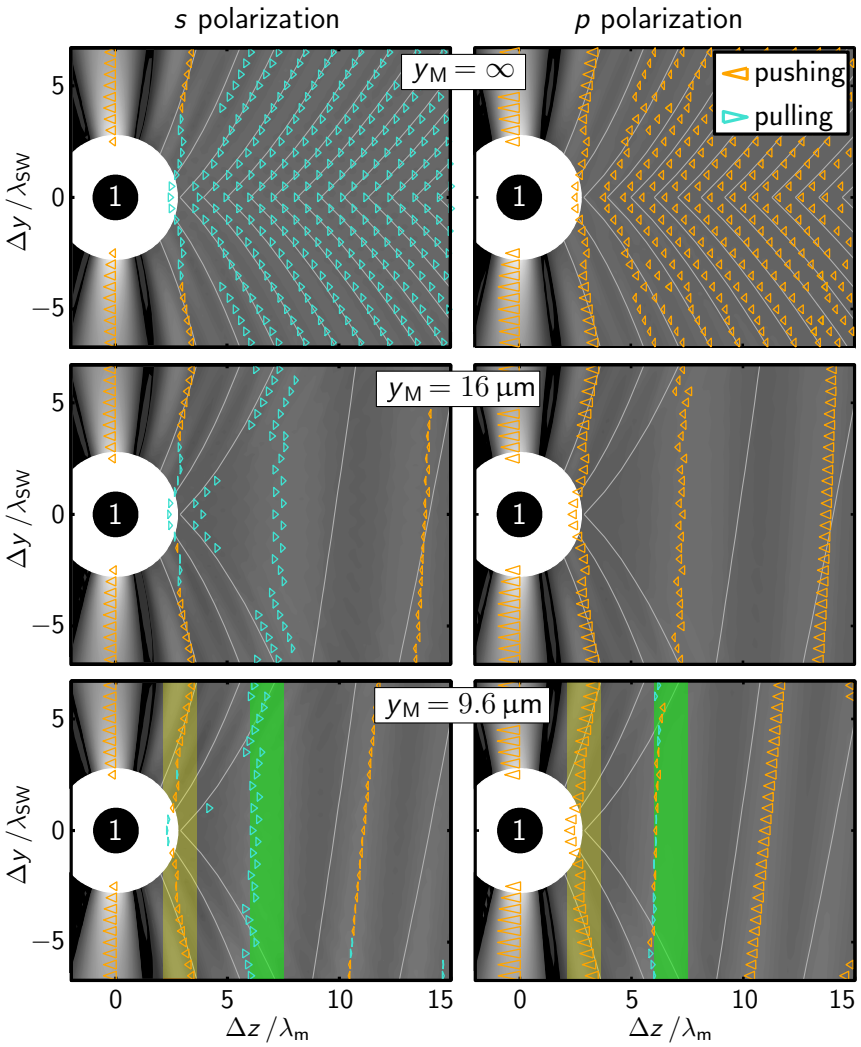

Fig. 2.19: Calculated velocities of optically bound pairs for different distances from the mirror y_M, where the magnitude and the direction of the velocity is encoded in the length (proportional to $\sqrt{v_{pair}}$) and colour of the arrowhead marks, respectively. The background is proportional to the optical intensity in a logarithmic scale averaged in y over one–fringe length, where the scattered field is taken as the sum of the field scattered off particle 1, its mirror image 1' and the mirror image of particle 2', shown in Fig. 2.18b. The scattering lobe maxima are illustrated by grey lines. The green and yellow shading corresponds to the shorter and longer observed inter–particle distances in Fig. 2.18a, respectively. The experiment and numerical calculations were performed for the s– and p–polarized tractor beam with the incident angle $\alpha_0 = 2.82\,°$. [8]

2.7 Conclusions

We have demonstrated that optically bound matter in the tractor beam displays a rich dynamical behaviour. In order to track the particle motion in three dimensions, we utilized the holographic video microscopy technique that could reveal the 3D positions even of multiple particles. We have shown that the direction of motion of optically bound particle pair is strongly dependent on the internal structure configuration and the speed of the objects can be by an order enhanced comparing to a single isolated particle in the same tractor beam. We have described an intuitive explanation of the behaviour of the optically bound structure in the tractor beam and showed that the particle pair is mutually propelled and its pushing and pulling motion is caused by the asymmetry in the incident tractor beam and subsequently in the optically bound structure and particle scattered fields. Investigating and describing underlying physical phenomena gives us new possibilities to control self–organization of illuminated particles and perform their sorting and transport in structured light fields.

3 PARTICLE LEVITATION

The pioneering experiments on optical levitation of particles were performed by Arthur Ashkin in 1970 and 1971 [29, 101] when he successfully demonstrated optical trapping of particles in air or even vacuum at pressure around 1 mBar. He indicated that it is possible to achieve an extremely low dissipation while trapping a particle in a high–vacuum environment. At low ambient pressure, optically levitated particles are decoupled from a thermal environment and an energy dissipation through strain vanishes. Therefore, a measurement sensitivity could be highly improved and levitated particles could be utilized as gyroscopes and accelerometers. The first experimental setup of an optical trap in a high–vacuum environment was demonstrated by A. Ashkin few years later and the optical trapping of oil droplets in vacuum down to 10^{-6} mBar was performed [102].

However, nowadays optically trapped micro- and nanoobjects are usually dispersed in water or other viscous media because of their applications particularly in the field of biology [2], where an isolation of a single particle from its environment is not desirable. A dynamics of such a particle in a viscous medium is overdamped with a negligible influence of particle inertia. But recently, there has been a renewed interest in optical trapping in air with reduced pressure up to high vacuum [12–16, 27, 103, 104], motivated by a prediction of entering the quantum regime [105–107]. It has led to a development of a new field called levitated optomechanics [108–110]. Unlike other optomechanical systems, a levitated object is not attached to any substrate. Therefore, an optically trapped particle does not suffer from clamping losses and is a very attractive tool due to an easy control of system parameters and its high sensitivity to the surrounding environment.

Thanks to the unique properties of the levitated optomechanical system, a levitated particle has attracted a great attention in fundamental physics for a verification of predicted thermodynamical processes [24] and for a prospective investigation of quantum properties of macroscopic objects [17, 25]. Since it is a very sensitive tool to any change in its environment, levitated particles are used also in applied physics for an ultrasensitive detection of tiny forces such as gravitational force, electric force or forces near a surface with a precision up to an order of zN [19].

In order to fully exploit a levitated particle for the purposes described above, it is necessary to precisely characterize parameters of a levitated optomechanical system. A particle levitated in air at lower pressure acts as a damped nanomechanical oscillator. Therefore, its parameters are often obtained via the power spectral density (PSD) of particle trajectories during its motion in an optical trap [12, 14, 27, 28]. The analysis of the position PSD assumes a harmonic oscillator, which applies only for a particle near its equilibrium position at the center of the optical potential. In

case of larger displacements, a potential nonlinearity has to be taken into account and the potential profile cannot be considered as harmonic anymore [21].

Therefore, we developed a novel methodology to estimate parameters characterizing a weakly nonlinear oscillator represented by a levitated particle. The method is based on averaging of recorded trajectories with defined initial positions in the phase space consisting of particle position and momentum. This technique provides us with the information about oscillator parameters such as eigenfrequency, damping, coefficient of nonlinearity and effective temperature directly from the recorded particle motion while other setup modifications such as an external driving force is not desirable.

In this Chapter, the experimental setup for a particle levitation is described and applications of such a levitated nanoparticle are overviewed. Then the PSD method is briefly introduced and our innovative approach for the parameter description is explained in detail, too. The proposed method is applied on experimental data and its validity for one–dimensional and three–dimensional motion of a levitated nanoparticle is verified by numerical simulations. We show that the new method is applicable even at lower pressures where the nonlinearity starts to play a significant role and the PSD method fails in the estimation of parameters of the optically trapped particle, especially in the damping coefficient.

This Chapter is based on our published results [18]. The author of the treatise was mainly involved in the experimental work, all the presented experimental data in this Chapter has been measured by the author. The supporting electronics was developed and tested by Ing. Petr Jedlička, Ph.D. and Ing. František Hrubý together with the author. The automatic control of the experiment done in a LabView environment was developed by Ing. Petr Jákl, Ph.D. The experimental data processing was done in Matlab environment and the code for the data analysis was mainly developed by Mgr. Martin Šiler, Ph.D.

3.1 Experimental setup

The key part of an optical setup utilized for experiments on particles levitated in vacuum environment is a strongly focused laser beam placed in a vacuum chamber where the air pressure can be tuned. Another crucial segment of the system is a branch for a particle loading and a path for a detection of particle motion in the optical trap. In this Section, the detailed technical description of the experimental setup is given followed by the explanation of the process of particle loading. Then techniques for the detection of particle positions are overviewed with focus on the quadrant–photodetector method.

3.1.1 Overview of the optical setup

A design of our experimental setup is schematically shown in Fig. 3.1. For optical trapping we utilized a low–noise linearly polarized laser beam (wavelength 1064 nm, Mephisto 2000NE) that was spatially filtered using a polarization–maintaining fibre (PMF) in order to obtain a laser beam with a high–quality Gaussian intensity profile. Then the laser beam was 3× expanded using lenses L1 and L2 (Thorlabs AC127-025-C, AC254-075-C) to slightly overfill the back aperture of the trapping lens L3. An optical power in the trapping–beam focus was controlled by a rotating half–wave plate $\lambda/2$ (Thorlabs WPH10M-1064) placed in front of a polarizing beamsplitter PBS (Thorlabs PBS253). The beam was focused by an aspheric lens L3 (Lightpath 355330, NA=0.77) placed inside a vacuum chamber. The beam power at the focal plane was set to approximately 100 mW during experiments presented in this work. The air pressure in the vacuum chamber was measured by a Pirani and cold–cathode gauge Pfeiffer Vacuum PKR 251 with its 30% accuracy and 5% reproducibility.

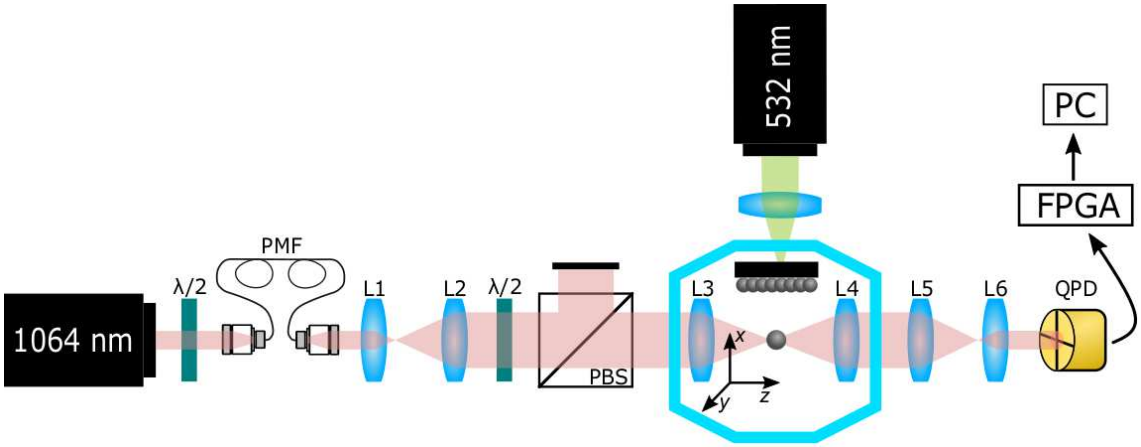

Fig. 3.1: Schematic illustration of the experimental setup. The infrared laser beam is spatially filtered using a polarization–maintaining fibre PMF, 3× expanded via lenses L1 and L2 and focused by an aspheric lens L3 in a vacuum chamber. The optical power in the laser beam is tuned by a half–wave plate $\lambda/2$ placed in front of a polarizing beamsplitter PBS. Particles are catapulted from a silicon substrate using a focused pulse green laser beam. The particle position is obtained via the same beam as used for optical trapping that is detected on a quadrant photodetector QPD together with the field scattered by the trapped particle. The detected signal is recorded through an FPGA card. Adapted from [18].

Silica nanoparticles (170 nm in diameter, Bangs Laboratories, Inc.) were launched from a substrate towards the trapping–beam focus by a focused laser pulse (wavelength 532 nm, Continuum Minilite MLII). The light scattered by a trapped

particle in the forward direction together with the unscattered part of the beam was collimated by an aspheric collector lens L4 (Thorlabs C240-TME), demagnified by a telescope L5 and L6 (Thorlabs AC254-250-C, AC254-030-C) and the resulting beam was detected by a quadrant photodetector QPD (Hamamatsu G6849). The QPD signal was processed by a home–made electronics and the particle positions in all three axes were acquired by National Instruments FPGA card (NI FPGA NI-5783 adapter module, FlexRIO FPGA) at the sampling frequency 1.78 MHz. Both loading and detection paths, are described in the following Sections in more detail.

3.1.2 Particle loading

There are two conventional methods how to load particles into an optical trap in air, by piezoelectric transducer or nebuliser. In the commonly used piezo approach [111–113], particles are sticked to a substrate due to their adhesion caused mainly by the van der Waals forces. To overcome the natural adherence, the substrate with particles is accelerated by a driven piezoelectric transducer and the particles are released from the substrate towards the optical trap. However, a minimum acceleration a_{piezo} for a particle detachment scales with a particle radius a as $a_{\text{piezo}} \sim a^{-2}$ [114] and for nanoparticles, a piezo stage cannot provide a desired acceleration. Therefore, this approach is mainly used in experiments on microparticles.

The second widely used procedure of the particle loading is a nebulising of particles diluted in an alcohol solution [12, 14, 103, 115]. Droplets are sprayed into a vacuum chamber and the alcohol evaporates quickly leaving only particles heading towards a laser focus. In this method, a dilution of the solution is critical since just one particle should be dispersed in a single droplet otherwise particles stick to each other. A weakness of this procedure is in the loading of particles at the atmospheric pressure which makes it difficult to efficiently achieve a high vacuum in a vacuum chamber. It can be solved by a loading chamber that is connected to the experimental one where subsequently, the trapped particle is transported to. Separating the experimental chamber from the loading area protects the chamber and optics against a contamination by residual particles from the loading process [116, 117].

Another innovative approach of the particle loading is a launching of particles from a substrate by a laser pulse [118–120]. A backside of the substrate is locally illuminated by a focused pulsed laser beam and the shock wave causes a desorption of particles towards a focal point. The pulse–laser–assisted launching is highly convenient in high–vacuum experiments because the catapulting of particles from a substrate can be performed at lower pressure. Thus a vacuum chamber is not contaminated by an ambient air and moreover, difficulties reaching low pressure with an optically trapped particle are overcome and the particle loss is much less pro-

bable while evacuating the vacuum chamber comparing to the pumping from the atmospheric pressure. This technique of particle launching via the laser pulse was also utilized in our experiments described in this work.

A 200μm thick silicon substrate was covered by a drop of alcohol solution with 170nm silica spheres. The wafer was heated to 80 °C and once the alcohol evaporated, another drop of the solution was added. This process was repeated until the sufficiently dense layer of particles was formed. Then the prepared substrate covered by the particles was placed in the vacuum chamber approximately 5 mm above the trapping–beam focus where its backside could be illuminated by the catapulting laser pulse. The critical point of the launching method is a speed of the launched particles. A maximum speed enabling a successful capture of the catapulted object in the optical trap is dependent on the medium damping Γ that can slow down the particle efficiently $v_{\max} \sim \lambda\Gamma$, where λ is the trapping beam wavelength [115]. Under our experimental conditions, the particle loading was achieved via a 532nm pulse laser with an energy of 4 mJ in a single pulse under a chamber pressure of 7 mBar.

However, all the loading methods mentioned above are inherently random and cannot be fully controllable. Multiple particles are often captured in the optical trap during the loading process, thus one needs to repeat the loading process several times to successfully trap a single particle. In our levitation experiments, a number of trapped particles was determined empirically from a scattering intensity of a trapped object and a profile of the power spectral density.

3.1.3 Position detection

When a nanoparticle is successfully loaded in an optical trap, one has to be able to track the particle position. Two detection techniques have been widely adopted: detection on a camera chip and photodiodes. In order to obtain 3D position by a camera imaging, the holographic video microscopy has to be utilized (see Section 2.4.2 above). Since the nanoparticle scattering is rather weak, the recorded holograms has a poor intensity modulation. Another disadvantage of this method is in its limitation of a frame rate and inability to track a particle motion in the real time. Therefore, in such experimental systems, the interferometric detection on photodiodes is predominantly implemented and the desired data can be acquired continuously.

The photodiode technique is based on the interference of the light scattered off a trapped particle with a reference beam. This interferometric measurement of position is a highly sensitive method especially for nanoparticles [121]. The procedure for levitated particles was pioneered by Gieseler et al. [12] and has enabled about 1 pm/$\mathrm{Hz}^{1/2}$ position sensitivity. There exist several arrangements of such an experimental system, forward or backward detections and detections on a quadrant

photodetector (QPD) [122, 123] or balanced detectors [12, 124].

The limiting factors of all approaches are the collection efficiency of the scattered light and detector noise [125]. The scattered light can be collected using a lens and imaged onto a photodetector [12, 104] but it is not always sufficient [124]. The collection efficiency can be improved by placing a multi–mode optical fiber close to the trapping region [118, 126] or by using optical cavities [103, 127–130]. The detection efficiency can be also enhanced by a backscattered detection alignment but the limiting factor is the imperfect overlap of a reference field with a field scattered by a trapped particle [131]. The detector noise can be rather suppressed by utilizing a balanced detector where the system noise can be subtracted immediately after its detection [121].

When using any interferometric photodiode method, the collected signal contains information about all degrees of freedom that can be analysed separately in frequency space [14, 19, 113]. In the following Section, the basic theoretical description of the detected signal is introduced and then our experimental parameters are described in more detail.

Theoretical description of a detected signal

Since the enhanced detection efficiency was not necessary in our experiments, we utilized the forward detection and as a reference beam was used an unscattered part of the trapping beam. This unscattered transmitted light provided a stable reference field without requiring additional optical path. The interference pattern was then detected on a QPD. The optical–field propagation in such a configuration and the tracking principle is described below, following the derivation in [12].

As a trapping beam, we consider a focused Gaussian beam propagating along the z axis with the polarization along the y axis. Such a beam is characterized by the following description of its field

$$\mathbf{E}_{\mathrm{in}}\left(\mathbf{r}\right)=E_{\mathrm{in}}\frac{w_0}{w\left(z\right)}e^{-\frac{R^2}{w(z)^2}}e^{\mathrm{i}\left(k_{\mathrm{m}}z-\eta(z)+\frac{k_{\mathrm{m}}R^2}{2\rho(z)}\right)}\mathbf{n}_y, \tag{3.1}$$

where $\mathbf{r}=(x,y,z)$, E_{in} is the incident electric field at focus, w_0 is the beam waist, $w\left(z\right)=w_0\sqrt{1+z^2/z_{\mathrm{R}}^2}$ is the beam radius with the Rayleigh range z_{R}, $R^2=x^2+y^2$ is the radial position and $\mathbf{n}_y$ is the polarization vector. Then we use the wavefront radius $\rho\left(z\right)=z\left(1+z_{\mathrm{R}}^2/z^2\right)$ and the phase correction $\eta\left(z\right)=\arctan\left(z/z_{\mathrm{R}}\right)$. The induced dipole in the nanoparticle illuminated by this field radiates an electric field

$$\mathbf{E}_{\mathrm{p}}\left(\mathbf{r},\mathbf{r}_{\mathrm{p}}\right)=\bar{G}\left(\mathbf{r},\mathbf{r}_{\mathrm{p}}\right)\alpha\mathbf{E}_{\mathrm{in}}\left(\mathbf{r}_{\mathrm{p}}\right), \tag{3.2}$$

where $\bar{G}$ is the field propagator given by Eq. 2.9 with a particle located at $\mathbf{r}_{\mathrm{p}}=(x_{\mathrm{p}},y_{\mathrm{p}},z_{\mathrm{p}})$.

In the paraxial approximation, where $z \gg x, y$ and thus $z \approx r$, the far field of the dipole at distance ρ from the focus is a spherical wave

$$\mathbf{E}_{\mathrm{p}}^{\mathrm{ff}}\left(\mathbf{r}, \mathbf{r}_{\mathrm{p}}\right) = E_{\mathrm{p}}\, e^{\mathrm{i}(k_{\mathrm{m}}\rho + \phi_{\mathrm{p}})}\mathbf{n}_y, \tag{3.3}$$

where

$$E_{\mathrm{p}} = E_{\mathrm{in}}\alpha\frac{1}{4\pi\varepsilon_0\rho}\, e^{-\frac{x_{\mathrm{p}}^2+y_{\mathrm{p}}^2}{w_0^2}} \tag{3.4}$$

is the amplitude of the field and

$$\phi_{\mathrm{p}} = -\mathbf{k}_{\mathrm{m}}\cdot\mathbf{r}_{\mathrm{p}} + \left(k_{\mathrm{m}} - \frac{1}{z_{\mathrm{R}}}\right) z_{\mathrm{p}} \tag{3.5}$$

is the phase of the scattered field of a nanoparticle located at $\mathbf{r}_{\mathrm{p}}$. Such a scattered field interferes with the unscattered transmitted beam used as a reference field

$$\mathbf{E}_{\mathrm{ref}}^{\mathrm{ff}}\left(\mathbf{r}\right) = E_{\mathrm{ref}}\, e^{\mathrm{i}(k_{\mathrm{m}}\rho - \pi/2)}\mathbf{n}_y \tag{3.6}$$

with the amplitude

$$E_{\mathrm{ref}} = E_{\mathrm{in}}\frac{z_{\mathrm{R}}}{\rho}\, e^{-\frac{R^2}{w(\rho)^2}}. \tag{3.7}$$

At the detector located at a distance ρ from the focus, the intensity distribution is then written as

$$I\left(\mathbf{r}, \mathbf{r}_{\mathrm{p}}\right) \propto \left|\mathbf{E}_{\mathrm{total}}\right|^2 = \left|\mathbf{E}_{\mathrm{ref}}^{\mathrm{ff}} + \mathbf{E}_{\mathrm{p}}^{\mathrm{ff}}\right|^2 = E_{\mathrm{ref}}^2 + 2E_{\mathrm{ref}}E_{\mathrm{p}}\sin\left(\phi_{\mathrm{p}}\left(\mathbf{r}, \mathbf{r}_{\mathrm{p}}\right)\right) + E_{\mathrm{p}}^2. \tag{3.8}$$

The last term in Eq. 3.8 is in case of a nanoparticle very small comparing to the other terms and can be neglected. The detected intensity then yields in

$$I\left(\mathbf{r}, \mathbf{r}_{\mathrm{p}}\right) \propto E_{\mathrm{ref}}^2 + 2E_{\mathrm{ref}}E_{\mathrm{p}}\sin\left(\phi_{\mathrm{p}}\left(\mathbf{r}, \mathbf{r}_{\mathrm{p}}\right)\right). \tag{3.9}$$

In the intensity distribution, the information about the particle position is included and the particle tracking can be performed using a photodetector.

For small particle oscillations, this technique produces directly a signal for the motion in all directions. Integrating Eq. 3.9 over the detector area, the detected signal is proportional only to the z_{p} position and the dependency on the lateral position $(x_{\mathrm{p}}, y_{\mathrm{p}})$ is cancelled. For small particle displacements in the z axis, the sine term in Eq. 3.9 can be linearized and the detected signal over the whole detector area is approximately

$$S_z \propto E_{\mathrm{p}}E_{\mathrm{ref}}\frac{z_{\mathrm{p}}}{z_{\mathrm{R}}} + C_{\mathrm{ref}}, \tag{3.10}$$

where C_{ref} is the constant value caused by the intensity of the reference field itself.

For the detection of the displacements in the x and y axes, the detected beam is split horizontally and vertically, respectively. These two parts of the splitted beam

are detected separately and the signals are mutually subtracted. This mechanism removes the constant term in Eq. 3.9 and thus the dependency of the signal on the z_p position. Then we can use the same approximation for small displacements as in the z axis and the detected signal for the x axis is

$$S_x \propto E_\mathrm{p} E_\mathrm{ref} \frac{x_\mathrm{p}}{w_0}. \tag{3.11}$$

The y_p position is measured analogously.

Detection parameters and outputs

The resulting intensity from the interfering fields described above is detected on a QPD Hamamatsu G6849. The optical power in the 1mm wide y–polarized beam was approximately 2 mW. The detected signal on each quadrant was converted into the voltage using operational amplifier ADA4004-4 placed very close to the photodiodes. The obtained voltage was further processed by home–made electronics. The signals from the individual quadrants were summed up and subtracted using operational amplifiers OPA134 in order to obtain the position of a trapped particle in all three coordinate axes, as described above and illustrated in Fig. 3.2. The signals representing x and y motion were amplified 100× and the z signal was amplified 30× using operational amplifiers AD797. The AC coupled signals were then acquired by the National Instruments FPGA card at the sampling frequency 1.78 MHz. The home–made electronics also provided us with the DC component of the output signals used for the QPD alignment.

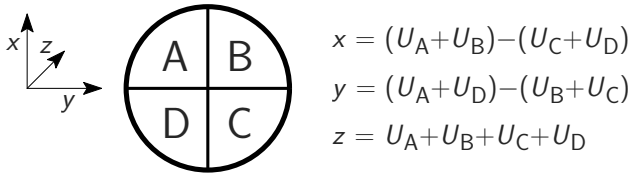

Fig. 3.2: Scheme of a quadrant photodetector with quadrants A–D and the calculation of a particle motion in all coordinate axes through the summation and subtraction of the quadrant voltage signals.

The particle trajectories in all three coordinate axes recorded at ambient pressure of 1 mBar are plotted in Fig. 3.3a. The oscillatory motion is evident in all three directions which is even more pronounced in the power–spectral–density analysis shown in Fig. 3.3b. Note that for a tightly focused laser beam with a linear polarization used for optical trapping, the field distribution is slightly elongated along the direction of polarization of the incident field, which leads to slightly different trapping frequencies along the two transverse directions [132]. The oscillation frequency

in the optical z axis is different from the transversal motion because of the focused–beam profile. Therefore, the motion in all three axes can be easily distinguishable in the frequency space. Except the main oscillation peak, several other peaks can be observed. This can be partially caused by a misalignment of the QPD but mainly by the cross–talks between different coordinate axes due to the potential nonlinearity [121], as discussed later.

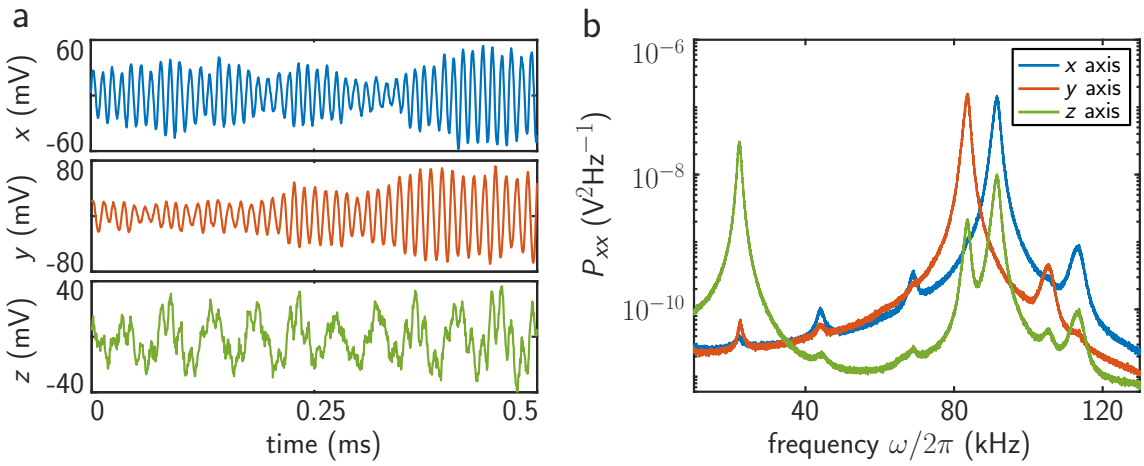

Fig. 3.3: (a) Recorded trajectories of a levitated nanoparticle in all three directions at the ambient pressure of 1 mBar. (b) Power spectral density obtained from 33s long trajectories, whose short regions are plotted in (a).

3.2 Applications of a levitated nanoparticle

Levitated nanoparticles have gained a great attention in both fundamental and applied physics. In contrast to microfabricated devices, optically levitated nanoparticles do not suffer from clamping losses and neither microfabrication of an oscillator device nor substrate is needed. Dissipation comes mainly from a noise in an optical field and interactions with a surrounding gas, which can be minimized by operating an optical tweezers in vacuum. Such an oscillator has very promising properties. An oscillation frequency of a levitated particle is high ($f \simeq 100\,\mathrm{kHz}$) and the damping in ultrahigh vacuum is very low (at pressure $p = 10^{-9}\,\mathrm{mBar}$ for 170nm nanoparticle $\Gamma/2\pi \simeq 10^{-6}\,\mathrm{Hz}$). Thus the quality factor of the system characterizing an oscillator bandwidth and energy losses can reach a very high value $Q = \frac{2\pi f}{\Gamma} \simeq 10^{-11}\,\mathrm{Hz}$ [12] which is orders of magnitude higher than quality factors of clamped oscillators [133, 134].

A key advantage of optically levitated oscillators is the ability to easily control system parameters. The damping factor can be tuned by the ambient pressure in a

vacuum chamber and the mechanical frequency can be dynamically modulated by a laser–beam power. Moreover, an optical potential explored by a trapped particle can be shaped into almost arbitrary force fields [135]. Thus an optically levitated particle is an excellent test bed for a wide range of nanothermodynamic phenomena in the underdamped regime that can be directly experimentally verified [23, 24]. For example, the levitation system allows to study the Brownian motion of a single well–isolated particle with high temporal and spatial resolution and controllable coupling to the environment. Thus the ballistic regime of Brownian motion could be observed, in contrast to the usual diffusive regime [27, 136]. Levitated nanoparticles have also led to the first quantitative measurement of Kramers turnover [135] and to a demonstration of general fluctuation theorems in the underdamped regime [137, 138] and the differential fluctuation theorem in both, overdamped and underdamped regimes [138].

Another exciting applications could be found with a levitated nanoparticle rotated by means of the beam polarization or orbital angular momentum [111, 120, 139–141]. Particles with a certain anisotropy originating from the intrinsic birefringence [111, 142, 143] or from the anisotropic shape [118, 126, 144] can be set into rotation at MHz [111, 126, 145–147] up to GHz [141] frequencies. Such a gyroscope could be used to design microscopic engines in the classical and quantum regime [148]. Several other engines have been already realized utilizing an optically levitated nanoparticle, such as Stirling [149] and Carnot [150] heat engines.

Nevertheless, a major motivation for performing optomechanical experiments with levitated particles is its potential to study fundamental quantum physics on macroscopic objects [25, 26]. Thanks to easily controllable parameters of a levitated oscillator, the motion of the center of particle mass in the optical trap can be cooled down and achieve very low energy states up to its quantum ground state even in the environment at room temperature [17]. Already in 1977 A. Ashkin showed that dielectric particles can be levitated and cooled under vacuum conditions [151].

There are two main routes for cooling, active feedback [12, 116, 124, 125, 152, 153] and passive cavity cooling [17, 103–106, 130, 154–156]. In active–feedback experiments, the particle position is monitored and correspondingly, the particle motion is cooled down by modulating the system properties via the active parametric feedback loop. At first, the cooling was performed employing the optical scattering force of laser beams illuminating the trapped particle from all 6 directions [157]. To simplify the experimental arrangement, Gieseler et al. proposed and experimentally verified the levitated optomechanical system for center–of–mass cooling by modulating a laser–beam power (i.e. the trap stiffness) and they managed to cool the particle motion in all three spatial degrees of freedom by a single trapping laser beam [12, 21, 116].

Even the active feedback loop has been improved applying Kalman filter to estimate the particle position or other machine–learning algorithms [158], the quantum ground state has not been achieved via the active–feedback approach. The limiting factor is mainly the photon recoil heating and a poor efficiency of the position detection [124]. To overcome the shot noise, the cold damping has been implemented using a charged particle in a modulated electric field [125, 152, 153]. Another investigation direction completely leaves the optical trapping and particles are levitated exploiting electric Paul traps [159] or purely magnetic traps [160, 161].

At the end, a tremendous progress towards entering the quantum regime was realized by the passive cooling enabling the automatic feedback [155, 156]. The quantum ground state of the center–of–mass motion was achieved for a particle optically trapped by an independent laser beam inside an empty optical cavity whose resonant frequency was tuned slightly higher than the optical frequency of the trapping laser [17].

The cooled particle motion also opens up a wide range of exciting new experiments in the classical domain of applied physics. Oscillators of low mass ($m \simeq 10^{-18}\,\mathrm{kg}$) and high quality factor are particularly useful for force sensing in a room–temperature environment [19, 113]. Since the cavity–cooling method presents more technical limitations and less flexibility, in the force–sensing experiments the optical–tweezers approach is generally utilized. Such an ultrasensitive detector can precisely detect very tiny forces in orders of zN [19, 20] and thus the levitated optomechanical system could be utilized for a detection of Casimir forces or van der Waals interactions [21, 140]. For now, the static gravitation and electric forces have been detected with free–falling nanoparticles with sensitivity of 10 aN [22] and surface–induced forces together with the potential mapping have been examined [162, 163].

3.3 Theoretical description of nanoparticle motion

While exploiting a levitated nanoparticle for the purposes mentioned above, an evaluation of oscillator parameters characterizing the system properties is crucial. This Section is dedicated to a theoretical description of a motion of a optically levitated nanoparticle and a characterization of crucial parameters of the levitated optomechanical system is introduced for linear and nonlinear regimes.

A nanoparticle optically levitated in air with reduced pressure is less disturbed by surrounding air molecules comparing to aqueous or other viscous media. Therefore, a motion of such a levitated particle near its equilibrium position tends to

be considered as a slightly damped nanomechanical oscillator, which motion is described by the Langevin equation of motion. For one coordinate x, the Langevin equation applies [164, p. 194]

$$\ddot{x}\left(t\right)+\Gamma\dot{x}\left(t\right)+\frac{\mathrm{d}}{\mathrm{d}x}\frac{U\left(x\right)}{m}=\frac{F_{\mathrm{fluct}}\left(t,\Gamma,T\right)}{m}, \tag{3.12}$$

where t is time, Γ is the medium damping, $U\left(x\right)$ is the optical potential given by the focused laser beam, m is the particle mass, T is the effective temperature and $F_{\mathrm{fluct}}\left(t,\Gamma,T\right)$ is the fluctuating Langevin force [24] uncorrelated in time with zero mean and its variance is given by the fluctuation–dissipation theorem $\langle F_{\mathrm{fluct}}(t)\rangle=0$, $\langle F_{\mathrm{fluct}}(t)F_{\mathrm{fluct}}(t')\rangle=2m\Gamma k_{\mathrm{B}}T\delta(t-t')$, where $\langle ...\rangle$ denotes correlation of functions within brackets, k_{B} is the Boltzmann constant and $\delta(x)$ denotes the delta function of x.

In order to describe the oscillator motion, all system parameters should be evaluated. The damping coefficient Γ can be theoretically predicted via the ambient pressure determined by a pressure gauge [157]. At higher pressures, where a levitated particle is not heated by a laser beam used for optical trapping, an effective temperature T can be estimated as a temperature of an ambient air. A particle mass m is generally given by declared particle dimensions and material or it can be defined more precisely by driving a charged particle in an electric field as discussed later in this Section [165]. However, the determination of an optical potential is not so straightforward and usually, one has to come up with some approximation. In the following, we describe the widely used harmonic approximation and then we focus on nonlinearities in an optical potential approximated by the first lower–even–order terms in the Taylor–series expansion, called Duffing nonlinearity.

3.3.1 Harmonic oscillator

The scattering force acting on a small object trapped in an optical tweezers is negligible, while the gradient force is typically highly predominant. In an optical trap, the gravity affects the optically levitated particle, too. However, the deflection of the particle caused by the gravitational force is very small ($\sim 10^{-2}$ nm) comparing to the particle oscillations ($\sim 10^{2}$ nm) and thus the symmetry of the optical trap is not broken. Since the gradient force is a conservative force, it can be described by the effective optical potential. Therefore, it can be supposed that the nanoparticle oscillates in an optical potential simply defined by a profile of the trapping beam and a corresponding gradient force. The profile of the focused beam is commonly assumed as Gaussian and amplitudes of particle oscillations are small comparing to the trapping–beam waist. Then the optical potential can be simplified into its

harmonic form

$$U = \frac{1}{2}\kappa_x x^2, \tag{3.13}$$

where κ_x is the trap stiffness and x is the particle position in the x axis relative to the trap center. Consequently, the gradient force acting on the levitated particle can be considered as a linear restoring force typical for an ideal harmonic oscillator

$$\langle F_{\mathrm{grad},x} \rangle = -\kappa_x x. \tag{3.14}$$

In such a three–dimensional harmonic potential, the motional degrees of freedom are highly decoupled and the equation of motion for each degree of freedom x, y and z can be treated independently.

Power spectral density

It is not always straightforward to directly analyse equation of motion due to the stochastic term. The most widely used method for analysis of the optically levitated particle and the optical trap properties is to Fourier transform the recorded trajectories and analyse its power spectral density (PSD) [12, 14, 27, 28]. PSD is a useful tool in experiments with harmonic oscillators, since the dynamics of the oscillator can be separated from spectrally distant undesirable features. This approach has been extensively used from the first optical tweezers experiments in the overdamped regime [166] and is still widely used for analyses of optically levitated particles even in vacuum [12, 167, 168]. In the following, we focus only on the underdamped regime ($\Omega_0 >> \Gamma$, where Ω_0 is the particle eigenfrequency) relevant for the levitated–particle systems.

Assuming the harmonic potential given by Eq. 3.13 and the n–order derivative $\mathrm{d}^n x(t)/\mathrm{d}t^n = (\mathrm{i}\omega)^n x$ with the frequency ω, the Langevin equation of motion 3.12 can be solved

$$|x\left(\omega\right)|^2 = \frac{|F_{\mathrm{fluct}}|^2/m^2}{\left(\omega^2 - \Omega_0^2\right)^2 + \Gamma^2\omega^2}, \tag{3.15}$$

where $\Omega_0 = 2\pi f_0 = \sqrt{\kappa_x/m}$ denotes the particle eigenfrequency. From the known oscillator trajectory $x\left(t\right)$, the one sided power spectral density of position of an ideal stochastic harmonic oscillator is derived into the following form [12, 103, 157, 167, 169]

$$\begin{aligned} P_{xx}\left(\omega\right) &= \int_{-\infty}^{\infty} \langle x\left(t\right) x\left(t - t'\right)\rangle e^{-\mathrm{i}\omega t'} \mathrm{d}t' \\ &= \frac{2k_{\mathrm{B}}T_{\mathrm{SP}}}{m} \frac{\Gamma}{\left(\omega^2 - \Omega_0^2\right)^2 + \Gamma^2\omega^2}, \end{aligned} \tag{3.16}$$

where T_{SP} is the effective spectral temperature.

By fitting the PSD formula to the experimentally obtained PSD, we can extract parameters characterizing the ideal harmonic oscillator. A comparison of the experimentally obtained PSD and the curve fitted to the peak is depicted in Fig. 3.4a. The position of the oscillation peak reveals a value of Ω_0 while its width is given by the medium damping Γ. If the particle mass and the QPD calibration are known, the effective temperature T_{SP} from the peak height with respect to the damping can be obtained, too.

Using the equipartition theorem

$$\frac{1}{2}m\Omega_0^2\langle x^2\rangle = \frac{1}{2}k_{\mathrm{B}}T \tag{3.17}$$

and the Wiener–Khinchin theorem [170, 171, p. 59]

$$\langle x^2\rangle = \frac{1}{2\pi}\int_0^\infty P_{xx}\left(\omega\right)\mathrm{d}\omega, \tag{3.18}$$

the effective spectral temperature can be also extracted by integrating over the PSD

$$T_{\mathrm{SP}} = \frac{m\Omega_0^2}{\pi k_{\mathrm{B}}}\int_0^\infty P_{xx}\left(\omega\right)\mathrm{d}\omega, \tag{3.19}$$

knowing the values of the mass m and the eigenfrequency Ω_0 together with the QPD calibration.

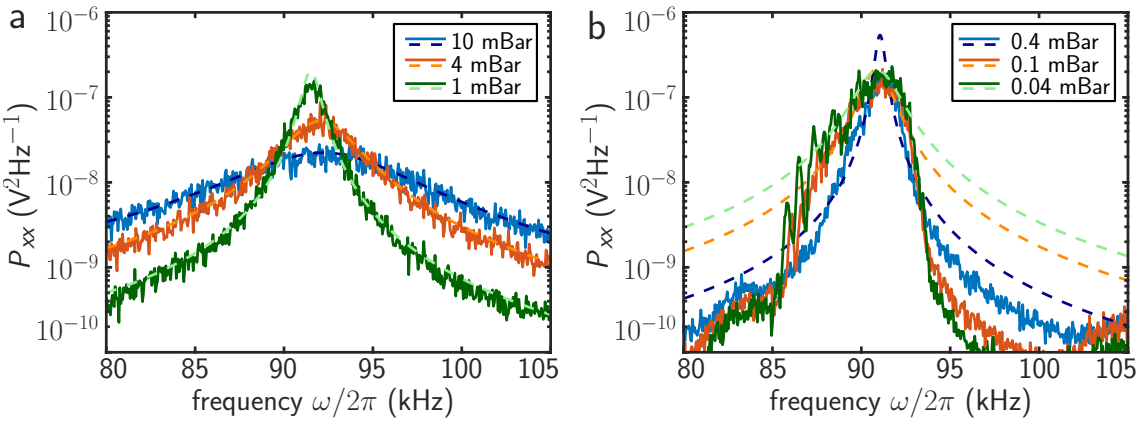

Fig. 3.4: Power spectral density (PSD) of a particle motion in the x axis for various ambient pressures. Dashed curves represent fits by Eq. 3.16. (a) At higher pressure, PSD profile can be fitted by Eq. 3.16 and the system parameters are obtained. (b) At lower pressure, the peak deforms due to the potential nonlinearity and the PSD fitting cannot be reliably performed anymore.

Mass characterization

Since the PSD method does not provide us with any information about the oscillator mass, there has been developed another approach for the mass estimation [165]. In

this method, a charged levitated particle is driven with the electric field on the frequency close to its eigenfrequency in the highly damped regime ($p \simeq 50\,\mathrm{mbar}$). Using the PSD assuming the harmonic potential, the mass of the particle is then given by the following ratio [165]

$$m = \frac{q^2 E_0^2 \tau}{8 k_\mathrm{B} T R_\mathrm{S} \Gamma}, \tag{3.20}$$

where q is the particle charge, E_0 is the amplitude of the applied external electric field, τ is the time length of the trajectory record, T is the bath temperature and R_S is the ratio of the driving–peak height to the value in PSD at the driving frequency when the external driving is off. This method estimates the mass value with the precision better than 1 %.

However, the electric–field driving has not been implemented in our experimental system and the oscillator mass was estimated simply from the declared diameter 170 nm and the silica mass density $2.0\,\mathrm{g/cm^3}$ (Bangs Laboratories, Inc.). Nevertheless, this method is not fully reliable because silica nanoparticles are highly porous and the liquid inside pores evaporates while reducing the ambient pressure [172]. The mass loss causes a slight decrease in the oscillation frequency and the scattering intensity, as shown in Fig. 3.5a. Below the pressure $p \simeq 0.05\,\mathrm{mBar}$ the properties of the trapped particle does not change anymore and its oscillation frequency and scattering intensity remain constant even while increasing the chamber pressure, see Fig. 3.5b. Therefore, in our presented experiment at first the process of pumping and venting chamber is performed while trapping the nanoparticle in order to obtain stable system properties that do not vary during experimental procedures.

Towards lower pressure

As we have demonstrated in Fig. 3.4a, the PSD peak can be reliably fitted by Eq. 3.16 assuming the harmonic oscillator down to pressure $p = 1\,\mathrm{mBar}$. However, if the ambient pressure is reduced even more, the profile of the oscillation peak in the displacement PSD is deformed and its shape is no more Lorentzian, see Fig. 3.4b. One can notice that the measured peak is wider and lower than the theoretically predicted one and a clear asymmetry of this peak appears exhibiting a visible negative skewness. Moreover, other peaks related to the higher harmonics generations as well as the cross–talks between the motion in different coordinate axes can be observed.

Since the main peak is apparently asymmetric and no more follows the theoretical prescription for the PSD, the fitting by the formula would not provide us with the relevant parameters of the levitated system [21, 135]. Such a deviation of the experimental PSD profile from the ideal one can be caused by the softening of

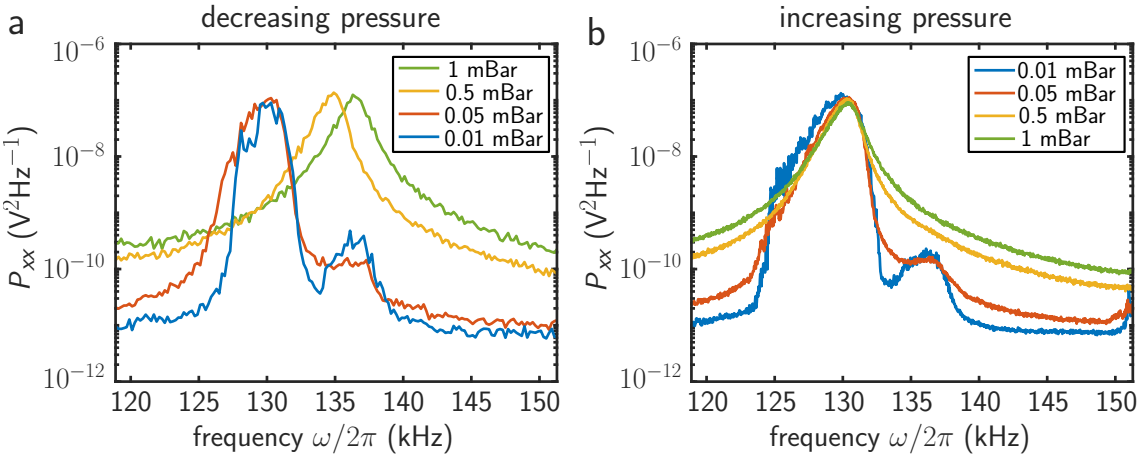

Fig. 3.5: Power spectral density (PSD) of an optically trapped silica nanoparticle. (a) When decreasing the ambient pressure, the drop in the oscillation frequency is observed, as well as a slight decrease in the scattering intensity caused by the particle–mass change. (b) After reaching the critical pressure ($p \simeq 0.05\,\mathrm{mBar}$), the particle properties remain constant at any pressure.

the experimental potential profile from the assumed ideal harmonic trap [21, 173]. This nonlinearity in the system causes a PSD–peak broadening at lower pressure where the PSD–peak width due to the damping is significantly reduced. In the following Section, a nonlinear oscillator is described in more detail and methods for the parameters determination are overviewed.

3.3.2 Nonlinear oscillator

In Fig. 3.4b we have demonstrated the deformation of the oscillation peak whose shape is no more Lorentzian, as predicted by Eq. 3.16 for an ideal harmonic oscillator. The PSD analysis assumes that the motion of the trapped particle is linear which applies only for very small deviations from the equilibrium position. However, Brownian motion can cause the trapped nanoparticle to explore nonlinear regions of the trapping potential, as observed in [21]. For larger oscillation amplitudes, the motion becomes anharmonic and the approximation of the optical potential has to be improved. Assuming just the first lower–even–order terms in Taylor series expansion of the real profile of the potential near its minimum, it gives the Duffing–type nonlinearity [21, 174]. The nonlinearity of the optical potential U is characterized by the coefficient of the Duffing nonlinearity ξ_x and the optical potential is described as follows [21]

$$U = \frac{1}{2}\kappa_x x^2 \left(1 - \frac{1}{2}\xi_x x^2\right). \tag{3.21}$$

In the real optical traps the coefficient ξ_x is positive and thus the stiffness of the optical spring gets weaker with an increasing deviation from the equilibrium position. Such an oscillator is called softening Duffing oscillator [21, 174–176].

Based on experimental investigations, new diverse effects have been recently observed in underdamped Duffing oscillators based on various nonlinear systems such as nano–electromechanical systems [177–179], micro–electromechanical systems [180–184], nonlinear electric oscillators [185], solid–state systems [186], mechanical oscillators with a chemical bond [187] and upcoming quantum mechanical oscillators with superconducting qubits [188]. In order to fully exploit the Duffing oscillator, it is desirable to characterize all the parameters of the nonlinear system including the Duffing coefficient of nonlinearity. In the following, the basic behaviour of the softening Duffing oscillator is theoretically described and existing methods for the parameter extraction are introduced.

Equation of motion

Assuming the approximation of the softening Duffing oscillator given by Eq. 3.21, the Langevin equation of motion 3.12 for one coordinate x is modified into the following form [21, 174]

$$\ddot{x}\left(t\right)+\Gamma\dot{x}\left(t\right)+\Omega_0^2 x\left(1-\xi_x x^2\right)=\frac{F_{\text{fluct}}\left(t,\Gamma,T\right)}{m}. \tag{3.22}$$

For the underdamped oscillator when $\Omega_0 \gg \Gamma$, the stochastic force F_{fluct} is much smaller than the deterministic terms in Eq. 3.22. Under these conditions, the frequency shift of the nonlinear oscillator can be derived. Employing the perturbation theory and the assumption that the amplitude of oscillations x_0 varies slowly in time comparing to the eigenfrequency Ω_0, the nonlinear frequency shift is given by [21]

$$\Delta\Omega=\Omega_{\text{H}}-\Omega_0=-\Omega_0\frac{3}{8}\xi_x x_0^2, \tag{3.23}$$

where Ω_{H} is the eigenfrequency of the damped harmonic oscillator depending on its amplitude x_0. Thus Ω_0 in the Duffing system corresponds to the eigenfrequency of the oscillation with zero amplitude while for larger amplitudes the eigenfrequency decreases.

Because of the Duffing nonlinearity, the oscillation frequency becomes a function of the oscillation amplitude. At higher pressure, the frequency shift induced by the Duffing nonlinearity can be neglected since it is much smaller than the linewidth caused by the medium damping Γ. However, at lower pressures the amplitude fluctuations lead to significant frequency shifts and the PSD peak is distorted. The phenomenon of the frequency dependence on the oscillator amplitude is demonstrated on the experimental data in Fig. 3.6 recorded at 0.04 mBar. The PSD oscillation

peak obtained from a long data set shown in Fig. 3.6b is broadened and asymmetric, see the black curve in Fig. 3.6a. If we analyse a shorter time interval when the particle oscillates with smaller amplitudes ($x < \sigma_x$, where σ_x is the standard deviation calculated from the long data set), the oscillation peak is much narrower and symmetric and is located at higher oscillation frequencies, see the blue curve. On the other hand, when the particle oscillates with a much higher amplitude (indicated by the red curve in Figs. 3.6a and 3.6c), the nonlinearity starts to play an important role. The oscillation peak is wider and down–shifted, as predicted by Eq. 3.23. Also the minor peaks caused by the cross–talks between different coordinate axes [121] are more pronounced in the motion with larger amplitudes.

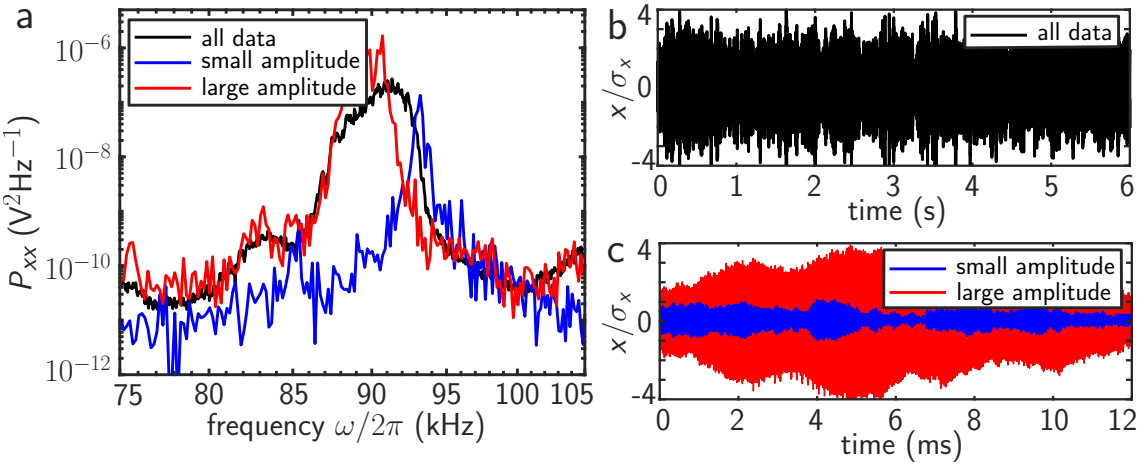

Fig. 3.6: (a) PSD of an optically trapped silica nanoparticle recorded at the ambient pressure of 0.04 mBar. Black curve represents a long data set shown in (b) while the blue and red curves illustrate PSD of shorter time intervals of the particle motion with smaller and larger amplitudes shown in (c), respectively. x position in (b) and (c) is normalized to its standard deviation σ_x calculated from the long data set.

Determination of oscillator parameters

Since the resonant PSD peak of the nonlinear oscillator is asymmetric, the commonly used method exploiting PSD fitting is not applicable and other methods have to be employed in order to obtain system parameters. Nevertheless, it is still possible to extract the spectral temperature by analysing the PSD, if the calibration of the detection system and the particle mass are known. For the harmonic oscillator, the equipartition theorem utilizing the potential energy is applied, but for an anharmonic oscillator, the formula given by Eq. 3.17 does not generally hold. However, the effective temperature of a nonlinear oscillator can be obtained using the kinetic energy, for which the equipartition theorem still holds even for the nonlinear

oscillator in the form [170]

$$\frac{1}{2}m\langle\dot{x}^2\rangle = \frac{1}{2}k_{\mathrm{B}}T. \tag{3.24}$$

The variance $\langle\dot{x}^2\rangle$ can be calculated by a numerical integration of the power spectral density of the particle velocity P_{vv} applying the Wiener–Khinchin theorem and the effective temperature can be obtained in analogy to Eq. 3.19

$$T_{\mathrm{SP}} = \frac{m}{\pi k_{\mathrm{B}}}\int_0^\infty P_{vv}\left(\omega\right)\mathrm{d}\omega. \tag{3.25}$$

The velocity PSD P_{vv} can be derived from the displacement PSD P_{xx} even for the anharmonic potential as [170]

$$P_{vv}\left(\omega\right) = \omega^2 P_{xx}\left(\omega\right). \tag{3.26}$$

Another essential parameter of the Duffing oscillator is the coefficient of Duffing nonlinearity, which can be obtained by one of known techniques. The first method is based on the driving of the levitated nanoparticle by modulation of the trapping–beam power [21]. The modulation frequency is swept over a parametric resonance and an experimental determination of a threshold frequency and a maximum potential energy provides us with an estimation of the coefficient of Duffing nonlinearity. The second approach is based on a rapid reduction of the trapping power while a levitated particle can explore the nonlinear potential region during the relaxation into its original thermal state [189]. A phase–space distribution of a spiral shape is then compared with simulated phase–space points using a Kolmogorov-Smirnov statistical test and the coefficient of Duffing nonlinearity is obtained. However, all these methods require a modification of the experimental procedure which can affect the original examined levitated system. Therefore, in this work, a novel methodology is proposed to determine all desired parameters of an optically levitated particle in a Duffing–type potential. The new method exploits only the recorded trajectories of the levitated particle and no modification of the experimental system is needed. In the following Sections, the data processing together with the developed methodology is described in more detail.

3.4 Signal calibration

In order to process the recorded trajectories, the calibration of the QPD detection system is desired. The standard method is to analyse the displacement PSD and use the equipartition theorem together with the known ambient temperature [12, 14, 21]. This method assumes that the particle is in the thermal equilibrium with its environment and the motion of the particle is purely harmonic [14, 21, 28]. It

is also possible to use another calibrated force to calibrate a detector, for example an electric force acting on a charged particle [20, 170]. But this method requires a precise knowledge of an applied force and a modification of an experimental setup.

To avoid a miss–calibration due to the mentioned nonlinearities in the optical potential, we use the velocity PSD and the equipartition theorem exploiting the kinetic energy of the particle motion, see Eq. 3.24 [170]. The calibration constant is then calculated as

$$C_{\mathrm{V}\to\mathrm{m}} = \sqrt{\frac{\pi k_{\mathrm{B}} T}{m \int_0^\infty P_{vv}(\omega)\,\mathrm{d}\omega}}, \tag{3.27}$$

where $T = 295\,\mathrm{K}$ is the room temperature, $m = 5.14\,\mathrm{fg}$ is the particle mass calculated from the declared dimension and mass density and P_{vv} is the velocity PSD in $\mathrm{V^2Hz}$.

Since the velocity PSD is obtained through the displacement PSD via Eq. 3.26, the noise increases with the frequency. Therefore, it is crucial to suppress high frequency noise in the displacement PSD that could be much more enhanced in the velocity PSD. In our case, a noise suppression was performed by subtracting the average level of the white noise at high frequencies P_{xx}^{∞} in P_{xx}

$$P_{vv}(\omega) = \omega^2 \left(P_{xx}(\omega) - P_{xx}^{\infty}\right). \tag{3.28}$$

To determine the noise level P_{xx}^{∞} we analyzed P_{xx} at frequencies $\omega/2\pi > 0.66 f_{\mathrm{Nyq}}$, where f_{Nyq} is the Nyquist frequency calculated as $f_{\mathrm{Nyq}} = f_{\mathrm{sample}}/2$ with the sampling frequency $f_{\mathrm{sample}} = 1.78\,\mathrm{MHz}$. In this higher–frequency range, the displacement PSD was firstly smoothed by a moving average filter and then the result was fitted by

$$P_{xx}(f) = Af^{-B} + C, \tag{3.29}$$

where A, B, and C are fitting parameters. An example of such a procedure of the background determination is shown in Fig. 3.7. The noise level was then set to $P_{xx}^{\infty} = C$.

The velocity PSD used for the calculation of the calibration constant is shown in Fig. 3.8 in the first row for two different ambient pressures. The blue curves illustrate the velocity PSD from the original raw data and the red curves show the velocity PSD of the data with the background subtracted in the displacement PSD, as described above. The background subtraction is crucial mainly at higher frequencies while the main oscillation peak remains unaffected. Except the main oscillation peak, other frequency peaks related to the higher harmonics generations and the cross–talks between the motion in different coordinate axes can be observed in the PSD. However, these peaks do not play a crucial role for the determination of the calibration constant from the integration of the velocity PSD. This is illustrated by the cumulative sum of the velocity PSD in Fig. 3.8 in the second row. A significant contribution to the sum is formed predominantly by the main oscillation peak while

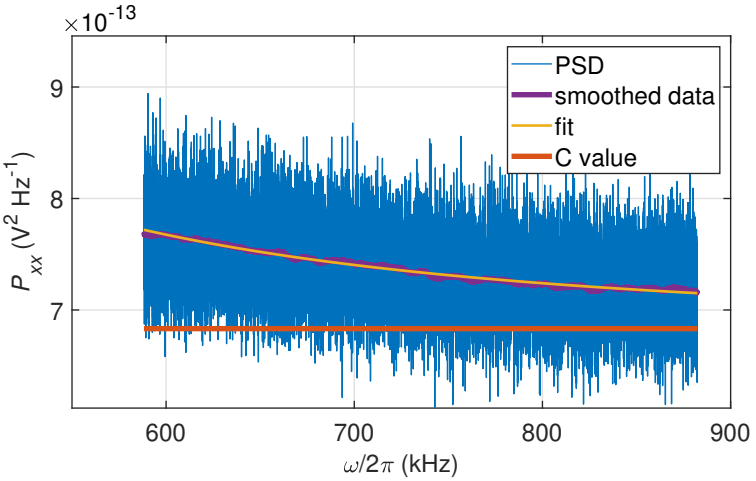

Fig. 3.7: High frequency tail of displacement PSD used for the estimation of the background. Smoothed P_{xx} (violet curve) was fitted (yellow curve) by Eq. 3.29 and the background was determined as the asymptote (red line) of the fitted function. The particle motion was recorded at the ambient pressure of 0.1 mBar.

contributions of other peaks are negligible. Only at lower pressure the small increase in the cumulative sum caused by the side peak is detected, but this contribution is still in the order of percent.

In the data processing, we focused only on the transversal axes, x and y, because the potential shape along the optical z axis is not Gaussian and cannot be simply approximated by the potential of the Duffing type. The calibration constant in both, x and y axes calculated via the integration of the velocity PSD at different pressures is plotted in Fig. 3.9 (see red curves). The values of the calibration constant form a constant level plateau at higher pressures above 0.4 mBar while at lower pressures the calibration constant decreases significantly. This phenomenon can be caused by a change of the particle temperature. Even though the particle absorption is low, high temperatures can be reached because of a poor heat transfer to the surrounding gas at low pressures [14]. Thus the temperature of the particle motion is higher than the room temperature used for the calculation of the calibration constant which leads to the drop in the value of the calibration constant. Therefore, the calibration process has to be performed at higher pressures where the particle is in the thermal equilibrium with its environment. We calculated the value of the calibration constant as a mean value in the pressure range from 0.4 mBar up to 10 mBar and this value was applied to the experimental data at all studied pressures. The values of calibration constant in the x and y axes were $C_{\mathrm{V}\to\mathrm{m},x} = (1.896 \pm 0.006)\,\mu\mathrm{mV}^{-1}$ and $C_{\mathrm{V}\to\mathrm{m},y} = (2.144 \pm 0.003)\,\mu\mathrm{mV}^{-1}$, respectively.

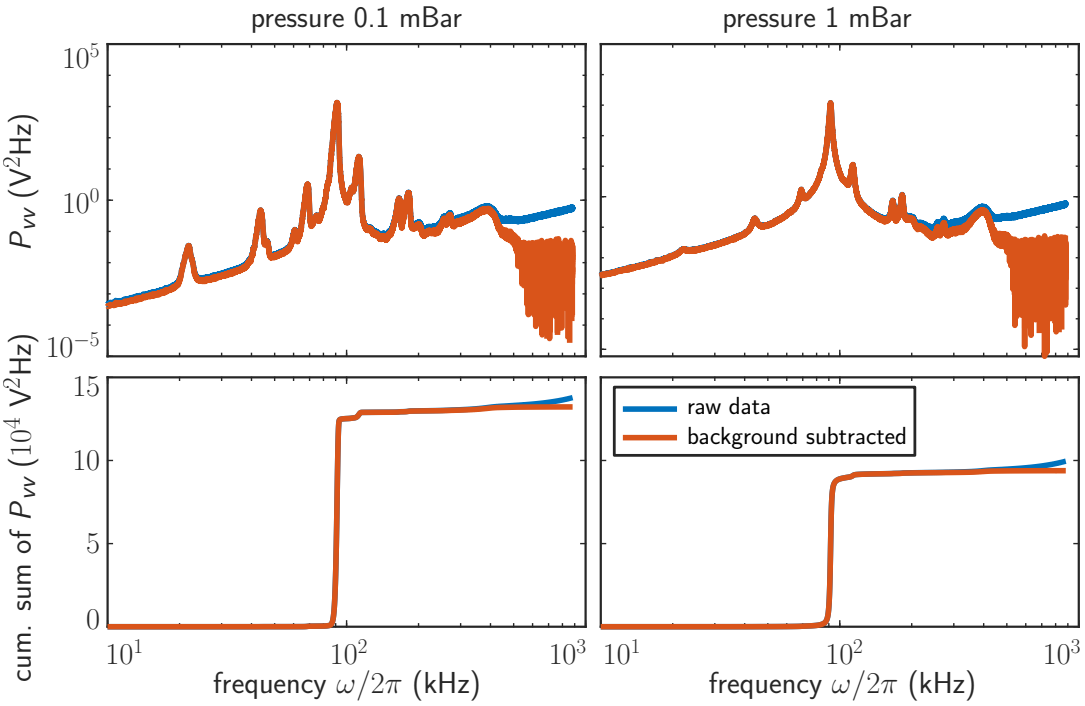

Fig. 3.8: (row 1) Velocity PSD in the x axis at two different ambient pressures. Blue curves illustrate the original raw data while the red curves shown the data with the background subtracted in the displacement PSD. (row 2) Cumulative sums of the corresponding velocity PSD shown in row 1.

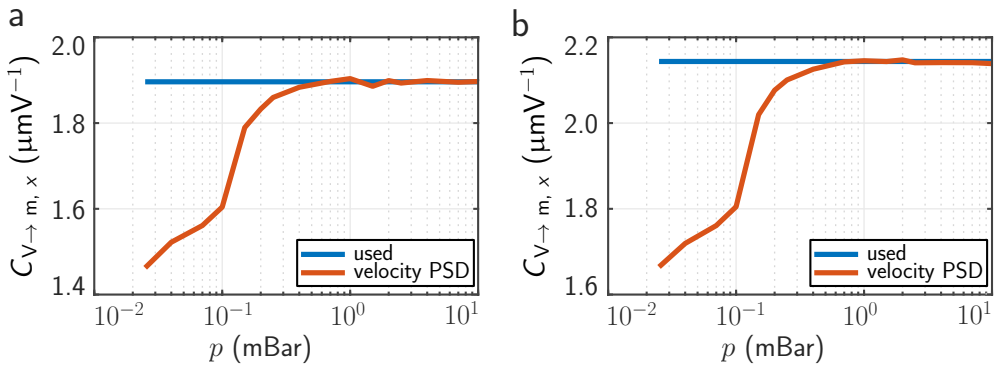

Fig. 3.9: Pressure dependence of the calibration constant $C_{\mathrm{V}\to\mathrm{m}}$ calculated from the velocity PSD (red) using Eq. 3.27 and a value of calibration constant that was actually used for the data processing (blue) for (a) the x axis and (b) the y axis. Taken from [18].

3.5 Data processing

As we have already presented in Fig. 3.6, the amplitude of oscillations varies in time. Here in Fig. 3.10, we show such a 1D trajectory in more detail. Two small regions of the whole trajectory shown in Fig. 3.10a were magnified and plotted in Fig. 3.10b. In the left part, the nanoparticle oscillates with a low amplitude close to the bottom of the optical potential ($x < \sigma_x$, where σ_x is the standard deviation calculated from the long data set) and in the second example of the trajectory, a higher amplitude of oscillations is demonstrated. It can be observed that the small–amplitude motion is strongly affected by noise whereas the large–amplitude oscillations are clearly visible and rather modified by the nonlinear potential profile.

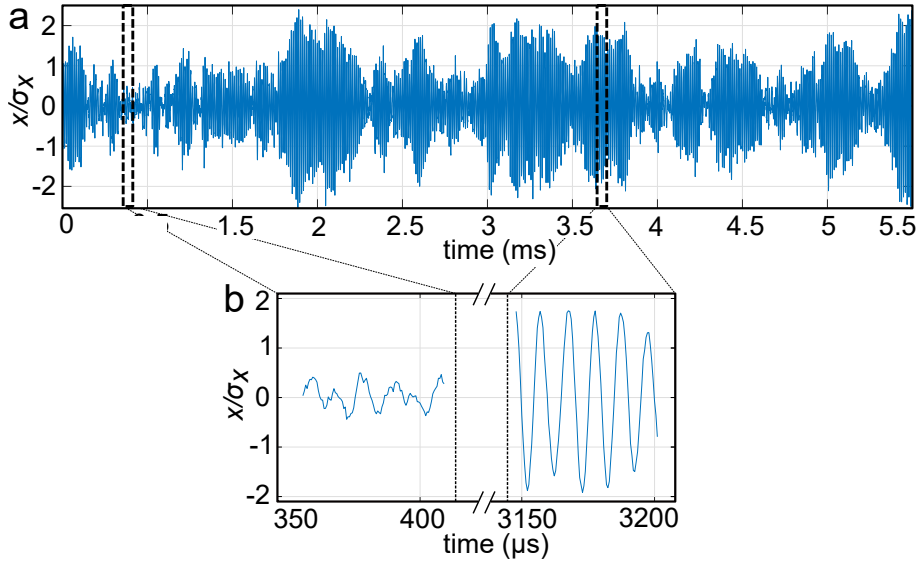

Fig. 3.10: (a) Particle trajectory in the x axis normalized to its standard deviation σ_x for the ambient pressure 1 mBar. (b) Magnified regions of the trajectory from (a) for small and large oscillations. Adapted from [18].

Our goal was to develop a methodology for an estimation of the oscillator parameters during a short transient dynamics of the levitated nanoparticle. A short time scale relatively to the heating rate is crucial for experimental testing of transient stochastic phenomena and for quantum experiments with a prepared initial state [190, 191]. The standard methodology based on the PSD of particle positions of velocities presumes that values estimated from steady states are valid also during the transient dynamics which can lead to significant systematic errors in the estimated values, as it is later shown in our results. Therefore, in this work, we propose a novel method for determination of parameters of an optically levitated nanoparticle based on the post–selection and post–processing of the measured stochastic trajectories with suitable initial conditions. Since the levitated system is stochastic and a

random noise influences the individual trajectories, each transient process with the same initial conditions leads to a different trajectory. Thus the post–selected trajectories were analysed via their moments, e.g. mean and variance in order to suppress the random noise. In the following, the data acquisition and the post–processing algorithm are described.

We recorded sets of particle trajectories with 60×10^6 samples at the sampling frequency $f_{\mathrm{sample}} = 1.78\,\mathrm{MHz}$, which corresponds to the particle motion for $\sim 33\,\mathrm{s}$. Such a data ensemble was recorded at different pressures ranging from $2.5{\cdot}10^{-2}\,\mathrm{mBar}$ up to 10 mBar. The acquired voltage signal was transformed to the nanoparticle position using the calibration constant $C_{\mathrm{V}\to\mathrm{m}}$. Since the cross–talks between different coordinate axes become more significant at lower pressures and could influence the analysis of the particle motion in a selected axis, the nanoparticle trajectories recorded at pressures below 1 mBar were filtered in the frequency domain using a bandpass filter. This process preserved only the leading oscillation peak in the selected axis while amplitudes at other frequencies were set to zero. The passband in the x axis was set to $87{-}96\,\mathrm{kHz}$ and in the y axis $72{-}90\,\mathrm{kHz}$.

Using the filtered nanoparticle positions $x(t)$, we calculated its velocities $v_x(t)$ using the central difference rule $v_x(t) = [x(t + \Delta t) - x(t - \Delta t)]/2\Delta t$, where Δt is the time step given by the sampling frequency during the data acquisition $\Delta t = 1/f_{\mathrm{sample}}$. Using the computer simulations, the experimental sampling frequency was verified to be sufficient for the calculation of the instantaneous particle velocity. Figure 3.11a shows a two dimensional histogram obtained from a long–time data set showing a probability density of the nanoparticle in a phase space. The phase space consists of the measured nanoparticle position and the calculated velocity. These two parameters were also used for the determination of the initial conditions in the trajectory–selection process.

The initial conditions were defined as intervals in the particle position and its velocity $x_0 - \Delta x_0 \leq x_0 \leq x_0 + \Delta x_0$ and $v_{x0} - \Delta v_{x0} \leq v_{x0} \leq v_{x0} + \Delta v_{x0}$, where both Δx_0 and Δv_{x0} are small but slightly bigger than the experimental uncertainty of measured positions and calculated velocities. The uncertainties were estimated using the noise level determined during the calibration process, see Section 3.4. The standard deviation of the white noise was $\sim 2\,\mathrm{nm}$ which is about 3 % of the particle standard deviation from the optical–trap center. Selecting the desired trajectory with the defined initial conditions (defined by the cross marks in Fig. 3.11a), we looked for the starting point in the small region of the phase space. If several consecutive points were found, the selected one gave the minimal separation from x_0.

When such an event was detected, the trajectory of the length typically $100\,\mu\mathrm{s}$ starting close to the defined point in the phase space (x_0, v_{x0}) was added into an statistical ensemble of trajectories. The remaining part of the recorded trajectory

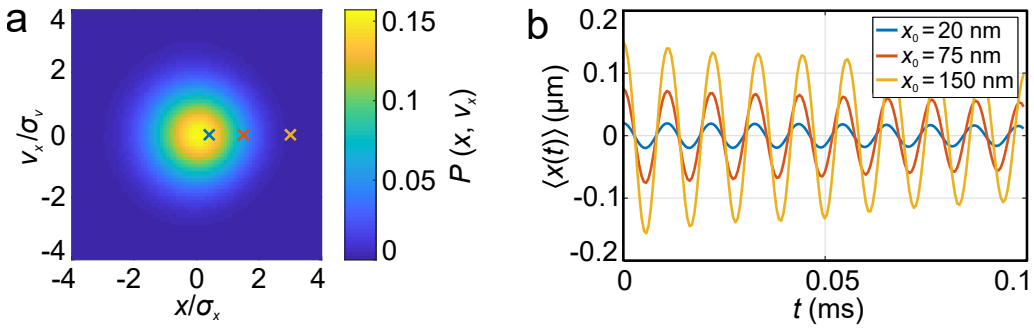

Fig. 3.11: (a) Probability density function of the nanoparticle in the phase space consisting of the position x and the velocity v_x normalized to their standard deviations σ_x and σ_v, respectively. 33s long data set was recorded at the ambient pressure 1 mBar. Cross marks define initial conditions of the trajectories shown in (b). (b) Mean trajectories obtained by averaging the trajectory sections starting at the same point in the phase space $(x_0, 0)$ marked in (a). Adapted from [18].

was scanned for the same event and other trajectories were added into the ensemble of trajectories starting at the vicinity of the point in the phase space (x_0, v_{x0}). If more selected trajectories overlapped in time, only one of them was taken into the further data processing. Depending on the selected initial conditions (x_0, v_{x0}), the ensemble contained from tens up to $\sim 5 \times 10^4$ snippets of trajectories. From the resulting statistical ensemble, the average trajectory $\langle x(t)\rangle$, velocity $\langle v_x(t)\rangle$ and their variances $\mathrm{Var}\,(x) = \langle x^2(t)\rangle - \langle x(t)\rangle^2$, $\mathrm{Var}\,(v_x) = \langle v_x^2(t)\rangle - \langle v_x(t)\rangle^2$ were calculated.

The typical averaged trajectories $\langle x(t)\rangle$ starting at the defined initial point $(x_0, 0)$ are shown in Fig. 3.11b. The starting points are for clarity also marked in the phase–space diagram in Fig. 3.11a by crosses with the corresponding colour. It can be clearly observed that the frequency of the oscillations is dependent on the initial amplitude x_0 of the averaged trajectories, the larger the amplitude, the lower the oscillation frequency. Another comparison was performed for the trajectories recorded at different ambient pressures. In Fig. 3.12a, mean phase–space trajectories starting at the same initial point but recorded at different ambient pressures are plotted. The phase–space trajectories spin inwards to the central point $(0, 0)$, as expected for the classical damped oscillator. Higher pressure corresponds to stronger damping and faster convergence of the trajectory to the center. The mean trajectories $\langle x(t)\rangle$ are shown in Fig. 3.12b. Whilst the oscillation frequency is very similar for all pressures, the higher pressure causes the higher damping of the particle oscillations.

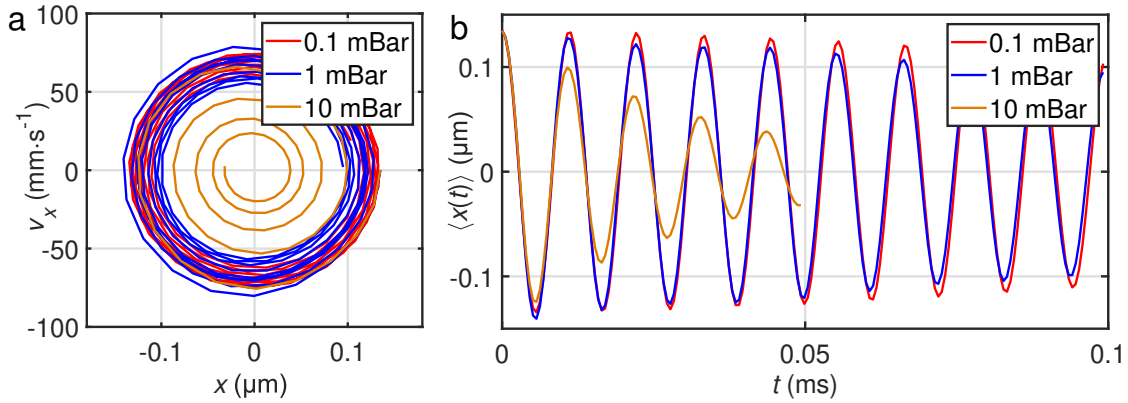

Fig. 3.12: (a) Mean phase–space trajectories starting at the same initial condition (130 nm, 0) for different pressures. (b) Time evolution of the mean position $\langle x(t) \rangle$ for different pressures.

3.6 Novel methodology (DOA) for determination of parameters of the Duffing oscillator

Employing the averaged trajectories and their variances, we have developed a new methodology for estimation of the parameters of the nonlinear Duffing–type oscillator represented by a levitated nanoparticle. Since the stochastic system described by Eq. 3.22 is analysed through the trajectory moments, the time evolution of the particle post–processed averaged position in the x axis can be described by the deterministic Duffing equation (DDE)

$$\ddot{x}\left(t\right) + \Gamma \dot{x}\left(t\right) + \Omega_0^2 x \left(1 - \xi_x x^2\right) = 0. \tag{3.30}$$

Using the presented Duffing oscillator approximation (DOA), local analysis near the center of the optical trap ($x = 0$) at low pressures leads to a solution of the lowest perturbation order in the form of a damped oscillator [192, p. 91]

$$x\left(t\right) = x_0 e^{-\frac{\Gamma}{2}t} \cos\left(\Omega_{\mathrm{D}} t + \theta_0\right), \tag{3.31}$$

where the amplitude x_0 and the phase θ_0 are defined by the initial conditions at $t = 0$. The oscillation frequency Ω_{D} is then expressed as [192, p. 92]

$$\Omega_{\mathrm{D}} = \sqrt{\Omega_0^2 \left(1 - \frac{3}{4}\xi_x x_0^2\right) - \left(\frac{\Gamma}{2}\right)^2}, \tag{3.32}$$

where Ω_0 is the eigenfrequency of the harmonic oscillator oscillating with zero amplitude. Considering a weakly damped nonlinear oscillator, its eigenfrequency is defined as

$$\Omega_{\mathrm{H}} = \sqrt{\Omega_{\mathrm{D}}^2 + \left(\frac{\Gamma}{2}\right)^2}. \tag{3.33}$$

Since the oscillation frequency Ω_{D} depends on the initial amplitude x_0, the eigenfrequency is amplitude dependent, too. For a slightly nonlinear Duffing oscillator, the eigenfrequency can be written as follows

$$\Omega_{\mathrm{H}} \simeq \Omega_0 \left(1 - \frac{3}{8}\xi_x x_0^2\right), \tag{3.34}$$

which is the identical expression for the frequency shift $\Delta\Omega$ defined by Eq. 3.23 already briefly discussed above.

The frequency shift increases quadratically with the amplitude and so for the small oscillation amplitudes, the frequency shift is negligible. Therefore, in the following we divided the oscillator description into two regions. Firstly we focus on the trajectories starting at the center point of the phase space, where the potential nonlinearities can be neglected. Then we deal with the whole range of the oscillator amplitudes where the dependence of the eigenfrequency on the amplitude are crucial.

3.6.1 Idealized harmonic oscillations

Close to the potential minimum, the anharmonicities are negligible and the weakly damped nonlinear oscillator behaves predominantly as harmonic [21]. The motion of such an oscillator can be simply described by its eigenfrequency Ω_0 and the surrounding damping rate Γ while excited by the thermal surrounding characterized by the temperature T. The oscillator moving near the potential minimum is naturally thermalized into its thermal equilibrium. For the linearized harmonic oscillator, the process of the thermalization from the oscillator state close to the phase–space center point can be described analytically. This transient motion is expressed via the position variance [167]

$$\mathrm{Var}\,(x) = \frac{k_{\mathrm{B}} T_{\mathrm{TR}}}{m\Omega_0^2}\left\{1 - \mathrm{e}^{-\Gamma t}\left[\frac{\Omega_0^2}{\Omega_{\mathrm{D}}^2} - \frac{\Gamma}{2\Omega_{\mathrm{D}}}\sin\left(2\Omega_{\mathrm{D}} t\right) + \frac{\Gamma^2}{4\Omega_{\mathrm{D}}^2}\cos\left(2\Omega_{\mathrm{D}} t\right)\right]\right\}, \tag{3.35}$$

where T_{TR} represents the effective transient temperature.

This transient motion is equivalent to a direct observation of the particle heating from its cooled state in experimental systems [28]. However, in our system the cooling process is not desired and the initial state can be selected in the data post–processing described in the previous section. The virtual cooling was preformed by selecting the initial conditions at $(x_0, v_{x0}) = (0,0) \pm (2\,\mathrm{nm}, 1\,\mathrm{mm}\cdot\mathrm{s}^{-1})$ and the variance $\mathrm{Var}\,(x)$ was determined from the statistical ensemble of the experimental data for long enough acquisition time to cover the thermalization. The size of the selected interval Δx_0 and Δv_{x0} corresponded to the initial center–of–mass temperature about 0.9 K.

The time dependences of the position variance calculated from the experimental data recorded at different ambient pressures are shown in Fig. 3.13. The slope of the variance curve in the first part characterizes the thermalization rate, i.e. the damping coefficient Γ, while the saturated level corresponds to the effective transient temperature T_{TR}. Fitting the analytical formula 3.35 to the plotted data, the parameters Γ, T_{TR} and Ω_0 are determined, see the red dashed curves in Figs. 3.13a and 3.13b.

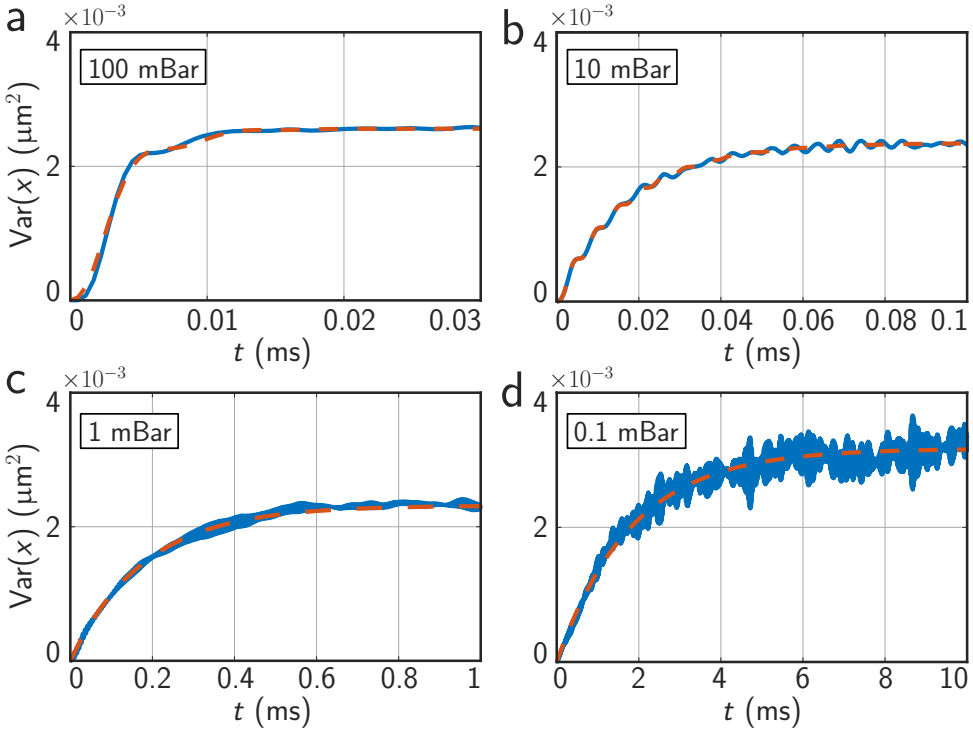

Fig. 3.13: Time dependence of the position variance $\mathrm{Var}\,(x)$ determined from the ensemble of trajectories starting at $(x_0, v_{x0}) = (0,0) \pm (2\,\mathrm{nm}, 1\,\mathrm{mm}\cdot\mathrm{s}^{-1})$. Experimental data are represented by blue curves, the red curves depict fits (a) and (b) by Eq. 3.35 and (c) and (d) by Eq. 3.36.

In a weakly damped system ($\Gamma \ll \Omega_{\mathrm{D}}$), the sinusoidal oscillations can be neglected and the analytical expression can be simplified into the following form

$$\mathrm{Var}\,(x) = \frac{k_{\mathrm{B}} T_{\mathrm{TR}}}{m\Omega_0^2}\left\{1 - \mathrm{e}^{-\Gamma t}\right\}. \tag{3.36}$$

Such fitting to the experimental data for a weakly damped oscillator is shown in Figs. 3.13c and 3.13d. This formula does not provide us directly with the information about the temperature T_{TR} and eigenfrequency Ω_0 but one of those values has to be determined by another method, as we describe in the following.

In the presented plots in Fig. 3.13, the thermalization process is slowed down with the decreasing pressure. (Note the time scales vary.) This result corresponds with

the theory that the damping coefficient Γ decreases with the decreasing ambient pressure [157]. The saturation levels varies with the pressure, too. Assuming the approximately constant eigenfrequency, the increase in the saturation level means the increase in the effective transient temperature T_{TR}.

3.6.2 Nonlinear oscillations

If the oscillator is displaced far from the center of the optical trap, the potential nonlinearities start to influence noticeably the oscillator motion. At lower pressures ($\Gamma \ll \Omega_{\mathrm{D}}$), the oscillator amplitude does not change significantly over a few periods neither due to the damping nor due to the thermal heating and such a motion can be described by Eq. 3.31.

As explained above, the oscillation frequency depends on the initial amplitude. This dependence is demonstrated in Fig. 3.14. Different initial conditions with various initial amplitude x_0 and zero velocity v_0 are chosen, as marked with crosses in Fig. 3.14a and the corresponding averaged phase portraits are plotted in Fig. 3.14b. Since the damping is weak, the phase–space trajectories spiral slowly inwards towards the center point and rather stay on their orbits during the short–time development ($< 0.1\,\mathrm{ms}$). The dashed curves represent the oscillator position in the phase space for the different oscillation amplitudes at the defined time from the initial condition. With the time the dashed curve bends backwards indicating the outer phase–space trajectories orbit slower comparing to the inner trajectories. This observation is consistent with the previous discussion about the frequency dependence on the oscillation amplitude, the larger the amplitude, the smaller the eigenfrequency (see Eq. 3.34).

In order to obtain the coefficient of Duffing nonlinearity ξ_x characterizing the frequency dependence on the oscillation amplitude, we focused on the mean trajectories $\langle x(t) \rangle$ starting with different oscillation amplitudes x_0. An example of such trajectories is shown in Fig. 3.15a. The mean trajectories $\langle x(t) \rangle$ were fitted by Eq. 3.31, which provided us with the information about the oscillation frequency Ω_{D}. Ω_{D} was then recalculated into the eigenfrequency Ω_{H} using Eq. 3.33 and the damping rate Γ determined above. The eigenfrequencies for different initial oscillation amplitudes and ambient pressures are plotted in Fig. 3.15b. The data points obtained by fitting the trajectories in Fig. 3.15a are highlighted with circles of the corresponding colour. The amplitude dependence of the eigenfrequency exhibits the expected parabolic profile described by Eq. 3.34. Fitting the plotted data (dotted curves), the values of the coefficient of nonlinearity ξ_x together with the eigenfrequency of the zero–amplitude oscillation Ω_0 can be estimated.

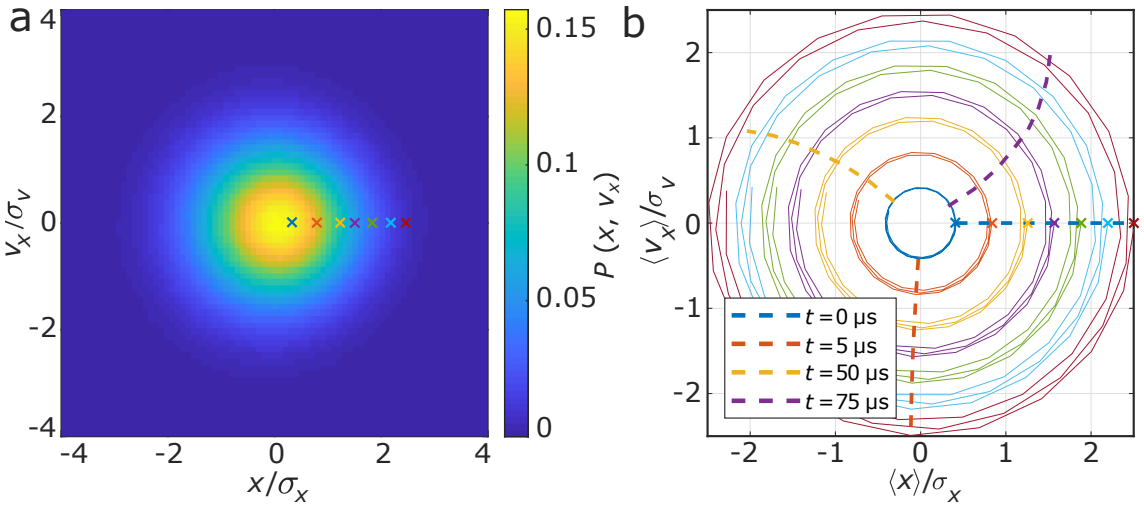

Fig. 3.14: (a) Probability density function of the oscillator in the position–velocity phase space at the ambient pressure 1 mBar. Cross marks define the initial conditions of the phase–space trajectories shown in (b). (b) Phase portraits of the motion in the x axis reconstructed using the averaged experimental data normalized to standard deviations. The phase–space trajectories recorded at the ambient pressure 1 mBar start at different initial positions $x_0 = 20$, 40, 60, 75, 90, 105, and 120 nm with the fixed initial velocity $v_{x0} = 0$. The dashed curves connect the phase space positions corresponding to the same times t but different initial amplitude x_0; adapted from [18].

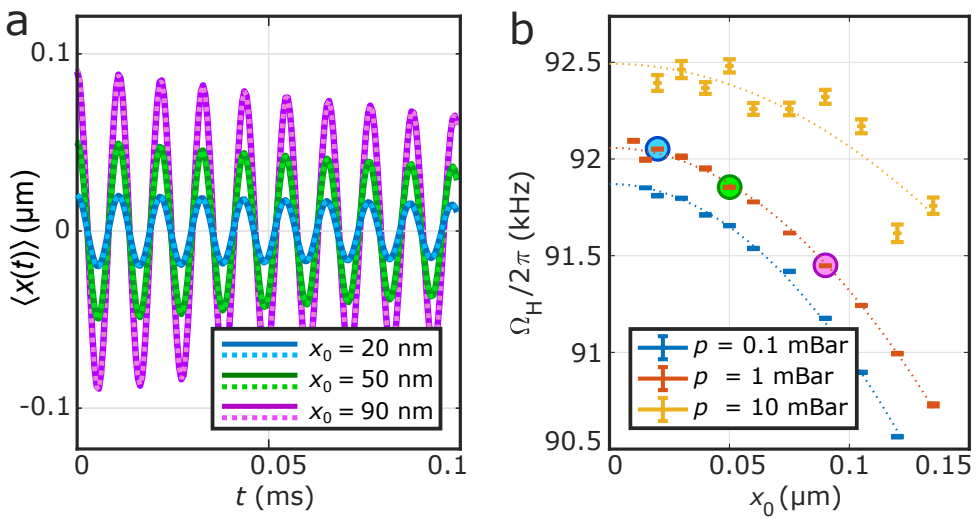

Fig. 3.15: (a) Mean trajectories starting at the different points in the phase space $(x_0, 0)$ at pressure 1 mBar. The dashed curves represent the fit to the experimental data by Eq. 3.31. (b) Eigenfrequency of a damped Duffing oscillator Ω_{H} as a function of the initial amplitude x_0 for various ambient pressures is obtained from the fitting by Eq. 3.31 to the post–processed experimental data, as shown in (a) (corresponding points marked by coloured circles). The oscillation frequency Ω_{D} is recalculated into the eigenfrequency Ω_{H} using Eq. 3.33 and the damping Γ obtained above. The data points are fitted by Eq. 3.34, see the dotted curves; adapted from [18].

3.6.3 Procedure summary

Here an overview of the innovative method based on the Duffing oscillator approximation (DOA) is presented. The instructions for the determination of the oscillator parameters (medium damping Γ, oscillation frequency Ω_{D}, eigenfrequency Ω_0, coefficient of Duffing nonlinearity ξ_x and effective transient temperature T_{TR}) are given and the obtained parameters are plotted in Fig. 3.16. The results are discussed later in Section 3.9.

Medium damping Γ

Eq. 3.35 is fitted to the mean variance $\mathrm{Var}\,(x)$ of trajectory ensembles starting at $(x_0, v_{x0}) = (0,0) \pm (2\,\mathrm{nm}, 1\,\mathrm{mm}\cdot\mathrm{s}^{-1})$. Besides the damping coefficient Γ, the effective transient temperature T_{TR} is also determined. For lower ambient pressures ($p \leq 1\,\mathrm{mBar}$), the medium damping Γ is obtained by fitting Eq. 3.36 to the position variance $\mathrm{Var}\,(x)$ and the saturated–level pre–factor $k_{\mathrm{B}}T_{\mathrm{TR}}/\,(m\Omega_0)$ is extracted, too. Examples of such fitting are shown in Fig. 3.13.

Oscillation frequency Ω_{D}

Oscillation frequency Ω_{D} is determined by fitting Eq. 3.31 to the mean trajectories $\langle x(t)\rangle$ over a few periods (~ 10) for different initial amplitudes x_0. The values of x_0 may reach up to a double of the standard deviation of particle positions in the trap, ensembles of trajectories with bigger initial amplitudes were not sufficiently large to reliably analyse the mean trajectories. Examples of such fitting are shown in Fig. 3.15a.

Eigenfrequency Ω_0 and coefficient of Duffing nonlinearity ξ_x

Employing Eq. 3.33 together with the oscillation frequency Ω_{D} and the medium damping Γ determined above provides us with the eigenfrequency of a damped Duffing oscillator Ω_{H} for different initial amplitudes x_0. Fitting Eq. 3.34 to the dependence of Ω_{H} on x_0 gives the eigenfrequency Ω_0 and the coefficient of Duffing nonlinearity ξ_x. Examples of such fitting are shown in Fig. 3.15b.

Effective transient temperature T_{TR}

Determination of the damping coefficient Γ described above provides us with the effective transient temperature T_{TR} directly. In case of lower ambient pressures, the temperature is determined from the pre–factor $k_{\mathrm{B}}T_{\mathrm{TR}}/\,(m\Omega_0)$ knowing the eigenfrequency Ω_0 and the oscillator mass. In our case the mass was calculated from the declared diameter (170 nm) and its density ($2000\,\mathrm{kg/m^3}$).

3.7 Numerical solution of deterministic Duffing equation (DDE)

In order to compare our novel methodology DOA for the estimation of the Duffing–oscillator parameters, DDE given by Eq. 3.30 was solved using the direct numerical integration (Matlab, ODE45 function) under the selected initial conditions. We fitted its numerical solution to all averaged trajectories $\langle x(t)\rangle$ for various initial conditions $(x_0, 0)$ at once. The contribution of trajectories was weighted as x_0^{-2} so that all trajectories contributed to the residual sum with the same weight. Employing the described procedure, we arrived into the values of medium damping Γ, eigenfrequency Ω_0 and coefficient of Duffing nonlinearity ξ_x. The obtained parameters are plotted in Fig. 3.16 and discussed later in Section 3.9.

3.8 Simulations based on stochastic Duffing equation (SDE)

In order to verify the PSD, DOA and DDE methods used for the determination of parameters of the Duffing oscillator represented by an optically levitated nanoparticle, we simulated the particle motion described by the 1D stochastic Duffing equation (SDE) given by Eq. 3.22 based on the Verlet scheme [193]. In the stochastic simulation, we considered the nanoparticle randomly moving in the optical potential with a Gaussian profile of the beam intensity. Since we studied the motion of the nanoparticle, a contribution of the scattering force was negligible and only the gradient force was taken into account.

The values of the input parameters were taken from the experimental results obtained by the DDE (Ω_0 and ξ_x) and DOA (T_{TR}) methods. The damping coefficient Γ was calculated by the theoretical model [157]. In case of the optically levitated nanoparticle, there are two contributions to the total damping rate, from the photon shot noise [124] and the surrounding air molecules [23]. In general, at higher ambient pressures down to 10^{-6} mBar the damping caused by the discrete photon nature of light is negligible and the dominant damping mechanism is determined by the collisions with the background gas [23, 194]. For a spherical particle in a rarefied gas, the damping rate is [23]

$$\Gamma = \frac{6\pi\mu a}{m}\frac{0.619}{0.619 + \mathrm{Kn}}\left(1 + c_{\mathrm{K}}\right), \tag{3.37}$$

where a and m and the particle radius and mass, $\mu = 17.7\,\mu$Pa·s is the viscosity coefficient of air, $c_{\mathrm{K}} = 0.31\mathrm{Kn}/\left(0.785 + 1.152\mathrm{Kn} + \mathrm{Kn}^2\right)$ and $\mathrm{Kn} = \bar{l}/a$ is the Knudsen number with the mean free path $\bar{l} = k_{\mathrm{B}}T/\left(\sqrt{2}\sigma_{\mathrm{gas}}p\right)$, where $\sigma_{\mathrm{gas}} = \pi d_{\mathrm{gas}}^2$ and

$d_{\mathrm{gas}} = 0.372\,\mathrm{nm}$ is the diameter of the air molecules. In our experimental pressure regime when $\mathrm{Kn} \gg 1$, the medium damping is linearly proportional to the ambient pressure p [23, 115]

$$\Gamma = 0.619\sqrt{72}\pi^2 \frac{a^2 \mu d_{\mathrm{gas}}^2}{m k_{\mathrm{B}} T} p. \tag{3.38}$$

For each experimental ambient pressure, 200 trajectories of the nanoparticle with random initial conditions were simulated with a time step corresponding to the experimental sampling frequency ($f_{\mathrm{sample}} = 1.78\,\mathrm{MHz}$) and the total duration of a single trajectory was 1 s. The simulated trajectories were processed in the same way as experimental data by PSD, DOA and DDE methods. The obtained parameters are compared with the input ones in Fig. 3.16 marked with circles with colours of the corresponding processing method.

3.8.1 Extension into the 3D space

The simulations were also extended into the 3D space in order to improve the approximation of the experiment on the nanoparticle moving in the 3D potential. We assume the intensity of the optical potential has a Gaussian profile in all three coordinate axes

$$U(\mathbf{r}) = -U_0\, \mathrm{e}^{-2\frac{x^2}{{w_x}^2} - 2\frac{y^2}{{w_y}^2} - 2\frac{z^2}{{w_z}^2}}, \tag{3.39}$$

where U_0 is the depth of the trapping potential which is related to the total laser power and w_x, w_y, and w_z are the radii of the Gaussian beam waists along the coordinate axes, respectively. Neglecting the scattering force, the force acting on the nanoparticle in the optical potential is expressed as $\mathbf{F} = -\nabla U(\mathbf{r})$, which in its individual components reads

$$F_x = -2\xi_x\, U_0\, x\, \exp\left[-\xi_x x^2 - \xi_y y^2 - \xi_z z^2\right], \tag{3.40}$$

$$F_y = -2\xi_y\, U_0\, y\, \exp\left[-\xi_x x^2 - \xi_y y^2 - \xi_z z^2\right], \tag{3.41}$$

$$F_z = -2\xi_z\, U_0\, z\, \exp\left[-\xi_x x^2 - \xi_y y^2 - \xi_z z^2\right]. \tag{3.42}$$

In the presented expression, the relation between the beam waist and the coefficient of nonlinearity was used [21, 173]

$$\xi_i = 2/w_i^2, \tag{3.43}$$

where $i = x, y, z$.

The force components are further described using the eigenfrequency $\Omega_{i0} = \sqrt{2\xi_i U_0/m}$ and simplified employing a Taylor expansion for coupled Duffing oscillators

$$F_x = -m\Omega_{x0}^2\ x\ \exp\left(-\Psi\right) \simeq -m\Omega_{x0}^2\ x\ \left(1-\Psi\right), \tag{3.44}$$

$$F_y = -m\Omega_{y0}^2\ y\ \exp\left(-\Psi\right) \simeq -m\Omega_{y0}^2\ y\ \left(1-\Psi\right), \tag{3.45}$$

$$F_z = -m\Omega_{z0}^2\ z\ \exp\left(-\Psi\right) \simeq -m\Omega_{z0}^2\ z\ \left(1-\Psi\right), \tag{3.46}$$

$$\Psi = \xi_x \left(x^2 + \frac{\Omega_{y0}^2}{\Omega_{x0}^2} y^2 + \frac{\Omega_{z0}^2}{\Omega_{x0}^2} z^2 \right). \tag{3.47}$$

The described force components were utilized for the full 3D simulations, where the input values were taken from the experiment. The values of Ω_{x0} and Ω_{y0} were obtained by the DDE method and the value of Ω_{z0} was determined from the PSD fit in the z axis. The parameter ξ_x was set by the DDE method, Γ was calculated using the theoretical formula given by Eq. 3.38, and the temperature was set as an average of T_x and T_y obtained by the DOA method. The volume of simulations was same as in case of the 1D simulations and the simulated trajectories were evaluated by the PSD, DOA and DDE methods. The obtained values of parameters are compared with the input ones in Fig. 3.16 marked with crosses with colours of the corresponding processing method.

3.8.2 Eigenfrequency correction

Since the nanoparticle is moving in the whole 3D space, its oscillations in the x axis are influenced by the motion in other two axes. The oscillator moves out of the beam center and consequently, the optical potential in the x axis is weaker on average comparing to the 1D case when the particle is moving only along a single axis. Therefore, the experimentally determined oscillation frequency is lower due to the weakened averaged potential.

In order to express the dependence of the eigenfrequency Ω_{x0} in the x axis on the position in the y and z axes, Eq. 3.44 is rewritten into the following form

$$F_x = -m\Omega_{x0}^2(y,z)\ x\ \exp\left(-\xi_x x^2\right), \tag{3.48}$$

where

$$\Omega_{x0}(y,z) = \Omega_{x0} \exp\left(-\frac{\xi_x \Omega_{y0}^2}{2\Omega_{x0}^2} y^2\right) \exp\left(-\frac{\xi_x \Omega_{z0}^2}{2\Omega_{x0}^2} z^2\right). \tag{3.49}$$

In the experiment, it is assumed that the motion between different coordinate axes is decoupled and thus the particle oscillates with an averaged oscillation frequency defined by the weakened optical potential. This frequency shift can be

analysed via the probability density of the particle position in the yz plane defined as follows

$$P(y,z) = \frac{1}{2\pi\sigma_y\sigma_z} \exp\left(-\frac{y^2}{2\sigma_y^2} - \frac{z^2}{2\sigma_z^2}\right), \tag{3.50}$$

where σ_y, and σ_z are the standard deviations of the axial harmonic motion in the corresponding axes. The standard deviation can be estimated from the equipartition theorem given by Eq. 3.17 assuming the small Duffing nonlinearity

$$\sigma_i^2 \simeq \frac{k_\mathrm{B}T}{m\Omega_{i0}^2}. \tag{3.51}$$

The averaged eigenfrequency in the x axis is then calculated as

$$\bar{\Omega}_{x0} = \iint \Omega_{x0}(y,z)P(y,z)\mathrm{d}y\mathrm{d}z = \frac{\Omega_{x0}}{\sqrt{1+\sigma_y^2\xi_x\frac{\Omega_{y0}^2}{\Omega_{x0}^2}}\sqrt{1+\sigma_z^2\xi_x\frac{\Omega_{z0}^2}{\Omega_{x0}^2}}}. \tag{3.52}$$

Combining Eqs. 3.51 and 3.52, the eigenfrequency in the x axis averaged in the yz plane reads

$$\bar{\Omega}_{x0} = \frac{\Omega_{x0}}{1+\frac{k_\mathrm{B}T\xi_x}{m\Omega_{x0}^2}}. \tag{3.53}$$

Analysing the results of the 3D simulations, the obtained eigenfrequency is recalculated using Eq. 3.53 in order to correctly compare the input parameters. This correction produces a frequency shift about 0.5 %, which is quite significant deviation, as Fig. 3.16 demonstrates.

3.9 Comparison of all described methods

In this Section, the parameters of the Duffing oscillator obtained by methods described above are presented and discussed. We compare the novel developed method DOA described in Section 3.6 with the numerical solution of DDE (Section 3.7) and the commonly used PSD method. In the PSD method, the power spectral density of position was fitted by Eq. 3.16 and the eigenfrequency Ω_0 and the damping coefficient Γ was determined. The effective spectral temperature T_SP was obtained by integrating the area under the oscillation peak in the power spectral density of the particle velocity, see Eq. 3.25. Nevertheless, the PSD method does not provide us with the information about the coefficient of Duffing nonlinearity because the method assumes a harmonic oscillator. The damping coefficient Γ is also compared with the theoretically predicted value given by Eq. 3.38.

Further, we obtained trajectories using SDE by means of computer simulations in 1D and 3D space for parameters determined from the experiment and they were processed in the same way as the measured trajectories, see Section 3.8. All obtained

parameters at different ambient pressures are compared in Fig. 3.16 for the x and y axes. In the following, we discussed all the oscillator parameters individually.

3.9.1 Eigenfrequency Ω_0

Over the whole range of the examined ambient pressures, the DOA and DDE methods gives the higher eigenfrequency values comparing to the PSD method. This shift of $\sim 1\,\mathrm{kHz}$ is caused by the averaging of the oscillation frequencies in the PSD method over all oscillation amplitudes. However, the eigenfrequency Ω_0 is defined as the eigenfrequency for the oscillations with zero amplitude, which the DOA and DDE methods can provide. At higher ambient pressure, this frequency shift between different methods gets smaller. The peak in the PSD is broadened mainly by the ambient damping and the influence by the nonlinear behaviour is negligible.

In the SDE simulation, the input parameter of the eigenfrequency was taken as the value obtained via the DDE method analysing the experimental data. In case of the 1D simulations, the determined values follow the same trends as the experimental data, only a weak bias of about 0.3 % towards higher frequencies can be observed in the DOA and DDE methods. On the other hand, the results from the 3D simulations, where the frequency correction described in Section 3.8.2 was taken into account, exhibit a drift towards lower frequencies.

The DDE method provides the most reliable values. Nevertheless, the novel DOA method is still applicable for the weakly nonlinear oscillator and is more precise comparing to the commonly used PSD method. The values of eigenfrequency Ω_0 vary with the ambient pressure. This drift is caused by the fluctuation of the optical power in the trapping beam, which is observable in both, the x and y axes.

3.9.2 Coefficient of Duffing nonlinearity ξ

In case of the coefficient of Duffing nonlinearity, only the DOA and DDE methods are compared. The PSD method assuming the harmonic oscillator does not give any information about the coefficient of Duffing nonlinearity ξ. The DDE method provides slightly higher values of ξ in both axes comparing to the DOA method. The difference between DOA and DDE methods increases rapidly at the ambient pressures above 2 mBar. At higher pressure, the oscillations are highly damped and the eigenfrequency for different oscillation amplitudes Ω_H utilized for the determination of ξ cannot be determined with a sufficient precision.

In the SDE simulations, again the values obtained from the experimental data through the DDE method were utilized. Both, the 1D and 3D simulations, provide

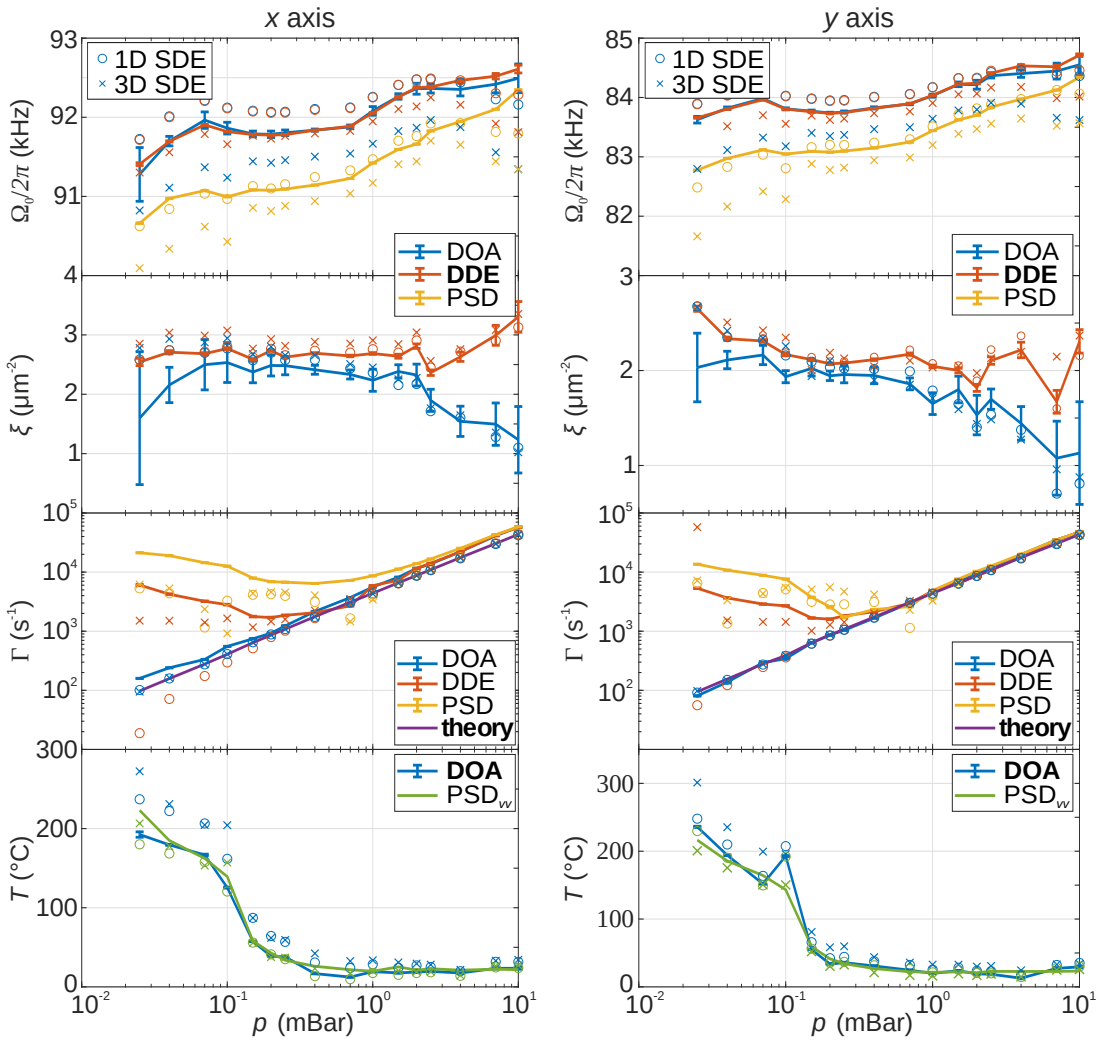

Fig. 3.16: Comparison of the pressure dependence of the oscillator parameters determined by all described methods. Left and right columns correspond to the x and y axes, respectively. (row 1) Eigenfrequency Ω_0; (row 2) coefficient of Duffing nonlinearity ξ; (row 3) damping coefficient Γ; (row 4) effective temperature T. Full curves represent the analysis of the experimental data. Circles $\circ$ and crosses $\times$ correspond to the analysis of the 1D and 3D SDE simulations analysed by different methods, where we used parameters obtained by the analysis of experimental data with the method marked bold in the legend. Colour of each symbol corresponds to the method of analysis depicted in the legend. All errorbars correspond to the 95% confidence intervals and are directly based on the results of the nonlinear least square fitting or the results of the fits are combined by the error propagation law. Adapted from [18].

the values corresponding to the experimental results. Even the shift in the eigenfrequency at higher pressures in the DOA method occurs in the 1D and 3D simulated data.

The mean values and standard errors of the coefficient of Duffing nonlinearity obtained by the DDE method are $\xi_x = (2.7 \pm 0.2)\ \mu\text{m}^{-2}$ and $\xi_y = (2.1 \pm 0.2)\ \mu\text{m}^{-2}$. The result can be compared with the theoretical estimation of the coefficient of Duffing nonlinearity characterized by Eq. 3.43. The beam waist $w_0 = 0.85\,\mu\text{m}$ was determined in Zemax software package in accordance to aberrations of the focusing lens at the trapping wavelength but polarization effects were not taken into account. Therefore, the simulated beam waist was the same for the x and y axes. The coefficient of Duffing nonlinearity was then theoretically estimated to the value $\xi = 2.76\,\mu\text{m}^{-2}$. This estimation corresponds quite well with the values determined by the DDE method from our experimental data.

3.9.3 Damping coefficient Γ

The damping coefficient Γ was obtained from the experimental data by the DOA, DDE and PSD methods and these values were compared with the theoretically predicted values given by Eq. 3.38. Apparently, only the DOA method provides reliable results even at lower pressures and the damping coefficient gets linearly proportional to the ambient pressure. At higher pressures above 0.5 mBar, the DDE and PSD methods show a good agreement with the theoretical model, too. However, at lower pressures the values do not decrease with the pressure and the deviations of more than one order of magnitude comparing to the theoretically predicted value appeared. In the PSD method, the increase in the damping coefficient is caused by the nonlinear broadening and deformation of the oscillation peak at lower pressures, as shown in Fig. 3.4b. Thus the wider peak results in higher values of the damping coefficient while fitting by Eq. 3.16. In the DDE method, the discrepancy cannot be explained directly, thus the method was verified on the simulated data.

In the simulations, the input values were determined by the theoretical model. In case of the PSD and DOA methods, the values revealed almost the same tendency as the analysis of the experimental data for both, 1D and 3D simulated trajectories. The DDE method applied on the 1D simulated data follows well the linear dependence even at lower pressures. However, the processing of 3D simulated trajectories by the DDE method showed the same trend as in case of the experimental data and the values deviate at lower pressures. Therefore, we deduced that the described discrepancies at lower pressures are caused by the cross–talks between different coordinate axes. The DOA method thus provides us with the most reliable values even at lower pressures while the DDE and PSD methods fail.

3.9.4 Effective temperature T

The effective temperature T was determined by two methods, DOA and PSD of particle velocities. Both ways gave comparable results. This time the PSD was not fitted by the theoretical formula but the velocity PSD was integrated under the oscillation peak. At higher ambient pressures above 0.5 mBar, the effective temperature is approximately constant and its value is about the ambient temperature. At lower pressures, the effective temperature strongly increases up to 200 °C. This trend was already observed in [28] and is caused by a low heat dissipation by conduction at low ambient pressures. At even lower pressures, the temperature saturation is expected because the absorbed heat is dissipated only by the particle radiation independently on the ambient pressure. However, in our experimental system lower pressures could not been achieved since the nanoparticle escaped from the optical trap due to its heating and noise in the system, such as laser noise or vibrations [14].

As the input parameter in the SDE simulations, the values obtained by the DOA method were used. The effective temperature of the simulated trajectories follows well the experimental trend and no remarkable difference between the 1D and 3D simulations was observed.

3.10 Conclusions

The optically trapped particle in vacuum behaves as a nanomechanical oscillator that could be utilized for ultrasensitive force measurements or examination of quantum effects on microscopic objects. For that purposes, the precise characterisation of oscillator parameters is desired. However, the commonly used method based on displacement power spectral density (PSD) evaluates only the oscillator steady states and assumes a harmonic oscillator which is not always applicable. Therefore, we developed a new approach how to characterize a slightly nonlinear Duffing–type oscillator and its parameters such as eigenfrequency, temperature, damping and coefficient of Duffing nonlinearity during its transient dynamics. The novel procedure is based on the post–processing of the recorded particle trajectories. Selecting the trajectories with the defined initial state in the phase space, the averaged trajectories and variances are obtained and analysed.

The developed method based on the Duffing oscillator approximation (DOA) was compared with the numerical solution of the deterministic Duffing equation (DDE) and the PSD method. In order to verify the reliability of the utilized methods, we compared the parameters determined from the experimental trajectories with the data sets obtained from simulations based on the stochastic Duffing equation (SDE). The comparisons of all determined parameters are presented in Fig. 3.16.

Examining only the region of the experimental parameters at pressures below 1 mBar, the DOA and DDE methods can determine the eigenfrequency Ω_0 with a precision better than 1 % and the coefficient of Duffing nonlinearity ξ with a precision better than 14 %. The damping coefficient Γ is the most precisely determined by the DOA method with a precision better than 1 % while other methods are inapplicable at lower pressures and the error is of several orders of magnitude. At lower pressures, the PSD method is suitable only for the determination of the effective temperature with the precision of 1 % while the DOA method performs worse with a precision about 14 %.

In conclusion, the presented DOA and DDE methods can reliably characterize all important parameters describing the Duffing oscillator. These methods are applicable for very low temperatures down to quantum mechanical motion and also at low pressures under 1 mBar, where the nonlinearity starts to play a significant role and a peak profile in the PSD deforms and deviates from the ideal Lorentzian shape.

CONCLUSIONS

The presented thesis was focused on investigating the behaviour of optically trapped particles in structured optical fields and various surrounding environments. Rich dynamical processes of optically trapped objects were examined experimentally and the results were supported by theoretical predictions based on extensive numerical simulations. Understanding the underlying physical mechanisms of particle performance arising from the light–matter interaction can open new opportunities for applications in the field of optics, biology, and quantum physics.

In the presented work, two main branches of the optical trapping were presented, overdamped and underdamped regimes. The overdamped mode was represented by experiments on optically trapped particles in the tractor beam performed in an aqueous medium. In such a tractor beam created by a retro–reflection of a wide Gaussian beam, an illuminated particle can be pushed or pulled against the total wave vector, depending on the scattering force acting on the particle. However, motion direction can be changed if more particles are optically trapped in the tractor beam, as we have demonstrated in this thesis.

Due to the particle scattering, the illuminated particles were optically bound and formed into stable structures that could move in the tractor beam. Depending on the mutual particle configuration, the interaction force arising from the particle scattering propelled the particles along or against the total wave vector of the tractor beam. We introduced an intuitive picture of the mechanism of motion of an optically bound matter based on the surfing of particle on the slope of the scattered intensity pattern formed by the other particle. We showed that the optical pulling or pushing force acting on the optically bound matter can be by an order enhanced comparing to a single isolated particle placed in the tractor beam with the same parameters. Describing the underlying physical mechanisms provides us with new prospects to control a light–driven self–organisation and transport of illuminated particles.

The second part of the work was devoted to the optical levitation experiments, i.e., a particle optically trapped in the air with reduced pressure. Such a particle behaves like a nanomechanical oscillator that can be sensitive even to ultraweak forces or utilized to examine quantum effects on microscopic objects. To exploit an optically levitated nanoparticle, a precise characterization of oscillator parameters is requested. Nowadays, the most common method is based on the displacement PSD, assuming a harmonic oscillator and evaluating only the steady states. However, this approach is not always applicable. Therefore, we have proposed a novel characterization methodology suitable even for a slightly nonlinear oscillator of a Duffing type.

In our developed DOA and DDE methods, the oscillator parameters were obtained by post–processing averaged recorded trajectories with defined initial positions in the phase space consisting of particle position and momentum. An advantage of the methods is in the parameters extraction directly from the recorded trajectories, while another modification of an experimental system is not needed. Unlike the PSD analysis, the developed procedures provide us with the coefficient of Duffing nonlinearity besides other parameters such as eigenfrequency, damping, and effective temperature.

Supporting the new approach by the numerical simulations based on SDE, we showed the applicability of the DOA method even at lower ambient pressures. Under these conditions, the nonlinearity starts to play a significant role, and the PSD fitting fails due to the deformation of the oscillation peak. Our proposed method can be utilized in experiments performed at high vacuum, such as measurement of very tiny forces or cooling of particle centre–of–mass motion to get a particle into its quantum ground state. Evaluating the particle trajectories, this approach allows us to study even transient dynamics of the nonlinear system, which can be crucial for upcoming studies of quantum effects.

LIST OF ACRONYMS

CCD	charge–coupled device
CMOS	complementary metal–oxide–semiconductor
DDE	deterministic Duffing equation
DOA	Duffing oscillator approximation
FPGA	field–programmable gate array
PSD	power spectral density
QPD	quadrant photodetector
SDE	stochastic Duffing equation

BIBLIOGRAPHY

[1] T. H. Maiman. Stimulated optical radiation in ruby. *Nature*, 187(4736):493–494, 1960.

[2] P. Rodríguez-Sevilla, L. Labrador-Páez, D. Jaque, and P. Haro-González. Optical trapping for biosensing: Materials and applications. *J. Mater. Chem. B*, 5:9085–9101, 2017.

[3] C. Xie, D. Chen, and Y.-Q. Li. Raman sorting and identification of single living micro-organisms with optical tweezers. *Opt. Lett.*, 30(14):1800–1802, 2005.

[4] S. Bize, P. Laurent, M. Abgrall, H. Marion, I. Maksimovic, L. Cacciapuoti, J. Grünert, C. Vian, F. Pereira dos Santos, and P. Rosenbusch. Cold atom clocks and applications. *J. Phys. B*, 38(9):S449, 2005.

[5] A. Öttl, S. Ritter, M. Köhl, and T. Esslinger. Correlations and Counting Statistics of an Atom Laser. *Phys. Rev. Lett.*, 95:090404, 2005.

[6] D. DeMille. Quantum Computation with Trapped Polar Molecules. *Phys. Rev. Lett.*, 88:067901, 2002.

[7] O. Brzobohatý, V. Karásek, M. Šiler, L. Chvátal, T. Čizmár, and P. Zemánek. Experimental demonstration of optical transport, sorting and self-arrangement using a 'tractor beam'. *Nat. Photonics*, 7(2):123–127, 2013.

[8] J. Damková, L. Chvátal, J. Ježek, J. Oulehla, O. Brzobohatý, and P. Zemánek. Enhancement of the 'tractor-beam' pulling force on an optically bound structure. *Light Sci. Appl.*, 7:17135, 2018.

[9] L. Dixon, F. C. Cheong, and D. G. Grier. Holographic deconvolution microscopy for high–resolution particle tracking. *Opt. Express*, 19(17):16410–16417, 2011.

[10] S. H. Lee and D. G. Grier. Holographic microscopy of holographically trapped three–dimensional structures. *Opt. Express*, 15(4):1505–1512, 2007.

[11] D. Mackowski. *The Extension of Mie Theory to Multiple Spheres.* Springer, New York, 2012.

[12] J. Gieseler, B. Deutsch, R. Quidant, and L. Novotny. Subkelvin Parametric Feedback Cooling of a Laser-Trapped Nanoparticle. *Phys. Rev. Lett.*, 109:103603–5, 2012.

[13] L. P. Neukirch, J. Gieseler, R. Quidant, L. Novotny, and A. N. Vamivakas. Observation of nitrogen vacancy photoluminescence from an optically levitated nanodiamond. *Opt. Lett.*, 38(16):2976–2979, 2013.

[14] J. Millen, T. Deesuwan, P. Barker, and J. Anders. Nanoscale temperature measurements using non-equilibrium Brownian dynamics of a levitated nanosphere. *Nat. Nanotechnol.*, 9:425–429, 2014.

[15] L. Jauffred, S. M. R. Taheri, R. Schmitt, H. Linke, and L. B. Oddershede. Optical trapping of gold nanoparticles in air. *Nano Lett.*, 15:4713–4719, 2015.

[16] T. M. Hoang, J. Ahn, J. Bang, and T. Li. Electron spin control of optically levitated nanodiamonds in vacuum. *Nat. Commun.*, 7:12250, 2016.

[17] U. Delić, M. Reisenbauer, K. Dare, D. Grass, V. Vuletić, N. Kiesel, and M. Aspelmeyer. Cooling of a levitated nanoparticle to the motional quantum ground state. *Science*, 367(6480):892–895, 2020.

[18] J. Flajšmanová, M. Šiler, P. Jedlička, F. Hrubý, O. Brzobohatý, R. Filip, and P. Zemánek. Using the transient trajectories of an optically levitated nanoparticle to characterize a stochastic Duffing oscillator. *Sci. Rep.*, 10:14436, 2020.

[19] G. Ranjit, M. Cunningham, K. Casey, and A. A. Geraci. Zeptonewton force sensing with nanospheres in an optical lattice. *Phys. Rev. A*, 93(5):053801–5, 2016.

[20] D. Hempston, J. Vovrosh, M. Toroš, G. Winstone, M. Rashida, and H. Ulbricht. Force sensing with an optically levitated charged nanoparticle. *Appl. Phys. Lett.*, 111:133111, 2017.

[21] J. Gieseler, L. Novotny, and R. Quidant. Thermal nonlinearities in a nanomechanical oscillator. *Nat. Phys.*, 9:806–810, 2013.

[22] E. Hebestreit, M. Frimmer, R. Reimann, and L. Novotny. Sensing Static Forces with Free-Falling Nanoparticles. *Phys. Rev. Lett.*, 121(6):063602, 2018.

[23] J. Millen and J. Gieseler. *Thermodynamics in the Quantum Regime: Fundamental Aspects and New Directions*. Springer Nature Switzerland AG, Cham, Switzerland, 2018.

[24] J. Gieseler and J. Millen. Levitated Nanoparticles for Microscopic Thermodynamics - A Review. *Entropy*, 20(5):326, 2018.

[25] O. Romero-Isart, A. C. Pflanzer, F. Blaser, R. Kaltenbaek, N. Kiesel, M. Aspelmeyer, and J. I. Cirac. Large Quantum Superpositions and Interference of Massive Nanometer-Sized Objects. *Phys. Rev. Lett.*, 107:020405, 2011.

[26] O. Romero-Isart. Quantum superposition of massive objects and collapse models. *Phys. Rev. A*, 84:052121, 2011.

[27] T. Li, S. Kheifets, D. Medellin, and M. G. Raizen. Measurement of the instantaneous velocity of a Brownian particle. *Science*, 328(5986):1673–1675, 2010.

[28] E. Hebestreit, R. Reimann, M. Frimmer, and L. Novotny. Measuring the internal temperature of a levitated nanoparticle in high vacuum. *Phys. Rev. A*, 97:043803, 2018.

[29] A. Ashkin. Acceleration and Trapping of Particles by Radiation Pressure. *Phys. Rev. Lett.*, 24(4):156–159, 1970.

[30] A. Ashkin. Trapping of Atoms by Resonance Radiation Pressure. *Phys. Rev. Lett.*, 40(12):729–732, 1978.

[31] A. Ashkin, J. M. Dziedzic, J. E. Bjorkholm, and S. Chu. Observation of a single-beam gradient force optical trap for dielectric particles. *Opt. Lett.*, 11(5):288–290, 1986.

[32] G. Sinclair, P. Jordan, J. Courtial, M. Padgett, J. Cooper, and Z. J. Laczik. Assembly of 3-dimensional structures using programmable holographic optical tweezers. *Opt. Express*, 12(22):5475–5480, 2004.

[33] S. E. Skelton Spesyvtseva and K. Dholakia. Trapping in a material world. *ACS Photonics*, 3(5):719–736, 2016.

[34] A. Ashkin. Forces of a single-beam gradient laser trap on a dielectric sphere in the ray optics regime. *Biophys. J.*, 61(2):569–582, 1992.

[35] P. Polimeno, A. Magazzù, M. A. Iatì, F. Patti, R. Saija, C. D. Esposti Boschi, M. G. Donato, P. G. Gucciardi, P. H. Jones, G. Volpe, , and O. M. Maragò. Optical tweezers and their applications. *J. Quant. Spectrosc. Radiat. Transf.*, 218:131–150, 2018.

[36] M. Dienerowitz, M. Mazilu, and K. Dholakia. Optical manipulation of nanoparticles: a review. *J. Nanophotonics*, 2:021875, 2008.

[37] J. A. Lock. Calculation of the radiation trapping force for laser tweezers by use of generalized Lorenz–Mie theory. I. Localized model description of an on-axis tightly focused laser beam with spherical aberration. *Appl. Opt.*, 43(12):2532–2544, 2004.

[38] J. A. Lock. Calculation of the radiation trapping force for laser tweezers by use of generalized Lorenz–Mie theory. II. On-axis trapping force. *Appl. Opt.*, 43(12):2545–2554, 2004.

[39] W. Hergert and T. Wriedt. *The Mie theory: Basics and applications*. Springer, New York, 2012.

[40] B. T. Draine and J. Goodman. Beyond Clausius–Mossotti: Wave propagation on a polarizable point lattice and the discrete dipole approximation. *Astrophys. J.*, 405:685–697, 1993.

[41] S. E. Skelton, M. Sergides, R. Saija, M. A. Iatì, O. M. Maragó, and P. H. Jones. Trapping volume control in optical tweezers using cylindrical vector beams. *Opt. Lett.*, 38(1):28–30, 2013.

[42] M. G. Donato, S. Vasi, R. Sayed, P. H. Jones, F. Bonaccorso, A. C. Ferrari, P. G. Gucciardi, and O. M. Maragò. Optical trapping of nanotubes with cylindrical vector beams. *Opt. Lett.*, 13(16):3381–3383, 2012.

[43] P. Zemánek, G. Volpe, A. Jonáš, and O. Brzobohatý. Perspective on light-induced transport of particles: from optical forces to phoretic motion. *Adv. Opt. Photonics*, 11(3):577–678, 2019.

[44] Ø. Farsund and B. U. Felderhof. Force, torque, and absorbed energy for a body of arbitrary shape and constitution in an electromagnetic radiation field. *Physica A*, 227(1):108–130, 1996.

[45] C. F. Bohren and D. R. Huffman. *Absorption and Scattering of Light by Small Particles*. Wiley-VCH, New York, 1998.

[46] J. J. Sáenz. Laser tractor beams. *Nat. Photonics*, 5:514–515, 2011.

[47] J. Chen, J. Ng, Z. Lin, and C. T. Chan. Optical pulling force. *Nat. Photonics*, 5:531–534, 2011.

[48] C. A. Ebongue, D. Holzmann, S. Ostermann, and H. Ritsch. Generating a stationary infinite range tractor force via a multimode optical fibre. *J. Opt.*, 19(6):065401, 2017.

[49] O. Brzobohatý, T. Čižmár, V. Karásek, M. Šiler, K. Dholakia, and P. Zemánek. Experimental and theoretical determination of optical binding forces. *Opt. Express*, 18(24):25389–25402, 2010.

[50] A. Mizrahi and Y. Fainman. Negative radiation pressure on gain medium structures. *Opt. Lett.*, 35:3405–3407, 2010.

[51] D. E. Fernandes and M. G. Silveirinha. Optical tractor beam with chiral light. *Phys. Rev. A*, 91:061801, 2015.

[52] S. Sukhov and A. Dogariu. On the concept of "tractor beams". *Opt. Lett.*, 35(22):3847–3849, 2010.

[53] A. Novitski, C. W. Qui, and H. F. Wang. Single Gradientless Light Beam Drags Particles as Tractor Beams. *Phys. Rev. Lett.*, 107:203601, 2011.

[54] D. B. Ruffner and D. G. Grier. Optical Forces and Torques in Nonuniform Beams of Light. *Phys. Rev. Lett.*, 108(17):173602, 2012.

[55] S. Sukhov and A. Dogariu. Negative Nonconservative Forces: Optical "Tractor Beams" for Arbitrary Objects. *Phys. Rev. Lett.*, 108:203602, 2011.

[56] V. Kajorndejnukul, W. G. Ding, S. Sukhov, C. W. Qiu, and A. Dogariu. Linear momentum increase and negative optical forces at dielectric interface. *Nat. Photon.*, 7:787–790, 2013.

[57] V. Shvedov, A. R. Davoyan, C. Hnatovsky, N. Engheta, and W. Krolikowski. A long-range polarization-controlled optical tractor beam. *Nat. Photon.*, 8(11):846–850, 2014.

[58] S.-H. Lee, Y. Roichman, and D. G. Grier. Optical solenoid beams. *Opt. Express*, 18(7):6988–6993, 2010.

[59] A. Salandrino and D. N. Christodoulides. Reverse optical forces in negative index dielectric waveguide arrays. *Opt. Lett.*, 36(16):3103–3105, 2011.

[60] T. Thirunamachandran. Intermolecular interactions in the presence of an intense radiation field. *Mol. Phys.*, 40:393–399, 1980.

[61] M. M. Burns, J.-M. Fournier, and J. A. Golovchenko. Optical Binding. *Phys. Rev. Lett.*, 63:1233–1236, 1989.

[62] M. M. Burns, J.-M. Fournier, and J. A. Golovchenko. Optical matter: Crystallization and binding in intense optical fields. *Science*, 249:749, 1990.

[63] J. Ng, Z. F. Lin, C. T. Chan, and P. Sheng. Photonic clusters formed by dielectric microspheres: Numerical simulations. *Phys. Rev. B*, 72:085130, 2005.

[64] L. Chvátal, O. Brzobohatý, and P. Zemánek. Binding of a pair of Au nanoparticles in a wide Gaussian standing wave. *Opt. Rev.* , 22(1):157–161, 2015.

[65] M. Šiler, T. Čižmár, M. Šerý, and P. Zemánek. Optical forces generated by evanescent standing waves and their usage for sub-micron particle delivery. *Appl. Phys. B*, 84:157–165, 2006.

[66] V. Karásek, K. Dholakia, and P. Zemánek. Analysis of optical binding in one dimension. *Appl. Phys. B*, 84:149–156, 2006.

[67] V. Karásek, O. Brzobohatý, and P. Zemánek. Longitudinal optical binding of several spherical particles studied by the coupled dipole method. *J. Opt. A: Pure Appl. Opt.*, 11:034009, 2009.

[68] V. Karásek, T. Čižmár, O. Brzobohatý, P. Zemánek, V. Garcés-Chávez, and K. Dholakia. Long-Range One-Dimensional Longitudinal Optical Binding. *Phys. Rev. Lett.*, 101(14):143601, 2008.

[69] X. Han and P. H. Jones. Evanescent wave optical binding forces on spherical microparticles. *Opt. Lett.*, 40(17):4042–4045, 2015.

[70] O. Brzobohatý, L. Chvátal, and P. Zemánek. Optomechanical properties of optically self-arranged colloidal waveguides. *Opt. Lett.*, 44(3):707–710, 2019.

[71] O. Brzobohatý, L. Chvátal, A. Jonáš, M. Šiler, J. Kaňka, J. Ježek, and P. Zemánek. Tunable soft-matter optofluidic waveguides assembled by light. *ACS Photonics*, 6(2):403–410, 2019.

[72] O. Brzobohatý, V. Karásek, T. Čižmár, and P. Zemánek. Dynamic size tuning of multidimensional optically bound matter. *Appl. Phys. Lett.*, 99(10):101105, 2011.

[73] S. H. Simpson, L. Chvátal, and P. Zemánek. Synchronization of colloidal rotors through angular optical binding. *Phys. Rev. A*, 93(2):023842, 2016.

[74] O. Brzobohatý, A. V. Arzola, M. Šiler, L. Chvátal, P. Jákl, S. H. Simpson, and P. Zemánek. Complex rotational dynamics of multiple spheroidal particles in a circularly polarized, dual beam trap. *Opt. Express*, 23(6):7273–7287, 2015.

[75] C. Zaza, I. Violo, J. Gargiulo, G. Chiarelli, L. Schumacher, J. Jakobi, J. Olomos-Trigo, E. Cortes, M. Konig, S. Barcikowski, S. Schlucker, J. Sáenz,

S. Maier, and F. Stefani. Size–selective optical printing of silicon nanoparticles through their dipolar magnetic resonance. *ACS Photonics*, 6(4):815–822, 2019.

[76] M. Nieto-Vesperinas, J. J. Sáenz, R. Gomez-Medina, and L. Chantada. Optical forces on small magnetodielectric particles. *Opt. Express*, 18(11):11428–11443, 2010.

[77] P. C. Chaumet and A. Rahmani. Electromagnetic force and torque on magnetic and negative-index scatterers. *Opt. Express*, 17:2224–2234, 2009.

[78] R. Gómez-Medina, B. García-Cámara, I. Suárez-Lacalle, L. S. Froufe-Pérez, F. González, F. Moreno, M. Nieto-Vesperinas, and J. J. Sáenz. Electric and magnetic optical response of dielectric nanospheres: Optical forces and scattering anisotropy. *Photonics Nanostructures: Fundam. Appl.*, 10:345–352, 2012.

[79] T. Zhu, Y. Cao, L. Wang, Z. Nie, T. Cao, F. Sun, Z. Jiang, M. Nieto-Vesperinas, Y. Liu, Ch.-W. Qiu, and W. Ding. Self-Induced Backaction Optical Pulling Force. *Phys. Rev. Lett.*, 120(12):123901, 2018.

[80] M. I. Petrov, S. V. Sukhov, A. A. Bogdanov, A. S. Shalin, and A. Dogariu. Surface plasmon polariton assisted optical pulling force. *Laser Photon. Rev.*, 10(1):116–122, 2016.

[81] E. Lee, D. Huang, and T. Luo. Ballistic supercavitating nano swimmer driven by single Gaussian beam optical pushing and pulling forces. *arXiv preprint arXiv:1908.05987*, 2019.

[82] T. Čižmár, V. Garcés-Chávez, K. Dholakia, and P. Zemánek. Optical conveyor belt for delivery of submicron objects. *Appl. Phys. Lett.*, 86:174101, 2005.

[83] T. Čižmár, V. Kollárová, Z. Bouchal, and P. Zemánek. Sub-micron particle organization by self-imaging of non-diffracting beams. *New. J. Phys.*, 8:43:1–23, 2006.

[84] D. B. Ruffner and D. G. Grier. Optical Conveyors: A Class of Active Tractor Beams. *Phys. Rev. Lett.*, 109:163903, 2012.

[85] V. Demergis and E.-L. Florin. Ultrastrong optical binding of metallic nanoparticles. *Nano Lett.*, 12(11):5756–5760, 2012.

[86] M. P. MacDonald, L. Paterson, K. Volke-Sepulveda, J. Arlt, W. Sibbett, and K. Dholakia. Creation and manipulation of three-dimensional optically trapped structures. *Science*, 296:1101–1103, 2002.

[87] V. Karásek and P. Zemánek. Analytical description of longitudinal optical binding of two spherical nanoparticles. *J. Opt. A: Pure Appl. Opt.*, 9:S215–S220, 2007.

[88] K. Dholakia and P. Zemánek. Gripped by light: Optical binding. *Rev. Mod. Phys.*, 82:1767–1791, 2010.

[89] L. Novotny and B. Hecht. *Principles of Nano-Optics*. Cambridge University Press, Cambridge, 2006.

[90] F. Depasse and J. M. Vigoureux. Optical binding force between two Rayleigh particles. *J. Phys. D: Appl. Phys.*, 27:914–919, 1994.

[91] N. K. Metzger, E. M. Wright, and K. Dholakia. Theory and simulation of the bistable behaviour of optically bound particles in the Mie size regime. *New J. Phys.*, 8:139, 2006.

[92] P. C. Chaumet and M. Nieto-Vesperinas. Coupled dipole method determination of the electromagnetic force on a particle over a flat dielectric substrate. *Phys. Rev. B*, 61:14119–14127, 2000.

[93] D. A. White. Vector finite element modeling of optical tweezers. *Comp. Phys. Commun.*, 128:558–564, 2000.

[94] D. C. Benito, S. H. Simpson, and S. Hanna. FDTD simulations of forces on particles during holographic assembly. *Opt. Express*, 16:2942–2957, 2008.

[95] A. Mazolli, P. A. Maia Neto, and H. M. Nussenzveig. Theory of trapping forces in optical tweezers. In *Proc. R. Soc. Lond. A*, volume 459, page 3021, 2003.

[96] J. Damková, L. Chvátal, O. Brzobohatý, and P. Zemánek. Optical Binding of Particle Pairs in Retro-Reflected Beam Geometry. *Proc. SPIE*, page 10142, 2016.

[97] F. C. Cheong, J. Krishnatreya, and D. G. Grier. Strategies for three-dimensional particle tracking with holographic video microscopy. *Opt. Express*, 18(13):13563–13573, 2010.

[98] B. J. Krishnatreya, A. Colen-Landy, P. Hasebe, B. A. Bell, J. R. Jones, A. Sunda-Meya, and D. G. Grier. Measuring Boltzmann's constant through holographic video microscopy of a single colloidal sphere. *Am. J. Phys.*, 82(1):23–31, 2014.

[99] S. H. Lee, Y. Roichman, G. R. Yi, S. H. Kim, S. M. Yang, A. van Blaaderen, P. van Oostrum, and D. G. Grier. Characterizing and tracking single colloidal particles with video holographic microscopy. *Opt. Express*, 15:18275–18282, 2007.

[100] P. Reuland, B. U. Felderhof, and R. B. Jones. Hydrodynamic interaction of two spherically symmetric polymers. *Physica*, 93A(3-4):465–475, 1978.

[101] A. Ashkin and J. M. Dziedzic. Optical levitation by radiation pressure. *Appl. Phys. Lett.*, 19:283–285, 1971.

[102] A. Ashkin and J. M. Dziedzic. Optical levitation in high vacuum. *Appl. Phys. Lett.*, 28:333–335, 1976.

[103] N. Kiesel, F. Blaser, U. Delić, D. Grass, R. Kaltenbaek, and M. Aspelmeyer. Cavity cooling of an optically levitated submicron particle. *Proc. Natl. Acad. Sci. USA*, 110(35):14180–14185, 2013.

[104] J. Millen, P. Z. G. Fonseca, T. Mavrogordatos, T. S. Monteiro, and P. F. Barker. Cavity Cooling a Single Charged Levitated Nanosphere. *Phys. Rev. Lett.*, 114(12):123602–5, 2015.

[105] D. E. Chang, C. A. Regal, S. B. Papp, D. J. Wilson, J. Ye, O. Painter, H. J. Kimble, and P. Zoller. Cavity opto-mechanics using an optically levitated nanosphere. *Proc. Natl. Acad. Sci. USA*, 107:1005–1010, 2010.

[106] O. Romero-Isart, M. J. Juan, R. Quidant, and J. I. Cirac. Toward quantum superposition of living organisms. *New J. Phys.*, 12:033015, 2010.

[107] P. F. Barker. Doppler Cooling a Microsphere. *Phys. Rev. Lett.*, 105:073002, 2010.

[108] Z.-Q. Yin, A. A. Geraci, and T. Li. Optomechanics of levitated dielectric particles. *Int. J. Mod. Phys. B*, 27(26):1330018, 2013.

[109] N. Vamivakas, M. Bhattacharya, and P. Barker. Levitated optomechanics. *Opt. Photon. News*, 27:42–49, 2016.

[110] J. Millen, T. S. Monteiro, R. Pettit, and A. N. Vamivakas. Optomechanics with levitated particles. *Rep. Prog. Phys.*, 83:026401, 2020.

[111] Y. Arita, M. Mazilu, and K. Dholakia. Laser-induced rotation and cooling of a trapped microgyroscope in vacuum. *Nat. Commun.*, 4:2374, 2013.

[112] Yoshihiko Arita, Andrew W. McKinley, Michael Mazilu, Halina Rubinsztein-Dunlop, and Kishan Dholakia. Picoliter rheology of gaseous media using a rotating optically trapped birefringent microparticle. *Anal. Chem.*, 83(23):8855–8858, 2011.

[113] G. Ranjit, D. P. Atherton, J. H. Stutz, M. Cunningham, and A. A. Geraci. Attonewton force detection using microspheres in a dual-beam optical trap in high vacuum. *Phys. Rev. A*, 91(5):051805, 2015.

[114] L.-O. Heim, J. Blum, M. Preuss, and H.-J. Butt. Adhesion and Friction Forces between Spherical Micrometer–Sized Particles. *Phys. Rev. Lett.*, 83(16):3328–3331, 1999.

[115] J. Gieseler. *Dynamics of optically levitated nanoparticles in high vacuum*. PhD thesis, ICFO Spain, 2014.

[116] P. Mestres, J. Berthelot, M. Spasenovic, J. Gieseler, L. Novotny, and R. Quidant. Cooling and manipulation of a levitated nanoparticle with an optical fiber trap. *Appl. Phys. Lett.*, 107(15), 2015.

[117] A. Torki. Mechanical transfer of optically trapped nanoparticle. Master's thesis, KTH Royal Institute of Technology, 2016.

[118] S. Kuhn, P. Asenbaum, A. Kosloff, M. Sclafani, B. A. Stickler, S. Nimmrichter, K. Hornberger, O. Cheshnovsky, F. Patolsky, and M. Arndt. Cavity-assisted manipulation of freely rotating silicon nanorods in high vacuum. *Nano Lett.*, 15:5604–5608, 2015.

[119] Z. Fu, X. She, N. Li, and H. Hu. Launch and capture of a single particle in a pulse-laser-assisted dual-beam fiber-optic trap. *Opt. Commun.*, 417:103–109, 2018.

[120] V. Svak, O. Brzobohatý, M. Šiler, P. Jákl, J. Kaňka, P. Zemánek, and S. H. Simpson. Transverse spin forces and non-equilibrium particle dynamics in a circularly polarized vacuum optical trap. *Nat. Commun.*, 9:5453, 2018.

[121] A. T. M. Anishur Rahman, A. C. Frangeskou, P. F. Barker, and G. W. Morley. An analytical model for the detection of levitated nanoparticles in optomechanics. *Rev. Sci. Instrum.*, 89(2):023109, 2018.

[122] A. Rohrbach and E. H. K. Stelzer. Three-dimensional position detection of optically trapped dielectric particles. *J. Appl. Phys.*, 91:5474–5488, 2002.

[123] R. M. Simmons. Quantitative measurement of force and displacement using an optical trap. *Biophys. J.*, 70:1813–1822, 1996.

[124] V. Jain, J. Gieseler, C. Moritz, C. Dellago, R. Quidant, and L. Novotny. Direct Measurement of Photon Recoil from a Levitated Nanoparticle. *Phys. Rev. Lett.*, 116(24):243601–5, 2016.

[125] F. Tebbenjohanns, M. Frimmer, A. Militaru, V. Jain, and L. Novotny. Cold Damping of an Optically Levitated Nanoparticle to Microkelvin Temperatures. *Phys. Rev. Lett.*, 122:223601, 2019.

[126] S. Kuhn, A. Kosloff, B. A. Stickler, F. Patolsky, K. Hornberger, M. Arndt, and J. Millen. Full rotational control of levitated silicon nanorods. *Optica*, 4(3):356–360, 2017.

[127] G. Wachter, S. Kuhn, S. Minniberger, C. Salter, P. Asenbaum, J. Millen, M. Schneider, J. Schalko, U. Schmid, A. Felgner, D. Hüser, M. Arndt, and M. Trupke. Silicon microcavity arrays with open access and a finesse of half a million. *Light Sci. Appl.*, 8:37, 2019.

[128] S. Kuhn, G. Wachter, F. F. Wieser, J. Millen, M. Schneider, J. Schalko, U. Schmid, M. Trupke, and M. Arndt. Nanoparticle detection in an open-access silicon microcavity. *Appl. Phys. Lett.*, 111:253107, 2017.

[129] L. Magrini, R. A. Norte, R. Riedinger, I. Marinkovic, D. Grass, U. Delić, S. Groeblacher, S. Hong, and M. Aspelmeyer. Near-field coupling of a levitated nanoparticle to a photonic crystal cavity. *Optica*, 5(12):1597–1602, 2018.

[130] P. Asenbaum, S. Kuhn, S. Nimmrichter, U. Sezer, and M. Arndt. Cavity cooling of free silicon nanoparticles in high vacuum. *Nat. Commun.*, 4:2743, 2013.

[131] F. Tebbenjohanns, M. Frimmer, and L. Novotny. Optimal position detection of a dipolar scatterer in a focused field. *Phys. Rev. A*, 100:043821, 2019.

[132] M. Frimmer, J. Gieseler, T. Ihn, and L. Novotny. Levitated nanoparticle as a classical two-level atom. *J. Opt. Soc. Am. B*, 34:C52–C57, 2017.

[133] M. Poot and H. S. J. van der Zant. Mechanical systems in the quantum regime. *Phys. Rep.*, 511(5):273–335, 2012.

[134] Y. Tsaturyan, A. Barg, E. S. Polzik, and A. Schliesser. Ultracoherent nanomechanical resonators via soft clamping and dissipation dilution. *Nat. Nanotechnol.*, 12:776–783, 2017.

[135] L. Rondin, J. Gieseler, F. Ricci, R. Quidant, C. Dellago, and L. Novotny. Direct measurement of Kramers turnover with a levitated nanoparticle. *Nat. Nanotechnol.*, 12:1130, 2017.

[136] T. Li and M. G. Raizen. Brownian motion at short time scales. *Ann. Phys.*, 525(4):281–295, 2013.

[137] J. Gieseler, R. Quidant, C. Dellago, and L. Novotny. Dynamic relaxation of a levitated nanoparticle from a non-equilibrium steady state. *Nat. Nanotechnol.*, 9(5):358–364, 2014.

[138] T. M. Hoang, R. Pan, J. Ahn, J. Bang, H. T. Quan, and T. Li. Experimental Test of the Differential Fluctuation Theorem and a Generalized Jarzynski Equality for Arbitrary Initial States. *Phys. Rev. Lett.*, 120(8):080602, 2018.

[139] M. Mazilu, Y. Arita, T. Vettenburg, J. M. Aunon, E. M. Wright, and K. Dholakia. Orbital-angular-momentum transfer to optically levitated microparticles in vacuum. *Phys. Rev. A*, 94(5):053821, 2016.

[140] A. Manjavacas, F. J. Rodríguez-Fortuño, F. J. García de Abajo, and A. V. Zayats. Lateral Casimir Force on a Rotating Particle near Planar Surface. *Phys. Rev. Lett.*, 118:133605, 2017.

[141] R. Reimann, M. Doderer, E. Hebestreit, R. Diehl, M. Frimmer, D. Windey, F. Tebbenjohanns, and L. Novotny. GHz Rotation of an Optically Trapped Nanoparticle in Vacuum. *Phys. Rev. Lett.*, 121(3):033602, 2018.

[142] L. Paterson, M. P. MacDonald, J. Arlt, W. Sibbett, P. E. Bryant, and K. Dholakia. Controlled rotation of optically trapped microscopic particles. *Science*, 292:912–914, 2001.

[143] A. I. Bishop, T. A. Nieminen, N. R. Heckenberg, and H. Rubinsztein-Dunlop. Optical Microrheology using Rotating Laser-Trapped Particles. *Phys. Rev. Lett.*, 92(19):198104, 2004.

[144] B. A. Stickler, S. Nimmrichter, L. Martinetz, S. Kuhn, M. Arndt, and K. Hornberger. Rotranslational cavity cooling of dielectric rods and disks. *Phys. Rev. A*, 94:033818, 2016.

[145] Y. Arita, M. Mazilu, T. Vettenburg, E. M. Wright, and K. Dholakia. Rotation of two trapped microparticles in vacuum: observation of optically mediated parametric resonances. *Opt. Lett.*, 40(20):4751–4754, 2015.

[146] S. Kuhn, B. A. Stickler, A. Kosloff, F. Patolsky, K. Hornberger, M. Arndt, and J. Millen. Optically driven ultra-stable nanomechanical rotor. *Nat. Commun.*, 8:1670–5, 2017.

[147] F. Monteiro, S. Ghosh, E. C. van Assendelft, and D. C. Moore. Optomechanics with levitated particles. *Rep. Prog. Phys.*, 97:051802(R), 2018.

[148] A. Roulet, S. Nimmrichter, J. M. Arrazola, S. Seah, and V. Scarani. Autonomous rotor heat engine. *Phys. Rev. E*, 95:062131, 2017.

[149] V. Blicke and Bechinger C. Realization of a micrometre-sized stochastic heat engine. *Nat. Phys.*, 8:143–146, 2012.

[150] I. A. Martínez, E. Roldán, L. Dinis, D. Petrov, J. M. R. Parrondo, and R. A. Rica. Brownian Carnot engine. *Nat. Phys.*, 12:67–70, 2016.

[151] A. Ashkin and J. M. Dziedzic. Feedback stabilization of optically levitated particles. *Appl. Phys. Lett.*, 30:202–4, 1977.

[152] G. P. Conangla, F. Ricci, M. T. Cuairan, A. W. Schell, N. Meyer, and R. Quidant. Optimal Feedback Cooling of a Charged Levitated Nanoparticle with Adaptive Control. *Phys. Rev. Lett.*, 122:223602, 2019.

[153] F. Tebbenjohanns, M. Frimmer, V. Jain, D. Windey, and L. Novotny. Motional Sideband Asymmetry of a Nanoparticle Optically Levitated in Free Space. *Phys. Rev. Lett.*, 124:013603, 2020.

[154] P. F. Barker and M. N. Shneider. Cavity cooling of an optically trapped nanoparticle. *Phys. Rev. A*, 81:023826, 2010.

[155] U. Delić, M. Reisenbauer, D. Grass, N. Kiesel, V. Vuletić, and M. Aspelmeyer. Cavity cooling of a levitated nanosphere by coherent scattering. *Phys. Rev. Lett.*, 122(12):123602–6, 2019.

[156] D. Windey, C. Gonzalez-Ballestero, P. Maurer, L. Novotny, O. Romero-Isart, and R. Reimann. Cavity-Based 3D Cooling of a Levitated Nanoparticle via Coherent Scattering. *Phys. Rev. Lett.*, 122:123601–5, 2019.

[157] T. Li, S. Kheifets, and M. G Raizen. Millikelvin cooling of an optically trapped microsphere in vacuum. *Nat. Phys.*, 7:527–530, 2011.

[158] A. Setter, M Toroš, J. F. Ralph, and H. Ulbricht. Real–time Kalman filter: Cooling of an optically levitated nanoparticle. *Phys. Rev. A*, 97:033822, 2018.

[159] N. P. Bullier, A. Pontin, and P. F. Barker. Characterisation of a charged particle levitated nano-oscillator. *J. Phys. D: Appl. Phys.*, 53:175302, 2020.

[160] O. Romero-Isart, L. Clemente, C. Navau, A. Sanchez, and J. I. Cirac. Quantum Magnetomechanics with Levitating Superconducting Microspheres. *Phys. Rev. Lett.*, 109:147205, 2012.

[161] C. Timberlake, G. Gasbarri, A. Vinante, A. Setter, and H. Ulbricht. Acceleration sensing with magnetically levitated oscillators. *Appl. Phys. Lett.*, 115:224101, 2019.

[162] G. Winstone, R. Bennett, M. Rademacher, M. Rashid, S. Buhmann, and H. Ulbricht. Direct measurement of the electrostatic image force of a levitated charged nanoparticle close to a surface. *Phys. Rev. A*, 98:053831, 2018.

[163] R. Diehl, E. Hebestreit, R. Reimann, F. Tebbenjohanns, M. Frimmer, and L. Novotny. Optical levitation and feedback cooling of a nanoparticle at subwavelength distances from a membrane. *Phys. Rev. A*, 98:013851, 2018.

[164] P. H. Jones, O. M. Maragò, and G. Volpe. *Optical tweezers: Principles and applications*. University Press, Cambridge, 2015.

[165] F. Ricci, M. T. Cuairan, G. P. Conangla, A. W. Schell, and R. Quidant. Accurate mass measurement of a levitated nanomechanical resonator for precision force-sensing. *Nano Lett.*, 19(10):6711–6715, 2019.

[166] K. Berg-Sørensen and H. Flyvbjerg. Power spectrum analysis for optical tweezers. *Rev. Sci. Instrum.*, 75(3):594–612, 2004.

[167] S. F. Nørrelykke and H. Flyvbjerg. Harmonic oscillator in heat bath: Exact simulation of time-lapse-recorded data and exact analytical benchmark statistics. *Phys. Rev. E*, 83:041103–10, 2011.

[168] T. Li. *Fundamental tests of physics with optically trapped microspheres*. PhD thesis, The University of Texas at Austin, 2011.

[169] Y. Amarouchene, M. Mangeat, Montes B. V., L. Ondic, T. Guérin, D. S. Dean, and Y. Louyer. Nonequilibrium Dynamics Induced by Scattering Forces for Optically Trapped Nanoparticles in Strongly Inertial Regimes. *Phys. Rev. Lett.*, 122:183901, 2019.

[170] E. Hebestreit, M. Frimmer, R. Reimann, C. Dellago, F. Ricci, and L. Novotny. Calibration and energy measurement of optically levitated nanoparticle sensors. *Rev. Sci. Instrum.*, 89(3):033111–7, 2018.

[171] W. T. Coffey, Y. T. Kalmykov, and J. T. Waldron. *The Langevin Equation*. World Scientific, Singapore, 2004.

[172] F. Ricci. *Levitodynamics toward force nano–sensors in vacuum*. PhD thesis, ICFO Spain, 2019.

[173] M. Yoneda and K. Aikawa. Thermal broadening of the power spectra of laser-trapped particles in vacuum. *J. Phys. B: At. Mol. Opt. Phys.*, 50:245501–9, 2017.

[174] J. Gieseler, M. Spasenovic, L. Novotny, and R. Quidant. Nonlinear Mode Coupling and Synchronization of a Vacuum-Trapped Nanoparticle. *Phys. Rev. Lett.*, 112:103603–5, 2014.

[175] S. H. Strogatz. *Nonlinear Dynamics and Chaos with Applications to Physics, Biology, Chemistry and Engineering*. Westview Press, Boulder, 2015.

[176] F. Ricci, R. A. Rica, M. Spasenovic, J. Gieseler, L. Rondin, L. Novotny, and R. Quidant. Optically levitated nanoparticle as a model system for stochastic bistable dynamics. *Nat. Commun.*, 8:15141–7, 2017.

[177] A. Chowdhury, S. Barbay, M. G. Clerc, I. Robert-Philip, and R. Braive. Phase Stochastic Resonance in a Forced Nanoelectromechanical Membrane. *Phys. Rev. Lett.*, 119:234101, 2017.

[178] A. Chowdhury, S. Barbay, I. Robert-Philip, and R. Braive. Weak signal enhancement by nonlinear resonance control in a forced nano-electromechanical resonator. *Nat. Comm.*, 11:2400, 2020.

[179] J. Güttinger, A. Noury, P. Weber, A. M. Eriksson, C. Lagoin, J. Moser, C. Eichler, A. Wallraff, A. Isacsson, and A. Bachtold. Energy–dependent path of dissipation in nanomechanical resonators. *Nat. Nanotechnol.*, 12:631, 2017.

[180] A. Ganesan, C. Do, and A. Seshia. Phononic Frequency Comb via Intrinsic Three–Wave Mixing. *Phys. Rev. Lett.*, 118:033903, 2017.

[181] C. Chen, D. H. Zanette, D. A. Czaplewski, S. Shaw, and D. López. Direct observation of coherent energy transfer in nonlinear micromechanical oscillators. *Nat. Commun.*, 8:15523, 2017.

[182] L. Huang, S. M. Soskin, I. A. Khovanov, R. Mannella, K. Ninios, and H. B. Chan. Frequency stabilization and noise–induced spectral narrowing in resonators with zero dispersion. *Nat. Commun.*, 10:3930, 2019.

[183] F. Sun, X. Dong, J. Zou, M. I. Dykman, and H. B. Chan. Correlated anomalous phase diffusion of coupled phononic modes in a sideband–driven resonator. *Nat. Commun.*, 7:12694, 2016.

[184] A. Leuch, L. Papariello, O. Zilberberg, C. L. Degen, R. Chitra, and A. Eichler. Parametric Symmetry Breaking in a Nonlinear Resonator. *Phys. Rev. Lett.*, 117:214101, 2016.

[185] R. Meucci, S. Euzzor, E. Pugliese, S. Zambrano, M. R. Gallas, and J. A. C. Gallas. Optimal Phase–Control Strategy for Damped–Driven Duffing Oscillators. *Phys. Rev. Lett.*, 116:044101, 2016.

[186] Y. Wen, N. Ares, F. J. Schupp, T. Pei, G. A. D. Briggs, and E. A. Laird. A coherent nanomechanical oscillator driven by single–electron tunnelling. *Nat. Phys.*, 16:75–82, 2020.

[187] P. Huang, J. Zhou, L. Zhang, D. Hou, S. Lin, W. Deng, C. Meng, C. Duan, C. Ju, X. Zheng, F. Xue, and J. Du. Generating giant and tunable nonlinearity in a macroscopic mechanical resonator from a single chemical bond. *Nat. Commun.*, 7:11517, 2016.

[188] M. Abdi, P. Degenfeld-Schonburg, M. Sameti, C. Navarrete-Benlloch, and M. J. Hartmann. Dissipative Optomechanical Preparation of Macroscopic Quantum Superposition States. *Phys. Rev. Lett.*, 116:233604, 2016.

[189] A. Setter, J. Vovrosh, and H. Ulbricht. Characterization of non-linearities through mechanical squeezing in levitated optomechanics. *Appl. Phys. Lett.*, 115:153106, 2019.

[190] A. A. Rakhubovsky, D. W. Moore, and R. Filip. Nonclassical states of levitated macroscopic objects beyond the ground state. *Quantum Sci. Technol.*, 4:024006–11, 2019.

[191] W. Ge and M. Bhattacharya. Single and two-mode mechanical squeezing of an optically levitated nanodiamond via dressed-state coherence. *New J. Phys.*, 18:103002–16, 2016.

[192] I. Kovacic and M. J. Brennan. *The Duffing Equation Nonlinear Oscillators and their Behaviour.* John Wiley & Sons, Ltd., 2011.

[193] N. Grønbech-Jensen, N. R. Hayre, and O. Farago. Application of the G-JF discrete-time thermostat for fast and accurate molecular simulations. *Comput. Phys. Commun.*, 185(2):524 – 527, 2014.

[194] J. P. Gordon and A. Ashkin. Motion of atoms in a radiation trap. *Phys. Rev. A*, 21:1606–1617, 1980.

LIST OF PUBLICATIONS AND OTHER OUTPUTS

Publications related to the thesis

- **J. Flajšmanová**, M. Šiler, P. Jedlička, F. Hrubý, O. Brzobohatý, R. Filip, and P. Zemánek. Using the transient trajectories of an optically levitated nanoparticle to characterize a stochastic Duffing oscillator. *Sci. Rep.*, 10:14436, 2020. (IF=3.998, cited 0×)
  https://www.nature.com/articles/s41598-020-70908-z
- **J. Damková**, L. Chvátal, J. Ježek, J. Oulehla, O. Brzobohatý, and P. Zemánek. Enhancement of the "tractor-beam" pulling force on an optically bound structure. *Light Sci. Appl.*, 7:17135, 2018. (IF=14.52, cited 15×)
  https://www.nature.com/articles/lsa2017135

Other publications

- V. Svak, **J. Flajšmanová**, L. Chvátal, M. Šiler, A. Jonáš, J. Ježek, S. H. Simpson, P. Zemánek, and O. Brzobohatý. Stochastic dynamics of optically bound matter levitated in vacuum. *Under review.*
- J. Mach, J. Piastek, J. Maniš, V. Čalkovský, T. Šamořil, **J. Damková**, M. Bartošík, S. Voborný, M. Konečný, and T. Šikola. Low temperature selective growth of GaN single crystals on pre-patterned Si substrates. *Appl. Surf. Sci.*, 497:143705, 2019. (IF=6.182, cited 0×)
  https://doi.org/10.1016/j.apsusc.2019.143705

Conference proceedings

- O. Brzobohatý, **J. Damková**, V. Svak, M. Šiler, P. Jákl, S. Simpson, O. Maragò, M.-G. Donato, R. Filip, and P. Zemánek. Vacuum optomechanics of optically levitated objects. *J. Phys.: Conf. Ser.*, 1461:012199, 2020.
  https://iopscience.iop.org/article/10.1088/1742-6596/1461/1/012199
- M. Šiler, **J. Flajšmanová**, V. Svak, P. Jákl. S. H. Simpson, R. Filip, O. Brzobohatý, and P. Zemánek. Vacuum optomechanics of optically levitated objects: determination of nonlinear properties of the optical trap. *Proc. SPIE*, 11297:112970I, 2020.
  https://doi.org/10.1117/12.2546009
- **J. Damková**, M. Šiler, P. Jákl, R. Filip, O. Brzobohatý, and P. Zemánek. Motion of optically levitated nanoparticle in nonlinear regime. *Proc. SPIE*, 10976:109760G, 2018.
  https://doi.org/10.1117/12.2518115
- O. Brzobohatý, S. Simpson, M. Šiler, P. Jákl, **J. Damková**, V. Svak, A. Arzola, K. Volke-Sepúlveda, R. Filip, and P. Zemánek. Experimental stochastic systems based on optical forces. *J. Phys.: Conf. Ser.*, 1092:012173, 2018.
  https://iopscience.iop.org/article/10.1088/1742-6596/1092/1/012173
- O. Brzobohatý, S. Simpson, M. Šiler, P. Jákl, **J. Damková**, V. Svak, A. Arzola, K. Volke-Sepúlveda, R. Filip, and P. Zemánek. Underdamped and overdamped dynamics of objects in nonlinear optical potentials. *Proc. SPIE*, 10712:107120Z, 2018.
  https://doi.org/10.1117/12.2319285
- **J. Damková**, L. Chvátal, J. Ježek, J. Oulehla, O. Brzobohatý, and P. Zemánek. Motion of optically bound particles in tractor beam. *Proc. SPIE*, 10712:107120Y, 2018.
  https://doi.org/10.1117/12.2319363
- **J. Damková**, L. Chvátal, O. Brzobohatý, and P. Zemánek. Optical binding of particle pairs in retro-reflected beam geometry. *Proc. SPIE*, 10142:101420Q, 2016.
  https://doi.org/10.1117/12.2263360
- **J. Damková**, L. Chvátal, O. Brzobohatý, V. Svak, M. Šiler, S. Simpson, and P. Zemánek. Characterizing particle pairs optically bound in "tractor beam". *Proc. SPIE*, 9922:99221Q, 2016.
  https://doi.org/10.1117/12.2237572

Conference contributions

- Light–Matter Interactions Towards the Nanoscale, Erice, Italy. Talk: Quantification of levitated nanoparticle parameters in nonlinear regime. 2019
- QELS, Benasque, Spain. Talk: Characterization of optically levitated nanoparticles in nonlinear regime. 2018
- CPS, Lednice, Czech Republic. Talk: Motion of optically levitated nanoparticle in nonlinear regime. 2018
- ICN+T, Brno, Czech Republic. Talk: Motion of optically bound particles in tractor beam. 2018
- Recent trends, Skalský dvůr, Czech Republic. Talk: Optical binding of polystyrene particles in tractor beam. 2018
- OMC, Yokohama, Japan. Talk: Motion of optically bound particles in "tractor beam". 2018 (*Best student talk*)
- Laser57, Třešť, Czech Republic. Poster: Characterizing particle pairs optically bound in a tractor beam. 2017
- Quantum Nanophotonics, Ascona, Switzerland. Poster: Enhancement of the tractor-beam pulling force on an optically bound structure. 2017
- Spring School on Mesoscopic Physics, Třešť, Czech Republic. Poster: Enhancement of the "tractor-beam" pulling force acting on optically bound particles. 2017
- SCP, Jasná, Slovakia. Talk: Characterizing particle pairs optically bound in "tractor beam". 2016 (*Best student talk*)
- SPIE, San Diego, USA. Talk: Enhancement of the "tractor-beam" pulling force on an optically bound structure. 2016
- Master School on Quantum Nano- and Opto-mechanics, Barcelona, Spain. Poster: Characterizing optically bound nanoparticles in tractor beam. 2016
- Spring School on Mesoscopic Physics, Třešť, Czech Republic. Poster: Characterizing optically bound nanoparticles in tractor beam with holographic microscopy. 2016

MY CONTRIBUTIONS TO THE PRESENTED WORK

Optical binding in tractor beam

- design, building and alignment of the experimental setup
- sample preparation
- software in LabView for the motorized stage with a sample holder
- measurements of all hologram videos
- preprocessing of recorded videos (background subtraction)
- comparisons of trajectories obtained by holographic video microscopy and theoretical predictions (both performed by Mgr. Lukáš Chvátal, Ph.D.)
- discussion on the results together with other group members

Particle levitation

- design, building and alignment of the experimental setup
- sample preparation
- minor revisions in the LabView software for the data acquisition (mainly performed by Ing. Petr Jákl, Ph.D.)
- testing of home–made electronics made by Ing. František Hrubý
- measurements of all recorded trajectories
- discussion on the results together with other group members